University of Innsbruck

Master Thesis

Bloch oscillations in a dipolar quantum gas and setup of a 631nm laser system for spin manipulation of erbium atoms

Simon Gschwendtner

September 6, 2023

Abstract

In recent years, the study of dipolar quantum gases has garnered significant attention because of their unique properties and potential applications in various fields of physics. One intriguing phenomenon observed in these systems is Bloch oscillations, which occur when ultracold atoms are subjected to a periodic potential and an external force.

This master thesis covers the theoretical basis of the atomic species erbium used in the ERBIUM experiment and the understanding of optical lattices and ground states of ultracold atoms within such a system. In addition, it derives a quasi 1D Gross-Pitaevskii-equation, which aims to simulate Bloch oscillations of dipolar atoms within the realm of beyond-mean-field effects. Further, it analyzes the results of these simulations and delves into the features introduced by dipolar interactions and possible explanations for them.

Moreover, it also aims to explain the rebuilding and repair of a 631 nm laser setup, which was not stable enough. From the basic principle of lasers, over the characteristics of a laser diode, to the shaping of an optical beam; This thesis strives to explain acousto- and electro-optical modulators and their use cases within the setup. Furthermore, it illustrates the locking of a laser to a stable reference cavity and shows an unfortunate turn of events during the later stages of the work.

Zusammenfassung

In den letzten Jahren hat die Erforschung dipolarer Quantengase aufgrund ihrer einzigartigen Eigenschaften und ihrer potenziellen Anwendungen in verschiedenen Bereichen der Physik große Aufmerksamkeit erregt. Ein faszinierendes Phänomen, das in solchen Systemen beobachtet wird, sind sogenannte Bloch-Oszillationen, die auftreten, wenn ultrakalte Atome einem periodischen Potenzial und einer äußeren Kraft ausgesetzt sind.

Diese Masterarbeit befasst sich mit den theoretischen Grundlagen der im ERBIUM-Experiment verwendeten Atomspezies Erbium, sowie mit dem Verständnis von optischen Gittern und Grundzuständen ultrakalter Atome in einem solchen System. Darüber hinaus wird eine quasi-1D Gross-Pitaevskii-Gleichung hergeleitet, die darauf abzielt, Bloch-Oszillationen von dipolaren Atomen im Bereich der "beyond-mean-field" Effekte zu simulieren. Darüber hinaus werden die Ergebnisse dieser Simulationen analysiert und die durch dipolare Wechselwirkungen hervorgerufenen Eigenschaften, sowie mögliche Erklärungen für diese, untersucht.

Des Weiteren soll der Wiederaufbau und die Reparatur eines 631 nm-Lasers erklärt werden, welcher zuvor nicht stabil genug während dem Betrieb war. Vom Grundprinzip des Lasers, über die Eigenschaften einer Laserdiode, bis hin zur Formung eines Laserstrahls; Diese Arbeit versucht, grundlegende physikalische Phänomene, wie auch akustische und elektro-optische Modulatoren und ihre Anwendungsfälle innerhalb des Aufbaus zu erklären. Außerdem wird die Kopplung eines Lasers an eine stabile Referenzkavität veranschaulicht und eine unglückliche Wendung in den späteren Phasen der Arbeit aufgezeigt.

Contents

Introduction

The realm of ultracold atomic physics has witnessed remarkable progress in recent decades since the first generation of a Bose-Einstein condensate in 1995 [1, 2], enabling researchers to explore the behavior of quantum gases at temperatures approaching absolute zero. Among the two basic types of quantum gases, Bose-Einstein condensates and degenerate Fermi gases, dipolar quantum gases stand out because of the long-range and anisotropic nature of the interparticle interactions. These interactions arise from the dipole-dipole interactions between atoms or molecules possessing a permanent magnetic or electric dipole moment. As a consequence, dipolar quantum gases exhibit rich and fascinating phenomena, such as, e.g. magnetostriction, self bound droplets and roton mode population [3–5], that are not observed in conventional contact interaction driven quantum gases. Another breakthrough discovery was the supersolid behaviour [6–8], which confirmed that supersolidity does exist in fact and paved the way for an active research field today.

One of the remarkable phenomena exhibited by ultracold atoms subjected to an optical lattice is Bloch oscillations. In the presence of a periodic potential, a quantum particle experiences a force proportional to the gradient of the potential due to gravity and undergoes coherent oscillations in momentum space. Bloch oscillations were initially predicted in the context of solid-state physics [9, 10], describing the behavior of electrons in a crystal lattice subjected to a constant electric field. However, with the advent of ultracold atomic systems, the investigation of Bloch oscillations has extended to the realm of quantum gases [11, 12].

In recent years, experimental and theoretical efforts have been directed towards studying Bloch oscillations in (dipolar) quantum gases [13–16]. These investigations have revealed intriguing properties, including long-lived Bloch oscillations due to an interaction strength tuned to zero [13] and the influence of (weak) magnetic dipole interactions on the interaction-induced dephasing of the Bloch oscillations [16]. As

recent experiments have experimentally shown a beyond-mean-field correction, first proposed in 1957 by Lee, Huang and Yang [17], this correction might also be relevant in this context.

Furthermore, recent experiments have shown that the utilization of narrow linewidth laser may improve the cooling [18, 19], and therefore the loading speed and efficiency into an optical dipole trap. Hence, an optical setup is designed and constructed to prepare for potentially later use as a further cooling step or as a tool to manipulate the spin substates of erbium atoms.

Through a combination of theoretical modeling and numerical simulations, this thesis seeks to contribute to the current understanding of Bloch oscillations in dipolar quantum gases [20] and to pave the way for future advancements in the field of ultracold atomic physics. Furthermore, it aims to open a new possibility to use 631 nm laser light on Erbium atoms for, e.g. further cooling of the atomic cloud or manipulation of spin substates [19].

Chapter 1

Erbium and interactions

Erbium (Er) was first discovered by Carl Mosander in 1843 in oxide form (Er_2O_3) as a component of a rock, which was found in the Ytterby mine in Sweden. First the existence of erbium was doubted, but it was later proven in 1864 by optical spectroscopy, that indeed erbium was present in this rock as erbium oxide [21]. Nowadays, erbium finds quite some application in modern technology, as it is useful to amplify light in the C- and L-band of the telecommunication bands through erbium doped fiber amplifiers [22]. It also finds usage in a variety of medical application because of the erbium doped solid state laser Er:YAG which lases at around 2.9 µm and may actually reduce snoring [23, 24].

1.1 Properties of erbium

First we are going to discuss some basic properties of erbium, like the isotope abundance, electron configuration, coupling schemes and the energy level spectrum. Then we will dive into interactions with magnetic fields and the high magnetic dipole moment. Finally we will have a look at the two-body interactions and parameters in cold atomic gases (of erbium).

1.1.1 Natural occurrence

Erbium belongs to a commonly known category of elements in the periodic table, called the rare earth elements, which are an integral part of the technical world today. More specifically, erbium is part of the lanthanide series at the bottom of

the periodic table. It has an atomic number of $Z = 68$ and a standard arithmetic weight of $A_\mathrm{r}(\mathrm{Er}) = 167.259(3)$ [25]. There are 6 stable isotopes of Er, 5 of which are of bosonic nature, whereas only one follows fermionic statistics. Their masses range from 162 to 170 u, with the unified mass unit $\mathrm{u} = 1.660\,539\,066\,6 \times 10^{-27}\,\mathrm{kg}$. The isotopes are listed in Tab. 1.1 with their corresponding natural abundances on Earth.

Table 1.1: Isotopes of erbium with their corresponding atomic masses, statistics and abundances on Earth [25].

Er isotope	^{162}Er	^{164}Er	^{166}Er	^{167}Er	^{168}Er	^{170}Er
Statistics	boson	boson	boson	fermion	boson	boson
Abundance	0.139 %	1.601 %	33.503 %	22.869 %	26.978 %	14.910 %

Every bosonic isotope shows a little bit different scattering properties and Feshbach resonances than the other, but one important aspect is the relatively high abundance of the fermionic isotope ^{167}Er with a nuclear spin of $I = 7/2$, which allows to study degenerate Fermi gases in the dipolar realm without the need of enriching the erbium sample.

1.1.2 Electron configuration and coupling schemes

Erbium has a total of 68 electrons which fill up the first electron shells the same way as for xenon, followed by the $6s$ shell with two electrons, which leaves a unfilled $4f$ shell with 12 electrons. This results in an electron configuration of the ground state of

$$[\mathrm{Xe}]4f^{12}6s^2\,,$$

where [Xe] denotes the electron configuration of xenon. Because the inner shell is not fully filled and missing two electrons, the resulting structure is called submerged-shell structure. It gives rise to a large orbital momentum quantum number in the ground state of $L = 5$ and a spin of $S = 1$. Written within the notation $^{2S+1}L_J$, this leads to a ground state of $^3\mathrm{H}_6$ with a total angular momentum quantum number of $J = L + S = 6$ in the LS-coupling scheme. This scheme is only applicable to the ground state, whereas for the excited states the jj-coupling has to be taken into account because of the fact that the spin-orbit interaction ($\sim \mathbf{S} \cdot \mathbf{L}$) becomes

comparable to the Coulomb interaction of higher orbital electrons [26].

Within the jj-coupling scheme each electron alone couples first $\mathbf{l}$ and $\mathbf{s}$ together, forming $\mathbf{j}_1 = \mathbf{l}_1 + \mathbf{s}_1$. In the special case of the J_1J_2-coupling, all electrons independently couple to either J_1 or J_2 first. Together they sum up to a total angular momentum of $\mathbf{J} = \mathbf{J}_1 + \mathbf{J}_2$, where the state is written as $(J_1, J_2)_J$.

1.1.3 Energy levels and laser cooling transitions

The submerged-shell structure gives rise to another feature, which is the rich landscape of energy levels. There are at least 672 known energy levels up to the ionization energy of $E^* = 49\,262(5)\,\mathrm{cm}^{-1}$ with an total angular momentum quantum number of $1 \leq J \leq 12$ [27, 28]. Figure 1.1 shows the energy levels of erbium up to $25\,000\,\mathrm{cm}^{-1}$ and some proposed laser cooling transitions [29]. The parity of the states, regarding the electronic wave function ($P\Psi(\mathbf{r}) = \pm\Psi(-\mathbf{r})$), is displayed in red (black), which represents even (odd) parity.

The two uppermost transitions promote an electron from the $6s$ shell to the $6p$ shell ($4f^{12}6s^2 \rightarrow 4f^{12}6s6p$), where both the $6s$ and $6p$ electron couple to either a singlet ${}^1P_1$ state (401 nm) or a triplet ${}^3P_1$ state (583 nm). The other three depicted transitions promote an electron from the $4f$ orbital to the $5d$ orbital ($4f^{12}6s^2 \rightarrow 4f^{11}5d6s^2$), where the final states differ in the jj-coupling.

The broadest of all the sketched transitions in the blue/violet region at 401 nm with a linewidth of $\Delta\nu \approx 30\,\mathrm{MHz}$ is similar to the D_2 line in alkali atoms, which is commonly used for laser cooling. The reason for that being the low lifetime and therefore the high number of scattering events. To quantify the cooling exerted on the atoms, one can define the so called Doppler temperature via $T_\mathrm{D} = \frac{\hbar\Gamma}{2k_\mathrm{B}}$, which is proportional to the transition rate $\Gamma = 2\pi\Delta\nu$. Compared to alkali atoms one does not need a repump laser during the cooling process, due to the transition being closed. This means, that there is no, or at least very little transfer of population to a different sublevel, than the cooling levels. Population in other levels may decay to other sublevels in the ground state and be lost from the cooling cycle. Considering all this makes the 401 nm line a good candidate for the use in a Zeeman slower (ZS) and general cooling/imaging of the atoms.

The next transition is an intercombination line in the yellow at 583 nm with a rather narrow linewidth of $\Delta\nu \approx 180\,\mathrm{kHz}$, which is conveniently suited for implementing a narrow line magneto-optical trap (MOT) with a Doppler temperature as

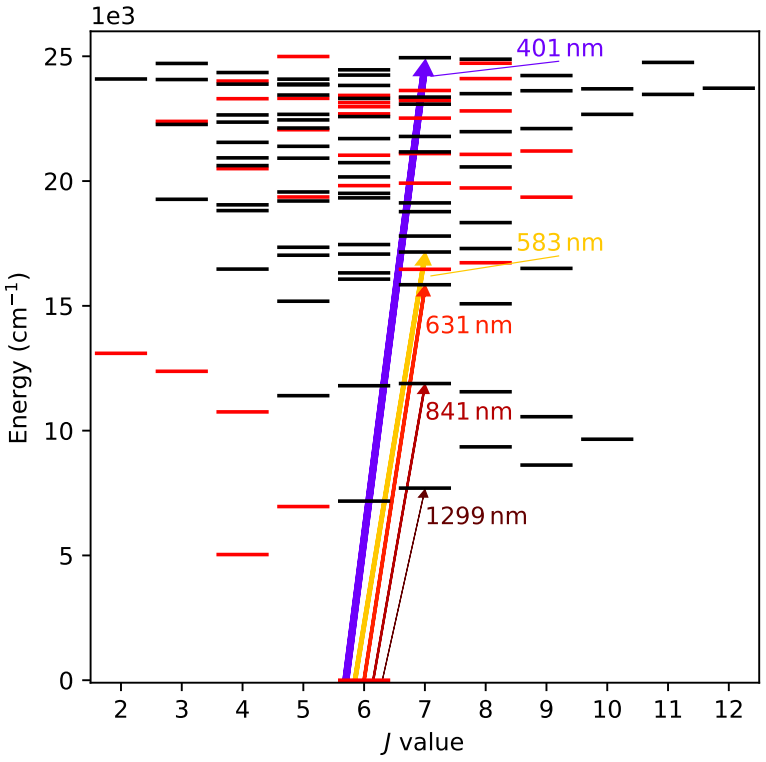

Figure 1.1: Energy spectrum of erbium up to 25 000 cm^{-1}, where red (black) lines denote even (odd) parity states. It shows the $J = 6$ ground state and five proposed laser cooling transitions. The two most important ones being the 401 nm and 583 nm transition used for the Zeeman slower and the MOT light, respectively. The laser system described later in Sec. 4 is relying on the 631 nm transition, which can be used for spin manipulation. A second stage MOT was recently implemented using the 841 nm transition [19], while the 1299 nm transition was also recently observed and characterized [30]. The thickness of the transition lines give an indication on the linewidth relative to each other.

low as $T_\mathrm{D} \approx 4.6\,\mu\mathrm{K}$ [31]. The comparably low Doppler temperature with respect to alkali MOTs allows for a direct loading into a optical dipole trap without any Sub-Doppler cooling mechanisms.

Another proposed laser cooling transition is in the red at 631 nm with a linewidth of $\Delta\nu \approx 28\,\mathrm{kHz}$ and a state configuration of $4f^{11}(^4\mathrm{I}^o_{13/2})\,5d_{3/2}\,6s^2\,(13/2, 3/2)^o_7$. This transition is the starting point for the laser system which is described and built up in Sec. 4. In the experiment it could be used to further cool down after the MOT stage or to implement some spin preparation schemes.

The last two transitions in the IR-A at 841 nm and 1299 nm were just recently

employed in two experiments. The former was used as an even narrower second-stage MOT after the common 583 nm MOT. By this they achieved sub-second production of a medium sized Bose-Einstein condensate (BEC) of erbium [19]. The latter was used to do high-resolution spectroscopy on and was found to have a lifetime on the order of a hundred ms in the excited state's lowest magnetic sublevel [30]. This could pave the path to a cleaner implementation of spin mixtures and dipolar physics in big spin manifolds in general.

1.2 Generic interactions in (ultracold) atomic systems

1.2.1 Atom-light interaction

Revisiting an atom positioned in a monochromatic light field $\mathbf{E}$, oscillating with a frequency $\omega_\mathrm{L} = 2\pi\frac{c}{\lambda}$, which can be written as

$$\mathbf{E} = \frac{1}{2}\varepsilon(\mathbf{r})e^{-i\omega_\mathrm{L}t+i\phi(\mathbf{r})} + \text{c.c.}\ , \tag{1.1}$$

with a field amplitude $\varepsilon(\mathbf{r})$ and a phase $\psi(\mathbf{r})$. This oscillating light field induces a dipole moment $\mathbf{d}$ in the atom corresponding to

$$\mathbf{d} = \alpha(\omega_\mathrm{L})\mathbf{E}\ , \tag{1.2}$$

with the (anisotropic) complex polarizability of the atom $\alpha(\omega_\mathrm{L})$. The total light shift (ac Stark shift) exerted on the atom is given by

$$U_\mathrm{dip}(\omega_\mathrm{L},\mathbf{r}) = -\frac{1}{2}\mathbf{E}^\dagger\alpha\mathbf{E} = -\frac{1}{2\varepsilon_0 c}\mathrm{Re}\{\alpha(\omega_\mathrm{L})\}I(\mathbf{r})\ , \tag{1.3}$$

with the vacuum permittivity ε_0 and the intensity of the light field $I(\mathbf{r}) = \frac{1}{2\varepsilon_0 c}|\mathbf{E}|^2$. Assuming a simple two level model and a laser which is detuned close to an atomic transition one may apply the rotating wave approximation and obtain approximations for the potential and the scattering rate

$$U_\mathrm{dip}(\mathbf{r}) = \frac{3\pi c^2}{2\omega_0^3}\frac{\Gamma}{\Delta}I(\mathbf{r}) \quad\text{and}\quad \Gamma_\mathrm{scatt} = \frac{3\pi^2c^2}{h\omega_0^3}\left(\frac{\Gamma}{\Delta}\right)^2 I(\mathbf{r})\ . \tag{1.4}$$

Here, ω_0 denotes the atomic transition frequency and $\Delta = \omega_\mathrm{L} - \omega_0$ is called detuning. Looking closely on the expression of the dipole potential we can see, that it is inversely proportional to Δ. This allows for a repulsive potential for a blue detuned laser $\Delta > 0$ and for an attractive potential for red detuning $\Delta < 0$. One has to keep in mind though, that the scattering rate is proportional to $1/\Delta^2$, decreasing the scattering rate for a large detuning, but also decreasing the potential depth. It is like in many systems a trade-off between different properties.

In general the total light shift is given by [32]

$$U(\omega_\mathrm{L}, \mathbf{r}) = -\frac{1}{2\varepsilon_0 c} I(\mathbf{r}) \Big[\alpha_\mathrm{scal}(\omega_\mathrm{L}) + |\mathbf{u}^* \times \mathbf{u}| \cos(\vartheta_k) \frac{m_J}{2J} \alpha_\mathrm{vect}(\omega_\mathrm{L}) + \frac{3m_J^2 - J(J+1)}{J(2J-1)} \frac{3\cos^2(\vartheta_p) - 1}{2} \alpha_\mathrm{tens}(\omega_\mathrm{L}) \Big] , \quad (1.5)$$

with the three contributions of the total polarizability $\alpha = \alpha_\mathrm{scal} + \alpha_\mathrm{vect} + \alpha_\mathrm{tens}$ being the scalar, vectorial and tensorial part respectively. The scalar term of the potential is present for any type of polarization $\mathbf{u}$, whereas the vectorial term can be zero if the light is linearly polarized and it can be arbitrarily tuned by the angle θ_k, which lies between the polarization axis and the direction of propagation. It also features a dependence on the magnetic quantum number m_J and the total angular momentum J. The tensorial term has a quadratic dependence on the magnetic quantum number and additionally depends on the angle between the polarization axis and the quantization axis. It vanishes if the angle is $\theta_k^* = 54.7°$, or if $J = 1/2$. The tensorial term is always zero for alkali atoms, due to the condition $J = 1/2$ being fulfilled. For erbium however it adds the possibility to selectively manipulate the sublevels m_J and much more complexity in the potential in general.

Figure 1.2 shows the calculated total atomic polarizability of erbium in the ground state in atomic units in green. The inset shows the configuration of the light and magnetic field with the angles being $\theta_k = \theta_p = \pi/2$. The three blue dots show polarizability measurements at three important wavelength currently used in the experiment for dipole traps - 532, 1064 and 1570 nm. Above 400 nm the polarizability is mainly red detuned, whereas below that it's mainly blue detuned.

As one can see, the left side at high wavelength shows a region with less transitions and an acceptable positive polarizability. Therefore it is very convenient to use lasers with wavelengths in this region to create attractive potentials for applications

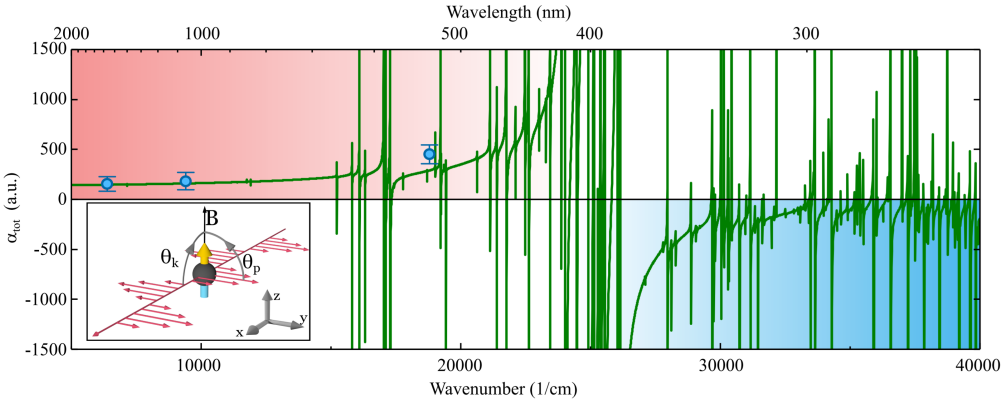

Figure 1.2: Calculated total atomic polarizability of erbium in the ground state from 200 to 2000 nm for $\theta_k = \theta_p = \pi/2$ in green. The blue dots depict measurements at the wavelengths 532, 1064 and 1570 nm. The red/blue shaded area emphasizes the general red-/blue-detuned trend of the polarizability. The inset shows the configuration in the experiment. Figure from Ref. [32].

such as dipole traps and lattices. The right side however is mostly blue detuned and would be suited for repulsive potentials, such as for example box potentials or ring potentials.

1.2.2 Magnetic moment and Landé g-factor

Another effect due to the submerged-shell structure is the high total angular momentum quantum number $J = 6$. Bosonic erbium does not have a nuclear spin and therefore, if placed in an external field the submanifold consists of the magnetic quantum numbers m_J ranging from $-J$ to $+J$. With these we can write the magnetic moment of a bosonic atom as

$$\mu_{\text{bos}} = m_J g_J \mu_{\text{B}} \tag{1.6}$$

with the Landé g-factor g_J and μ_{B} the Bohr magneton. The Landé g-factor can be calculated via

$$g_J = 1 + (g_S - 1)\frac{J(J+1) - L(L+1) + S(S+1)}{2J(J+1)} \tag{1.7}$$

within pure LS-coupling and with $g_S \approx 2.0023$. Applying some needed corrections, see e.g. Ref. [33], actually yields a value close to the experimentally

observed one $g_J = 1.163801(1)$. Finally the atomic magnetic moment evaluates to $\mu_{\text{bos}} = 6.982806(6)\,\mu_{\text{B}}$ with $(J, m_J) = (6, -6)$. For the fermionic isotope one needs to consider the new good quantum number F due to the non-zero nuclear spin, with another g-factor

$$g_F = g_J \frac{F(F+1) - I(I+1) + J(J+1)}{2F(F+1)}\,, \tag{1.8}$$

which gives $g_F = 0.735032(1)$ for $F = 19/2$ and $I = 7/2$ and the same magnetic moment in the lowest hyperfine state $(F, m_F) = (19/2, -19/2)$.

1.2.3 Interaction with magnetic fields - Zeeman shift

When applying a magnetic field B, the magnetic submanifold of m_J (m_F) states will split into $2J+1$ ($2F+1$) levels for bosons (fermions). The Zeeman effect shifts the energy of the ground state substates as

$$\Delta E^{\text{bos}}_{m_J,\text{Zeeman}}(B) = m_J g_J \mu_{\text{B}} B \tag{1.9}$$

for the bosonic isotopes of erbium, which accounts for an overall linear shift of the energies. For the fermionic isotope however, the Paschen-Back effect decouples the total angular momentum **J** and the nuclear spin **I** and forces a quadratic energy splitting onto the linear one. For low magnetic field strength, i.e. a couple of Gauss, the linear relation only produces an error in the kHz range.

In Fig. 1.3 we show the linear splitting of the Zeeman sublevels of bosonic erbium for low magnetic field up to 5 G, which ends up being on the order of MHz between single substates.

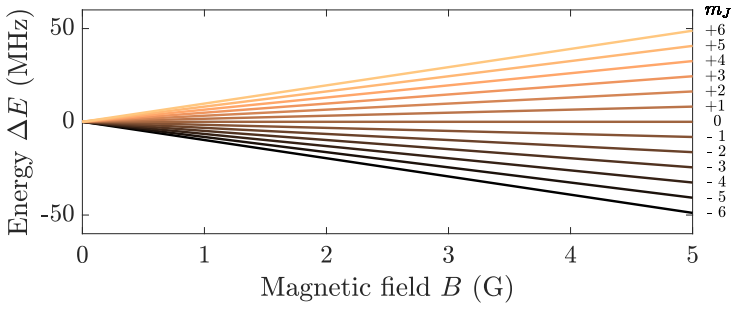

Figure 1.3: Zeeman splitting of bosonic erbium in the ground state submanifold for a low magnetic field up to 5 G.

1.3 Ultracold quantum gases

Since the observation of the first Bose-Einstein condensates (BEC) in 1995 [1, 2], the interest in ultracold quantum gases was on the rise. To date, 14 different atomic species have been condensed in different labs around the world using increasingly advanced technology, with the latest competitor being thulium in 2020 [34]. Decades later, BECs still provide a versatile platform for many research groups working in different fields of quantum physics.

1.3.1 Production of ultracold erbium quantum gases

The generation of degenerate quantum gases of erbium is realized in a vacuum apparatus, which can be separated into two regions, see Fig. 1.4. The first region (high vacuum) consists of a high temperature oven, a transversal cooling section, a pumping stage and an atomic beam shutter. The second region (ultra-high vacuum) shows the Zeeman slower, the main science chamber, a pumping section and the Zeeman slower light viewport.

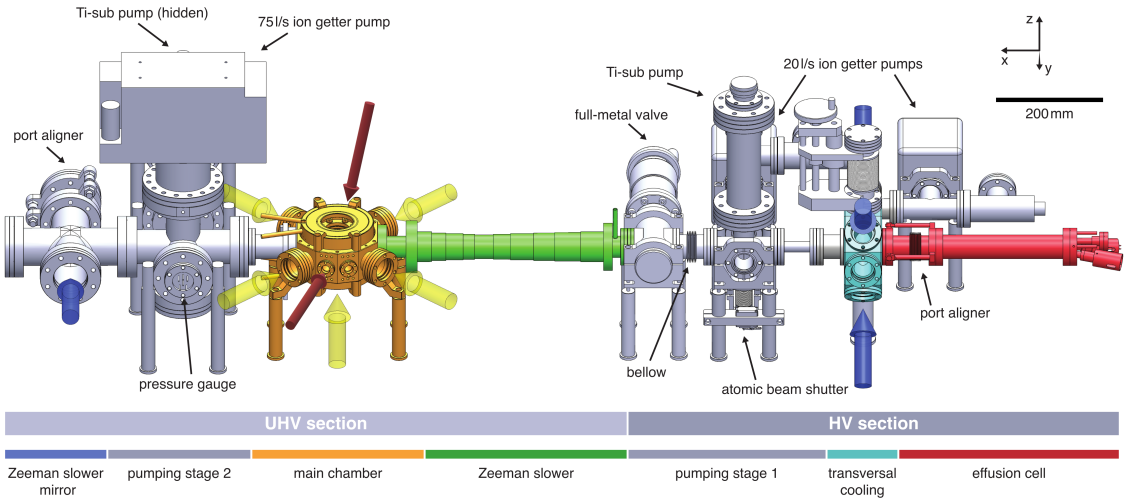

Figure 1.4: Experimental apparatus of the ERBIUM lab. Atoms travel from the oven/effusion cell on the right to the main chamber on the left. On their way they get cooled transversally and in the direction of propagation by the blue light. After the Zeeman slower, the atoms are trapped and accumulated in a yellow 5-beam magneto-optical trap. From there, they are loaded into an optical dipole trap and evaporatively cooled to degeneracy. Figure adapted from Ref. [35].

The oven consists of an effusion cell holding a small chunk of erbium and is operated at around 1200 °C, just $\sim$ 300 °C below erbium's melting point at $T_{\mathrm{m}} = 1529^{\circ}$ [36]. It produces a hot beam of atoms, which is collimated and transversally cooled directly after. Two retroreflected high aspect ratio laser beams red detuned from the 401 nm transition form a two-dimensional optical molasses.

After passing the pumping and beam shutter section, the atomic beam enters the Zeeman slower, which decelerates the atoms from a couple of 100 m/s down to a few m/s, allowing an efficient loading of the MOT. To decelerate the atoms the Zeeman slower utilizes the Zeeman shift, which compensates the Doppler shift coming from the finite velocity of the atoms. While light is scattered the atoms are slowed down and the Doppler shift is effectively getting less, requiring a weaker magnetic field to compensate it. The atoms arrive in the main chamber after the ZS, where the magneto-optical trap is formed by 5 yellow laser beams and a quadrupole magnetic field. Two horizontal pairs of beams and one beam from the bottom allow for a similar loading rate of the MOT compared to the standard 6-beam MOT used for alkali atoms. That is due to the high mass of the erbium atoms and the narrow 583 nm line creating a spin polarized sample in the lowest Zeeman state [37]. After a couple of seconds of ZS and MOT operation, the MOT gets compressed (cMOT) by reducing the intensity and the detuning of the light, increasing density and decreasing temperature before the transfer of the atoms into a conservative trap.

As a conservative trap we use a far-detuned optical dipole trap (ODT), created at the crossing point of two tightly focused laser beams, which are generated by a high-pwer 1064 nm laser depicted by the dark red arrows around the main chamber. After a couple of ms loading time into the dipole trap, the cMOT is switched off and the atoms are now trapped in the conservative potential. From there on, the atoms are cooled by means of forced evaporation, which is done by nearly exponentially reducing the power of the trapping beam, so that the hottest/fastest atoms escape the trap and the rest rethermalizes to a lower temperature. A couple of seconds and only a small fraction of remaining atoms later, the critical temperature for the onset of forming a condensate is met (a couple 100 nK). The atoms start to accumulate in the lowest quantum state (ground state) and form a macroscopic coherent object.

1.3.2 Bose-Einstein condensation

The quantum statistics of a Bose-Einstein condensate (BEC) are intimately tied to the behavior of identical bosonic particles, which follow Bose-Einstein statistics. These statistics govern how these particles occupy quantum states and play a fundamental role in the formation of a BEC. Unlike fermions, which obey Fermi-Dirac statistics and follow the Pauli exclusion principle, bosons can occupy the same quantum state simultaneously, which allows the macroscopic occupation of one state. In the context of a BEC, the quantum statistics manifest as the tendency of bosons to condense into the lowest-energy state. At low temperatures, the majority of bosons gather in this state, forming the condensate.

To understand the statistics behind a BEC, we can examine the distribution of bosons in all energy states. At thermal equilibrium, the probability of finding a boson in a particular energy state is given by the Bose-Einstein distribution

$$\langle n_i \rangle = g_i \frac{1}{e^{\beta(E_i-\mu)} - 1} \ . \tag{1.10}$$

Here, $\langle n_i \rangle$ represents the average number of bosons in the state with energy E_i, g_i is the degeneracy of the state i, μ is the chemical potential, and $\beta = 1/k_\mathrm{B}T$ is inversely proportional to the Boltzmann constant k_B and temperature T.

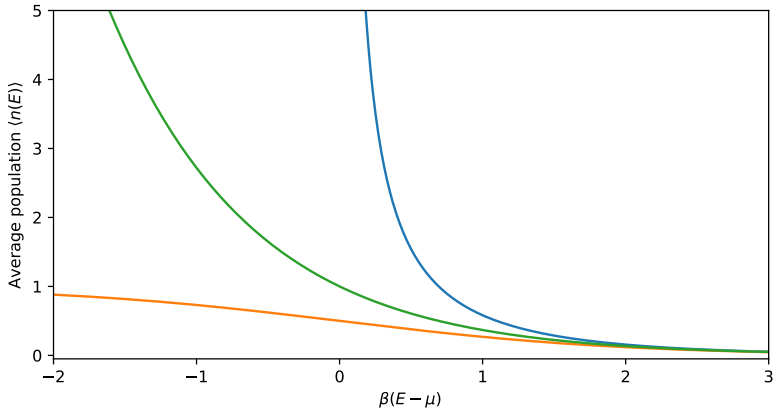

Figure 1.5: Various types of distributions. The Bose-Einstein-distribution in blue diverges to infinity when approaching zero in the exponent. The Fermi-Dirac distribution in orange is $\frac{1}{2}$ at 0 and approaches 1 at $-\infty$. The Maxwell-Boltzmann distribution in green corresponds to the classical limit.

At high temperatures, where the thermal energy is much larger than the energy

of the states ($k_B T \gg E_i$), the exponential term dominates and the distribution approaches the classical Maxwell-Boltzmann distribution, as shown in Fig. 1.5. In this regime, bosons are distributed among different energy levels according to their respective energies.

However, as the temperature decreases, the exponential term in the Bose-Einstein distribution becomes countable, and when the temperature approaches absolute zero ($T \to 0$), the distribution undergoes a dramatic change. At $T = 0$, the exponential term approaches 1, resulting in a divergent distribution for the mean population. This implies that an increasing number of bosons occupy the lowest energy state, leading to the formation of a BEC.

To put the concept of Bose-Einstein condensation into a more physical perspective, particles can be associated with the so-called thermal de Broglie wavelength

$$\lambda_{\mathrm{th}} = \frac{h}{p} = \frac{h}{\sqrt{2\pi m k_{\mathrm{B}} T}} \propto \frac{1}{\sqrt{T}} \ , \tag{1.11}$$

which is inversely proportional to the square root of the temperature T. Here, h is the Planck constant, m the mass of the particle, and k_{B} the Boltzmann constant. The thermal wavelength increases for lower temperatures due to the dependence on T. At the point where the waves become as large as the mean interparticle distance, they start to overlap, and quantum effects and statistics will start to play a role. For ultracold quantum gases the usual parameter quantifying this transition is the phase space density ρ. If the condition

$$\rho = n\lambda_{\mathrm{th}}^3 \geq 2.612 \quad \text{(harmonic trap)} \tag{1.12}$$

is fulfilled, a BEC starts to form and particles will occupy the lowest quantum state. The amount of particles in the BEC (N_0) can be described by the BEC fraction

$$\frac{N_0}{N} = 1 - \left(\frac{T}{T_{\mathrm{c}}}\right)^3 \ , \tag{1.13}$$

where N is the total amount of atoms of the condensed and thermal part and T_{c} is the critical temperature of the system. At a temperature of half the critical temperature, a BEC fraction of $\sim 88\,\%$ is already reached, which is shown in Fig. 1.6 on the left (green).

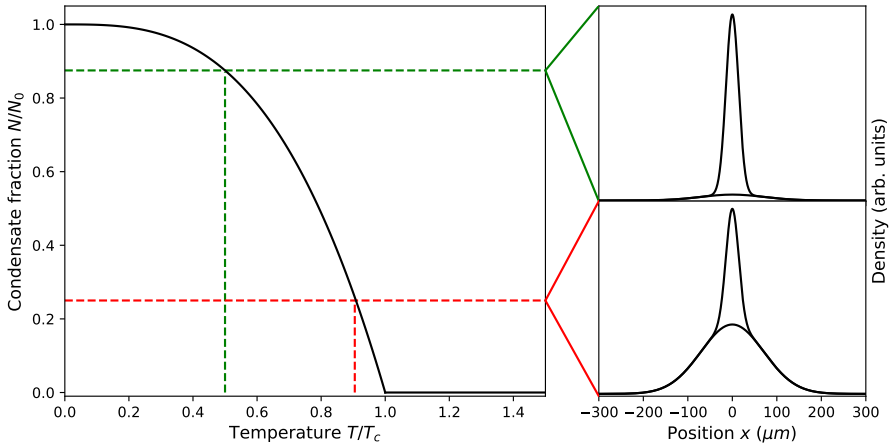

Figure 1.6: (left) Condensate fraction of a BEC when the temperature T is below the critical temperature T_c, following Eq. 1.13. (right) Usual radially integrated bimodal density profile of a partial BEC at $(0.9, 0.5)$ T/T_c (red, green). The underlying Gaussian depicts the thermal part, which is not condensed yet, whereas the sharp peak is all the atoms occupying the lowest energy state.

1.3.3 Contact interaction

The most common interaction between two uncharged particles can be described in a simplified way by the attractive part of a Lennard-Jones potential, which reads

$$U_\mathrm{LJ} = -\frac{C_6}{r^6}\,, \tag{1.14}$$

with r being the interparticle distance and C_6 the van-der-Waals coefficient. Here, we omit the repulsive part, because it only plays a role at very small particle separations.

However, in scattering theory, an incoming wave is generally described as a plane wave $e^{i\mathbf{k}\cdot\mathbf{r}}$ that scatters into an outgoing spherical wave with a scattering amplitude $f(\vartheta)$, which leads to the scattering wave function $\psi(\mathbf{r}) = \mathrm{e}^{i\mathbf{k}\cdot\mathbf{r}} + f(\vartheta)\,\mathrm{e}^{ikr}/r$. In the limit of low energy scattering [38], i.e. $k \to 0$, only the s-wave channel contributes to the scattering amplitude and we can therefore approximate the interaction potential as a delta-like pseudo-potential [39]

$$U(\mathbf{r}_1 - \mathbf{r}_2) = g\delta(\mathbf{r}_1 - \mathbf{r}_2), \text{ with } g = \frac{4\pi\hbar^2 a_\mathrm{s}}{m}. \tag{1.15}$$

Here, g is called the contact coupling constant, and a_s is the s-wave scattering length. The sole dependency on one parameter is a huge advantage, because it

allows one to easily change the interaction strength by only varying one physical quantity.

To illustrate the effect of the interaction strength onto a BEC we cover this topic already here instead of in Sec. 2.4, where the Gross-Pitaevskii equation is fully explained.

For a sufficiently large interaction strength and high number of atoms, one can use the Thomas-Fermi approximation to describe a BEC. It states that we can neglect the kinetic energy term, due to the high interaction strength. Dropping the kinetic energy from the equation results in a simple inverse parabola shape of the condensate. Atoms are confined within the Thomas-Fermi radius $r_{\mathrm{tf}} = \sqrt{\frac{2\mu}{m\bar{\omega}^2}}$, with μ the chemical potential and $\bar{\omega}$ the mean trap frequency. Using the full GPE it softens the edges and creates a smooth density distribution; see Fig. 1.7 on the right. The left side of the plot shows the widening of the condensate when increasing the interaction strength, ergo it is getting more repulsive.

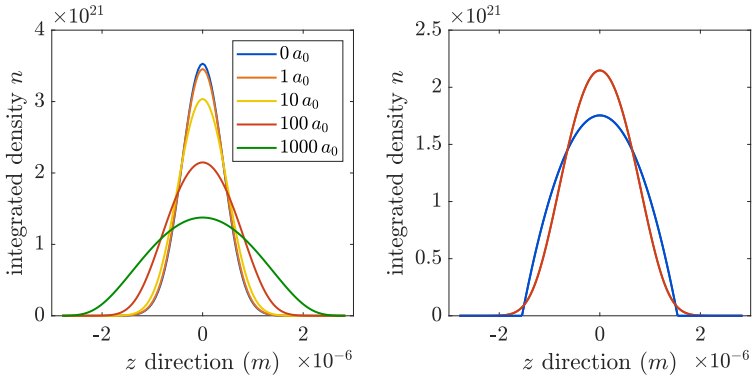

Figure 1.7: The left plot shows integrated densities of a 3D BEC for different scattering lengths. The higher the scattering length, the wider the condensate, due to the increasingly repulsive interaction. The right plot shows the Thomas-Fermi approximation at 100 a_s in blue and the GPE solution in red. The condensate shape becomes an inverted parabola because of those approximations.

1.3.4 Dipole-dipole interaction

As erbium is a highly magnetic atom, there is an additional interaction to consider, the dipole-dipole interaction. In general, the interaction between two dipoles pointing along $\mathbf{e}_1$ and $\mathbf{e}_2$ at positions $\mathbf{r}_1$ and $\mathbf{r}_2$ ($\mathbf{r} = \mathbf{r}_1 - \mathbf{r}_2$) can be described by the interaction potential

$$U_{\mathrm{dd}}(\mathbf{r}) = \frac{C_{\mathrm{dd}}}{4\pi} \frac{r^2(\mathbf{e}_1 \cdot \mathbf{e}_2) - 3(\mathbf{e}_1 \cdot \mathbf{r})(\mathbf{e}_2 \cdot \mathbf{r})}{r^5} \tag{1.16}$$

with the dipolar coupling constant $C_{\mathrm{dd}} = \mu_0 \mu_1 \mu_2$. Here, μ_0 is the permeability of vacuum and $\mu_{1,2}$ are the two magnetic dipole moments of the respective atoms. Under the influence of an external magnetic field $\mathbf{B}$, the dipoles will align with the field vector and hence they will be polarized. Under this circumstance and the assumption of two identical particles interacting, meaning $\mu = \mu_1 = \mu_2$, we can simplify the dipole-dipole interaction to

$$U_{\mathrm{dd}}(r, \vartheta) = \frac{C_{\mathrm{dd}}}{4\pi} \frac{1 - 3\cos^2 \vartheta}{r^3} \,. \tag{1.17}$$

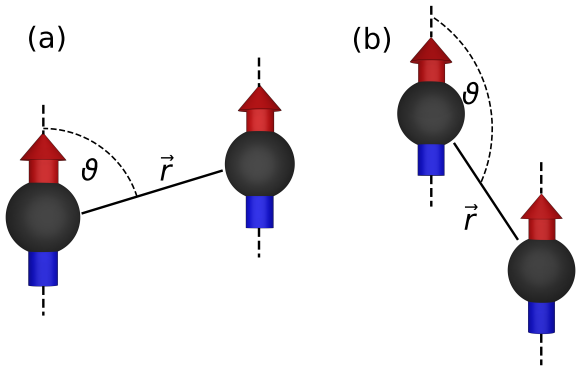

Figure 1.8: (a) Illustration of two dipoles in a rather side-to-side configuration. The DDI is repulsive. (b) Another two dipoles in a more head-to-tail like configuration, where the DDI is attractive.

The angle ϑ is defined by the polarization axis and the interparticle axis, see Fig. 1.8. The dipole-dipole interaction is anisotropic, which means, that for different orientations of the dipoles with respect to the particle axis, the DDI can range from $-2 \cdot \frac{C_{\mathrm{dd}}}{4\pi}$ to $1 \cdot \frac{C_{\mathrm{dd}}}{4\pi}$, see Fig. 1.9. The former extreme is achieved in a so called head-to-tail configuration with ϑ being 0°, whereas the latter is reached in a side-by-side configuration with $\vartheta = 90°$. At a magic angle of $\vartheta_{\mathrm{m}} = 54.7°$ the DDI can be tuned to zero, or at least very close to it [40].

Another feature of the DDI is the long range character in three dimensions ($n = 3$). That is, because the integral over the potential [41]

$$\int_{r_0}^{\infty} \mathrm{d}^n r \, U_{\mathrm{dd}}(\mathbf{r}) \,, \tag{1.18}$$

converges at large distances and therefore gives an extensive energy. In lower dimensional systems though ($n = \{1, 2\}$) the DDI is short range.

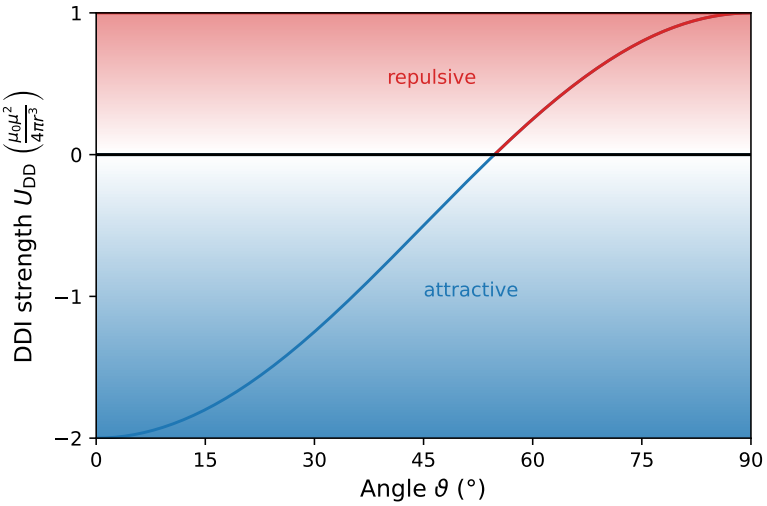

Figure 1.9: Dipole-dipole interaction strength versus the angle ϑ between the inter-particle and polarization axis. For a head-to-tail configuration ($\vartheta = 0°$) the DDI is twice as attractive as repulsive for the side-by-side ($\vartheta = 90°$) configuration. At the magic angle $\vartheta_{\mathrm{m}} = 54.7°$ the DDI strength goes to zero.

As said before, the dipole interaction can be both attractive and repulsive and in many specific geometries of the system, speaking about trap frequencies of an ODT, the DDI can become mostly attractive and therefore counteract the repulsive contact interaction. To quantify this, one can define a lengthscale for dipolar interactions [41]

$$a_{\mathrm{dd}} \equiv \frac{C_{\mathrm{dd}} m}{12\pi\hbar^2} \tag{1.19}$$

which can be related to the contact interaction through the dipolar strength

$$\varepsilon_{\mathrm{dd}} \equiv \frac{a_{\mathrm{dd}}}{a_{\mathrm{s}}} = \frac{C_{\mathrm{dd}}}{3g} \,. \tag{1.20}$$

For $\varepsilon_{\mathrm{dd}} \geq 1$ the system is dominantly dipolar, whereas for $\varepsilon_{\mathrm{dd}} < 1$ it is in the contact dominated regime. For ^{166}Er the dipolar length gives $a_{\mathrm{dd}} = 65.5\,\mathrm{a}_0$ with a_0 the Bohr radius.

When looking at dipolar BECs we find a new behaviour. When put into a circular trap, non dipolar BECs assume the shape of the trap, independent of the orientation of an external magnetic field. Dipolar BECs however, tend to elongate along the direction of the magnetic field, because it wants to minimize its energy. This is called magnetostriction and is illustrated in Fig. 1.10.

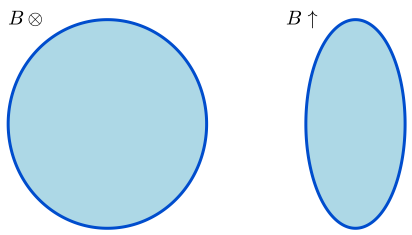

Figure 1.10: Sketch of the concept of magnetostriction. The BEC is in a circular trap and the magnetic field points into the plane, which leaves a circular BEC. If the magnetic field is pointing in the direction of the plane, the BEC restricted by the dipole interaction and gets squeezed/elongated.

1.3.5 Feshbach resonances

Another turning knob of cold atomic gases which utilizes magnetic fields are so called Fano-Feshbach resonances, short FRs, which describe atom-atom collisions in the presence of a magnetic field. To define these resonances one has to take a look at the interaction potentials. The dissociation energy of different channels/potentials can be higher (lower) than the total energy of the two-atom system, which is termed open (closed) channel [42].

Suppose, two atoms collide in the open channel and there is a closed channel with a dissociation threshold energy difference of ΔE higher, as depicted in Fig. 1.11. This closed channel can now contain a vibrational bound state close to zero energy and cause a mixing of the two states, which induces a coupling between the open and closed channel. During the scattering process the closed channel vibrational state is dressed by the coupling to the open channel. The atoms are then momentarily caught in the closed channel and decay back to the open channel after a characteristic time [42]. A single Feshbach resonance is usually modelled by

[43]

$$a_{\mathrm{s}}(B) = a_{\mathrm{bg}}\left(1 + \frac{\Delta}{B - B_0}\right) , \tag{1.21}$$

where a_{bg} is the background scattering length, Δ is the width and B_0 the position of the resonance. In the experiment we can tune ΔE due to the fact, that the magnetic moments of most of the states are different, leading to $\Delta E = (\mu_{\mathrm{closed}} - \mu_{\mathrm{open}})B$. When changing B, two states can be very close to each other and cause the resonant behaviour in the scattering length, as shown in the inset of Fig. 1.11.

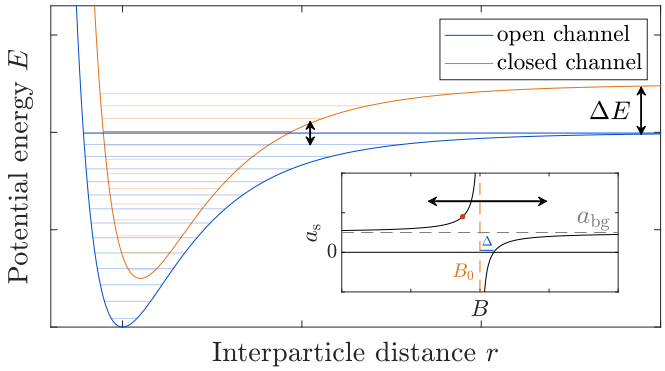

Figure 1.11: Sketch of the two-particle scattering potential (blue, open) and another higher energy bound state potential (orange, closed) with a dissociation threshold energy difference ΔE. When a bound state of the closed channel lies close to the zero energy $E_{\mathrm{B}} \sim 0$, the states get mixed, couple, and eventually cause a scattering resonance in the open channel. The inset shows the behaviour of the scattering length when sweeping the magnetic field B over the resonance. The resonance can be characterized by the background scattering a_{bg}, the resonance position B_0 and the width Δ.

Now erbium has quite a high density of Feshbach resonances [44, 45] compared to alkali atoms, owed to the anisotropy of both the short and long range interactions [46], giving rise to couplings between different molecular channels. Given the large number of molecular potentials together with the couplings results in a very complex Feshbach structure, which cannot be predicted by calculations. The dense Feshbach spectrum of erbium actually has features of quantum chaos [44].

To measure the scattering length of ultracold gases one can employ different techniques, the most common ones being expansion or anisotropic expansion [47] after the release from a trap and measuring the evolution of the size of the cloud in different spatial directions, which allows to calculate the scattering length. Further-

more a technique using cross dimensional re-thermalization was applied recently to measure the scattering length of erbium [48]. After exciting the cloud in one direction, the re-thermalization process is measured on two perpendicular axis. Fitting a hydrodynamic model based on the Enskog equations [49] to the observed evolution of the temperature allows for an accurate determination of the scattering length. A much more sophisticated way to measure the scattering length is based on lattice modulation spectroscopy. The cold gas is loaded into a deep lattice, where it will be in the Mott insulator phase. By periodically modulating the amplitude of the potential one observes a resonance at the frequency which matches the particle-hole excitation gap of the Mott insulator. This is given by the total onsite interaction U, which is the sum of the contact and dipole-dipole onsite interaction. Whilst the former is proportional to the scattering length, the latter can be calculated. The results of the measurement for ^{166}Er are shown in Fig. 1.12 with the lattice modulation spectroscopy data and fit in black. The data of the re-thermalization measurement is depicted by the blue and red data points. More information and details on the measurements, see Ref. [48].

The region from 0 to 3 G is very important for current experiments, because it allows us to change the scattering length quite nicely. Later we will see, that the available scattering length range gives access to a contact dominated regime, as well as a dipolar dominated regime. It is also the region which we use in the experiment for controlling the scattering length in recent Bloch oscillation measurements, which directly compare to simulations, where one just plugs in different values for a_s.

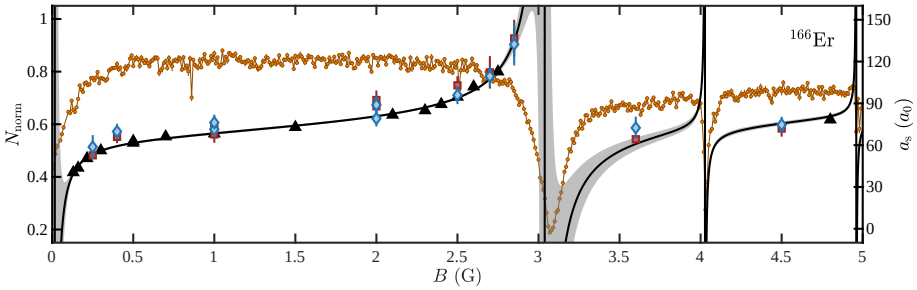

Figure 1.12: Normalized atom number (orange) of a Feshbach scan of ^{166}Er between 0 and 5 G. The black line shows a fit to the triangles, where the scattering length was obtained by lattice modulation spectroscopy. The red and blue data points show recent results from a fit to cross dimensional re-thermalization measurements with the Enskog equations and an analytic formula, respectively. For more information and the figure, see Ref. [48].

Chapter 2

Optical lattices and ground state simulations

A periodic variation of the intensity of laser light is usually referred to as an optical lattice. It comes in different geometries, sizes and colors, speaking about the wavelength of the laser used to create the potential. A basic one dimensional optical lattice is usually formed by either interfering two counterpropagating lasers or interfering them under an angle φ. The former usually gives a smaller lattice spacing $d = \lambda/2$, depending also on the wavelength λ of the laser.

We will now discuss first how optical potentials are created, then describe generally a particle in a periodic potential with different depths and move on to many body physics in optical lattices. More specifically, we will go into mean-field descriptions of many-body systems, namely the Gutzwiller approach and the Gross-Pitaevskii equation. Both are used nowadays to describe specific systems within the realm of ultracold quantum gases.

2.1 General description

Platform: Optical lattice

To create optical lattices one usually uses red detuned lasers, which are interfered with a counterpropagating one, forming a standing wave. The easiest geometry being a one dimensional lattice, one can also add one or two more interfering laser pairs perpendicular to the first one to create a two or three dimensional lattice.

Interfering three lasers under an angle of 120° creates a honeycomb lattice, which gives rise to new phases.

Optical lattices in general allow to pin atoms to specific locations, resembling a real world crystal lattice structure quite well. Additionally to that, they also allow for a fast change of the potential depth due to easy adjustment of the laser power and provide therefore a handy tool to change interactions. Lattices which are created by interfering lasers under an angle usually allow even to vary the lattice spacing by changing the enclosed angle. From simple models and transitions like the superfluid to Mott insulator transition, to an extended Spin dynamics model and precision measurements of the gravitational constant. Optical lattices seem to be an all-rounder platform for cold atomic gases. But how can we calculate ground states of cold atomic gases within a lattice?

2.1.1 Solution to Schrödinger equation - Bloch waves

To obtain the ground state wave function of a quantum mechanical problem one has to solve the Schrödinger equation (SE), which reads for a free particle in one dimension

$$\hat{H}\phi(x) = -\frac{\hbar^2}{2m}\partial_x^2\phi(x) = E\phi(x) \tag{2.1}$$

with the Hamiltonian being the kinetic energy operator of the system. The general solution to this problem is a plane wave $\phi(x) = e^{ikx}$ with the well known energy dispersion relation $E(k) = \frac{\hbar^2 k^2}{2m}$, with a parabolic shape in k.

When electrons move through a solid they usually *feel* a periodic potential created by all the atomic cores arranged in a crystalline structure. Analogously to that, an optical lattice filled with atoms resembles that natural system quite well. If we now want to solve for the wave function in a periodic potential, such as an optical lattice, the SE becomes

$$\hat{H}\phi(x) = \left[-\frac{\hbar^2}{2m}\partial_x^2 + V(x)\right]\phi(x) = E\phi(x) \tag{2.2}$$

with a periodic potential of the form

$$V(x) = -V_0\cos^2(k_{\mathrm{L}}x) = -sE_{\mathrm{r}}\cos^2(k_{\mathrm{L}}x)\ . \tag{2.3}$$

Here V_0 is the lattice depth and s the lattice depth in recoil energies $E_{\mathrm{r}} = \hbar^2 k_{\mathrm{L}}^2/2m$

of the laser light with $k_\mathrm{L} = \frac{2\pi}{\lambda}$. The solution to this equation are so called Bloch waves

$$\phi_{n,q}(x) = e^{iqx/\hbar} u_{n,q}(x) \quad \text{with} \quad u_{n,q}(x) = u_{n,q}(x+d) \ . \tag{2.4}$$

The Bloch waves are the product of a plane wave and a periodic Bloch function in space $u_{n,q}(x)$ with periodicity d. The parameters $q = \hbar k$ and n denote the quasi momentum and the index of the n-th energy band, respectively.

Using the fact, that the Bloch waves and the lattice potential have the same periodicity and that the potential can be rewritten as $V(x) = -V_0 \cos^2(k_\mathrm{L} x) = -\frac{V_0}{4}(e^{-2ik_\mathrm{L}x} + 2 + e^{2ik_\mathrm{L}x})$, one can easily obtain the Fourier coefficients for the Fourier representation of the potential as $a_0 = -V_0/2$ and $a_{\pm 1} = -V_0/4$, summing up to

$$V(x) = \sum_{j=-1}^{1} a_j e^{2ijk_\mathrm{L}x} \ . \tag{2.5}$$

Analogously to that, we can also write the Bloch functions as a Fourier series

$$u_{n,q}(x) = \sum_{j'=-\infty}^{\infty} c_{j'}^{n,q} e^{2ij'k_\mathrm{L}x} \ . \tag{2.6}$$

Although Bloch functions are complicated functions, with the kinetic energy term

$$\frac{(\hat{p}+q)^2}{2m} u_{n,q}(x) = \sum_{j'=-\infty}^{\infty} \frac{(2j'\hbar k_\mathrm{L} + q)^2}{2m} c_{j'}^{n,q} e^{2ij'k_\mathrm{L}x} \tag{2.7}$$

we can reduce Eq. (2.2) to a linear eigenvalue problem of the matrix Hamiltonian

$$\sum_{j'=-b}^{+b} H_{j,j'} c_{j'}^{n,q} = E_n(q) c_j^{n,q} \quad \text{with} \quad H_{j,j'} = \begin{cases} (2j\hbar k_\mathrm{L} + q)^2/2m - V_0/2 & \text{if } j = j', \\ -V_0/4 & \text{if } |j - j'| = 1, \\ 0 & \text{else.} \end{cases} \tag{2.8}$$

Numerically diagonalizing the Hamiltonian matrix $H_{j,j'}$ yields the eigenvectors $c_{j'}^{n,q}$ with the corresponding energy eigenvalues $E_n(q)$ for a reasonably chosen b as cutoff depending on the number of Bloch bands one desires to compute ($b \sim 10$ within the scope here). For a potential of non-zero amplitude s the continuous energy spectrum splits up at the edge of the Brillouin zone and creates so called band

gaps. For increasing lattice depth the band gaps get larger and the width of the bands itself is getting narrower, see Fig. 2.1.

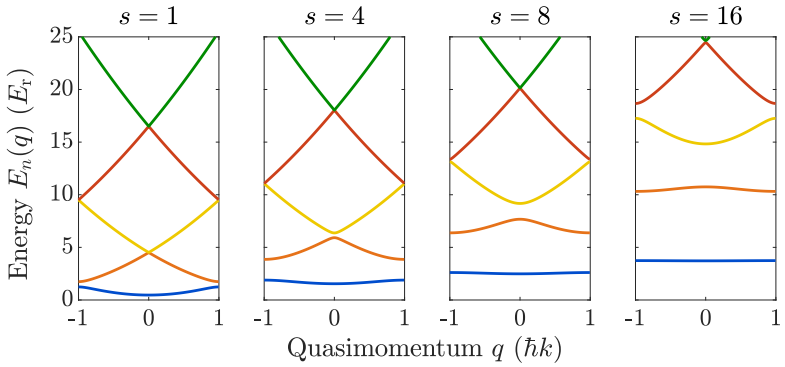

Figure 2.1: Energy of the first five Bloch bands in the first Brillouin zone for increasing lattice depth s from left to right. The deeper the lattice, the flatter the bands become and they get more separated, forming the well known band gaps.

A more quantitative than qualitative approach is depicted in Fig. 2.2, where the first five energy bands are plotted versus the lattice depth V_0 in the natural units E_r of the system. Also the extracted band gap $\Delta E_n(s)$ between the lowest and the n-th band is shown. Already for $s = 2$ the gap between the first and second band is around one photon recoil energy. The spread of the colored energy bands is given in the right panel as well, featuring a fast squeezing of the width $\Delta_n(s)$ for the lowest band.

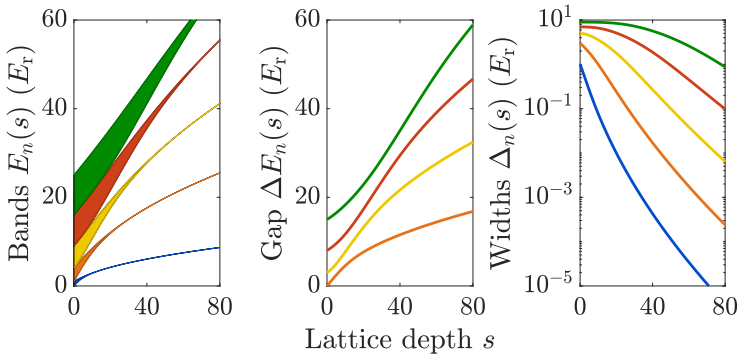

Figure 2.2: (left) First five energy bands $E_n(s)$ for increasing lattice depth. For deeper lattices, the bands get thinner and the band gaps get larger. (middle) Band gap $\Delta E_n(s)$ from the lowest to the n-th band as a function of s. (right) Width of the energy bands $\Delta_n(s)$ depending on the lattice depth.

2.2 Wannier functions and deep lattices

2.2.1 Wannier basis

It is not always very handy to work with Bloch functions, especially when the lattice is deep enough to localize atoms to single lattice sites. Wannier functions are a practical tool, which form an orthogonal set of functions, that are localized to individual lattice sites and can be calculated from the Bloch waves as

$$w_n(x - x_j) = \frac{1}{\sqrt{\aleph}} \sum_q \phi_{n,q}(x) e^{-iqx_j/\hbar} \ . \tag{2.9}$$

In turn, the Bloch waves of the n-th band can also be expressed by the Wannier functions

$$\phi_{n,q}(x) = \frac{1}{\sqrt{\aleph}} \sum_j w_n(x - x_j) e^{iqx_j/\hbar} \ . \tag{2.10}$$

Here, $\aleph$ is a normalization factor and x_j is the position of the j-th lattice site, or in other words, the j-th minimum of the periodic potential.

From the definition of the Wannier functions, one can deduce, that the global phase is not fixed, similar to the Bloch functions, and can therefore be randomly chosen. But it has been shown, that there is one and only one unique phase, which yields a Wannier function $w_n(x)$ that is real, (anti-)symmetric around $x = 0$ or $x = d/2$ and falls off exponentially faster than for any other choice of phase [50]. These Wannier functions are maximally localized and are suited for the description of interacting systems, where interactions between particles on the same or neighbouring lattice sites play a crucial role in the dynamics.

In Fig. 2.3 these localized Wannier functions of the lowest energy band are shown for different lattice depths. For a shallow lattice, Wannier functions possess wings, which create a finite overlap with another particle, if it was to exist on the neighbouring lattice site. This finite overlap is responsible for a non-zero tunneling matrix element J, which can be calculated by means of an overlap integral of neighbouring sites i and j

$$J = \int \mathrm{d}x \, w_n(x - x_i) \left[-\frac{\hbar^2}{2m} \partial_x^2 + V(x) \right] w_n(x - x_j) \ . \tag{2.11}$$

Another alternative way to calculate J is to consider the width of the lowest energy

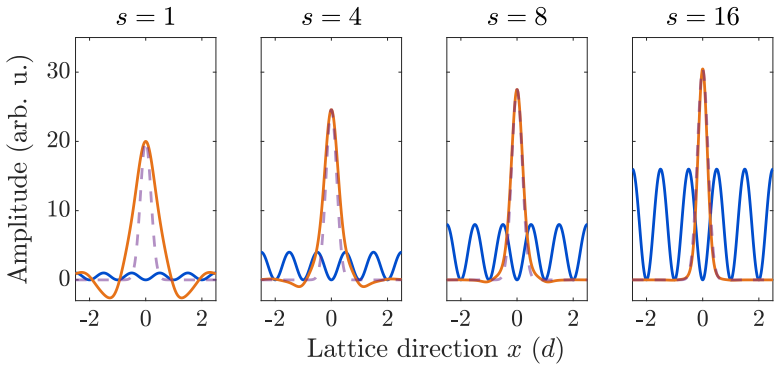

Figure 2.3: Overview of the lowest Bloch band Wannier function (orange) for different lattice depths s. The lattice potential is depicted in blue and the Gaussian harmonic oscillator approximation is plotted as the dashed line. For a shallow lattice the Wannier function has a non-negligible overlap to neighbouring lattice sites. The deeper the lattice, the less overlap, i.e. the more localized the wave function gets. Also the Gaussian approximation works much better in the deep lattice limit, than in the shallow lattice regime.

band [51] and following the relation

$$J = \frac{1}{4}\left(\max_q E_0(q) - \min_q E_0(q)\right) \ . \tag{2.12}$$

The tunneling matrix element is an important quantity for many experiments and much more important is the fact, that it is easily tunable by changing the lattice depth via varying the laser power.

2.2.2 Gaussian approximation

One approximation which is often made for deep lattices is to assume a harmonic potential on each lattice site $V(x \approx x_j) \approx \frac{1}{2}m\omega_{\text{latt}}(x - x_j)^2$ and that the gas is in the ground state of this harmonic oscillator. We approximate the Wannier function in this harmonic potential on site j with trap frequency $\omega_{\text{latt}} = 2\sqrt{s}\frac{E_\text{r}}{\hbar}$ to be of the functional form

$$w_{\text{ho}}(x - x_j) = \frac{1}{\sqrt{\sqrt{\pi} l_{\text{latt}}}} e^{-(x-x_j)^2/(2l_{\text{latt}}^2)} \ , \tag{2.13}$$

with the harmonic oscillator width $l_{\text{latt}} = \sqrt{\frac{\hbar}{m\omega_{\text{latt}}}}$. For deep enough lattices, i.e. $V_0/E_\text{r} \gg 1$, where Wannier functions show very little overlap, they are quite well approximated by Gaussians, see Fig. 2.3. Though, it gives ideally estimates and

is most of the time not suited to describe the full system. The harmonic oscillator approximation does not account for the finite curvature of the bands, which remains even for deep lattices.

2.3 Gutzwiller approach

The Gutzwiller Ansatz was first introduced by Martin C. Gutzwiller in 1963 trying to explain the ferromagnetism in a metal via a new Ansatz for the wave function [52]. Later in the 90's the Gutzwiller wave function was adapted to bosonic systems [53, 54]. In general, the Gutzwiller wave function is found in systems with Hubbard-type Hamiltonians like the Bose-Hubbard (BH) Hamiltonian [55]

$$\hat{H}_{\mathrm{BH}} = -J \sum_{\langle i,j \rangle} \hat{a}_i^\dagger \hat{a}_j + \frac{U}{2} \sum_i \hat{n}_i(\hat{n}_i - 1) + \sum_i \mu_i \hat{n}_i \ . \tag{2.14}$$

Here, J denotes the tunneling matrix element, U is the onsite interaction and μ_i is the chemical potential on the lattice site i. The Hamiltonian is written in second quantization and therefore the operators $\hat{a}_i$ ($\hat{a}_i^\dagger$) are the bosonic annihilation (creation) operator which together give the number operator $\hat{n}_i = \hat{a}_i^\dagger \hat{a}_i$. In these kind of systems the total atom number is given by $\sum_i \hat{n}_i = N$. The tunneling matrix element is defined as $J = -\int \mathrm{d}\mathbf{x} w(\mathbf{x}-\mathbf{x}_i)[-\hbar^2\nabla^2/2m + V_{\mathrm{latt}}(\mathbf{x})]w(\mathbf{x}-\mathbf{x}_j)$. The first term is summed up over neighboring lattice sites and usually tends to delocalize the atoms over the lattice. The second term accounts for the interaction of atoms on the same lattice site and quantifies the energy paid by the system to have multiple atoms on one lattice site. The interaction is defined as $U = 4\pi\hbar^2 a_{\mathrm{s}}/m \int \mathrm{d}\mathbf{x}|w(\mathbf{x})|^4$ and usually localizes atoms to lattice sites. The last term gives an energy offset for every individual lattice site, which is $\mu_i = V_{\mathrm{ext}}(\mathbf{x}_i) - \mu$ with usually an external harmonic confinement V_{ext} and the chemical potential μ.

Coming back to the Gutzwiller wave function, it will be able to nicely capture two regimes of the BH model, the shallow lattice regime where $U/J \ll 1$ and the deep lattice regime where $J/U \ll 1$. Finally it is able to roughly predict the phase transition points in the case of three dimensions and calculate the phase diagram of the BH model within the mean-field description [56].

2.3.1 Gutzwiller wave function

The Gutzwiller wave function is a product state of the single particle wave functions on each lattice site and takes the form

$$|\Psi_{\mathrm{GW}}\rangle = \prod_i |\Psi_i\rangle \tag{2.15}$$

with

$$|\Psi_i\rangle = \sum_{n=0}^{n_{\mathrm{cut}}} g_n^{(i)} |n\rangle_i \ , \tag{2.16}$$

where $|n\rangle_i$ is the Fock state of n atoms on site i, n_{cut} sets the cut off on the maximum number of atoms occupying a single site and $g_n^{(i)}$ are complex coefficients defining the probability amplitude of having n atoms on site i. The coefficients are normalized to one $\sum_n |g_n^{(i)}|^2 = 1$. As said before, the Gutzwiller Ansatz can predict the onset of a Mott insulator lobe as seen in Fig. 2.4. For the first lobe ($\mathrm{MI}_{n=1}$) the approach yields a critical point of $(J/U)_c = 1/(5.8z)$ with z being the number of nearest neighbors of a lattice site [56]. This critical point is quite off for lower dimensions, but gets much better for higher dimensions. In the limit of $J/U \to 0, \infty$ the Gutzwiller approach yields exact results. For a high J/U it will give a superfluid (SF) ground state with delocalized atoms all over the lattice, as depicted by the gray region in Fig. 2.4. The blue regions, on the contrary, sketch out the region where the many-body ground state is a product of Fock states $|n\rangle$, a so called Mott insulator (MI). These two limits can be written down in the corresponding ground states

$$|\Psi_{\mathrm{SF}}\rangle \propto \left(\sum_{i=1}^{L} \hat{a}_i^\dagger\right)^N |0\rangle \quad \text{and} \quad |\Psi_{\mathrm{MI}_n}\rangle \propto \prod_{i=1}^{L} (\hat{a}_i^\dagger)^n |0\rangle \ , \tag{2.17}$$

for N atoms distributed across L lattice sites or a Mott insulator with a commensurate filling of n atoms on each lattice site.

To calculate the ground state of the system one has to minimize the energy $\langle\Psi_{\mathrm{GW}}| \hat{H}_{\mathrm{BH}} |\Psi_{\mathrm{GW}}\rangle$ in order to get the coefficients $g_n^{(i)}$. There are two important parameters which we want to calculate afterwards, which read

$$\bar{n}_i = \sum_n n|g_n^{(i)}|^2 \quad \text{and} \quad \varphi_i = \langle\hat{a}_i\rangle = \sum_n \sqrt{n+1} g_n^{*(i)} g_{n+1}^{(i)} \tag{2.18}$$

and correspond to the mean atom number and the order parameter respectively.

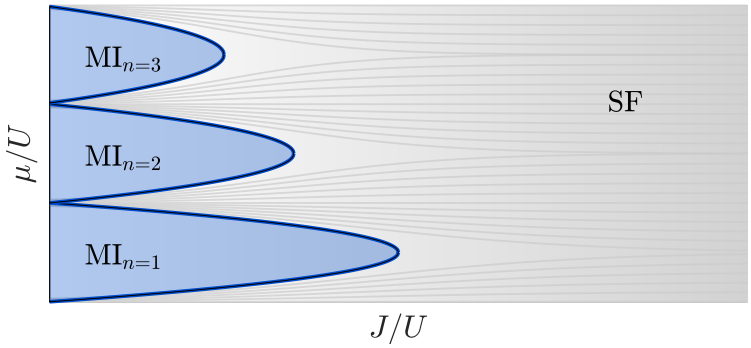

Figure 2.4: Sketch of the phase diagram of the Bode-Hubbard Hamiltonian $\hat{H}_{\mathrm{BH}}$ with μ/U vs. J/U. For a shallow lattice with high J/U the ground state is a superfluid (SF) state with delocalized atoms (gray region). For deeper lattices and smaller J/U the ground state is a Mott insulator (MI) with a specific number of atoms n per lattice site depending on the μ/U ratio (blue regions). The gray lines depict contour lines of $\bar{n}$ which will be followed if J/U is varied for a fixed $\bar{n}$.

In the following we show ground state calculations of a 3D system with lattice spacings $d_{x,y} = 256\,\mathrm{nm} = d_z/2$. The lattice potential is complemented with a harmonic confinement of trapping frequencies $\omega_{x,y} = 2\pi \cdot 60\,\mathrm{Hz} = \omega_z/3$. The lattice depths were always chosen to fulfill $s_{x,y} = s_z/4$ to obtain the same lattice depth V_0 in every spatial direction. The total external potential can therefore be written as

$$V_{\mathrm{ext}}(\mathbf{x}) = \sum_{\xi=x,y,z} s_\xi E_{\mathrm{r}}^\xi \sin^2\left(k_\xi \xi\right) + \frac{1}{2} m \omega_\xi^2 \xi^2 \ , \tag{2.19}$$

with the wavenumber $k_\xi = \pi/d_\xi$ and the recoil energy $E_{\mathrm{r}}^\xi = \hbar^2 k_\xi^2/2m$. The scattering length was set to $60\,\mathrm{a_0}$, while the mass was taken to be that of $m = m(^{168}\mathrm{Er})$. Although erbium is highly dipolar, we omit this fact to keep things simple for now.

2.3.2 Results of ground state calculations

The first Figure 2.5 displays the density in this 3D lattice in the xy-plane for the central lattice site of the z direction. Here we increased the fraction U/J by increasing the lattice depth s_ξ up to a point where we could only observe the Mott insulator plateaus anymore. When going from left to right one can spot the slow development of the MI rings stacking on top of each other and forming a so called wedding cake structure for the case of high U/J.

Due to the fact, that the trap in z direction is much tighter, we don't see a very clear distinction between SF regions and MI plateaus and skip a presentation of this direction.

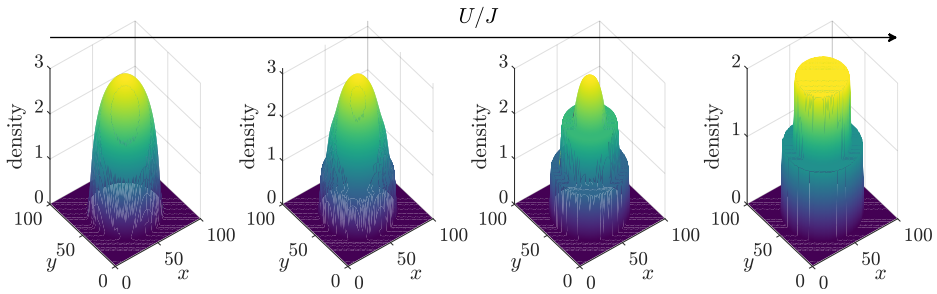

Figure 2.5: Density for a 3D lattice and increasing U/J from left to right. While the lattice depth is increased the density starts to form Mott insulator plateaus with superfluid regions in between. At the rightmost point, the so called wedding cake structure can be observed.

The other ground state calculation which was done features an increase of $\bar{n}$ while keeping U/J fixed and only shows the x direction of the ground state. While the density (blue) for low $\bar{n}$ is similar to a Thomas-Fermi profile, it starts to develop a flat top in the second tile of Fig. 2.6. The orange line shows the order parameter which is non zero for a superfluid and zero for a Mott insulator state. When going from left to right one can see that the order parameter partially goes to zero when a Mott plateau is forming.

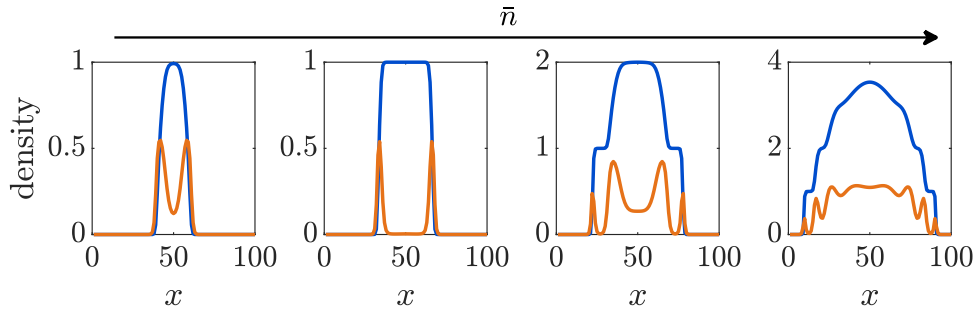

Figure 2.6: Density (blue) and superfluid order parameter (orange) at a fixed U/J vs. increasing $\bar{n}$. In the leftmost picture there is a superfluid present everywhere, but as soon as a Mott insulator plateau forms, the superfluid order parameter goes down to zero and one can clearly see the suppression of the superfluid component.

2.4 Gross-Pitaevskii equation with external periodic potential

Before we have mainly discussed the properties of a single particle in a periodic lattice and the description within the Schrödinger equation. Now we want to extend the SE by a density depending interaction term, the contact interaction energy $U_c(\mathbf{r}) = g|\Psi(\mathbf{r})|^2$, leading to a non-linear Schrödinger equation

$$-i\hbar\frac{\partial\Psi(\mathbf{r})}{\partial t} = \left[-\frac{\hbar^2}{2m}\nabla^2 + V(\mathbf{r}) + g|\Psi(\mathbf{r})|^2\right]\Psi(\mathbf{r}) \ , \tag{2.20}$$

which is called Gross-Pitaevskii equation (GPE) [57, 58]. Here, the kinetic and potential energy term stay unchanged, apart from the fact that they are written now in three dimensions. The wave function is normalized to the total atom number N as $\int \mathrm{d}\mathbf{r}|\Psi(\mathbf{r})|^2 = N$. The contact interaction parameter $g = \frac{4\pi\hbar^2 a_\mathrm{s}}{m}$ is determined by the s-wave scattering length and may be tuned via the magnetic field in experiments, see Sec. 1.3.5. Stationary solutions to the GPE can be written in the form $\Psi(\mathbf{r}, t) = \Psi(\mathbf{r})e^{-i\mu t/\hbar}$, which gives the stationary time-independent equation

$$\mu\Psi(\mathbf{r}) = \left[-\frac{\hbar^2}{2m}\nabla^2 + V(\mathbf{r}) + g|\Psi(\mathbf{r})|^2\right]\Psi(\mathbf{r}) \ . \tag{2.21}$$

Here μ denotes the chemical potential, which quantifies the energy it takes to add/ remove a particle to/from the system. For a positive chemical potential $\mu > 0$ the interactions are repulsive, whereas for $\mu < 0$ the interactions are attractive.

In the following we want to describe the approach to numerically evolve the GPE in time and also how to calculate ground states of the GPE in an external potential.

2.4.1 Numerical approach - Split step Fourier method

Due to the fact, that the GPE is a nonlinear partial differential equation, one usually has to obtain solutions via numerical calculations. The are actually quite a few algorithms to solve these type of equations. Here we want to focus onto the one used in the following simulations, the split-step Fourier method, or time-splitting spectral method, which is quite efficient and easy to understand.

Starting from the Hamiltonian of the system, we want to split it up into a kinetic and a potential part

$$\hat{H} = \hat{T} + \hat{V} = \frac{-\hbar^2}{2m}\nabla^2 + V(\mathbf{r}) \ . \tag{2.22}$$

Reminding us of the time-dependent GPE we can integrate from t to $t + \Delta t$, which leads to an equation for a small time step Δt

$$\Psi(\mathbf{r}, t + \Delta t) = e^{-i\hat{H}\Delta t/\hbar}\Psi(\mathbf{r}, t) \ , \tag{2.23}$$

if the Hamiltonian satisfies $\hat{H} \equiv \hat{H}(t)$. The kinetic and potential energy operators do not commute $[\hat{T}, \hat{V}] \neq 0$, which prohibits us to write the exponential as a product of an exponential of each individual term. However, it is still possible to approximate it as

$$e^{-i\hat{H}\Delta t/\hbar}\Psi(\mathbf{r}, t) \approx e^{-i\hat{V}\Delta t/2\hbar}e^{-i\hat{T}\Delta t/\hbar}e^{-i\hat{V}\Delta t/2\hbar}\Psi(\mathbf{r}, t) \ , \tag{2.24}$$

which only produces an error of $\mathcal{O}(\Delta t^3)$ [59, 60]. Now we have a look on the order in which we apply the operator exponentials to the wave function. First we do the operation $e^{-i\hat{V}\Delta t/2\hbar}\Psi(\mathbf{r}, t)$, which corresponds to the multiplication $e^{-iV(\mathbf{r})\Delta t/2\hbar}\Psi(\mathbf{r}, t)$ because the potential energy operator $\hat{V}$ is diagonal in position space. For the kinetic energy operator, it is quite similar. When performing a Fourier transform, the differential operator $\nabla \to \mathbf{k}$ goes over to a multiplication with the wave vector. This means that by taking the Fourier transform of the wave function $\tilde{\Psi}(\mathbf{k}, t) = \mathcal{F}[\Psi(\mathbf{r}, t)]$, the operation reduces to the multiplication $e^{-i\hbar k^2\Delta t/2m}\tilde{\Psi}(\mathbf{k}, t)$. So in total, the sequence of calculations becomes

$$\Psi(\mathbf{r}, t + \Delta t) = \hat{V}_{\Delta t/2}\, \mathcal{F}^{-1}[\hat{T}_{\Delta t}\, \mathcal{F}[\hat{V}_{\Delta t/2}\, \Psi(\mathbf{r}, t)]] \ , \tag{2.25}$$

where afterwards the wave function needs to be renormalized to satisfy $N = \int \mathrm{d}\mathbf{r}|\Psi(\mathbf{r}, t + \Delta t)|^2$ with the total atom number N.

2.4.2 Ground states in a 3D lattice - Comparison of methods

Putting the previously discussed method to the test, we show a series of ground states with increasing lattice depth. For that we choose the same lattice configuration and trapping frequencies as before in Section 2.3.1. We directly plot both the

GPE results and the GW results together for comparison in Figure 2.7.

We integrate both x- and y-axis out to get only the axis with the larger lattice spacing. The GPE results are unchanged, but the GW results on each lattice site were multiplied by the respective Wannier functions and added together to obtain a continuous curve. At $0\,\mathrm{E_{r,532}}$ both methods result in a smooth distribution, but only the GPE solution is correct. Increasing the lattice depth starts to form small lobes, which have a different conciseness. At around $1\,\mathrm{Er},532$ both concepts yield similar curves, which is expected, as this is the transition where now the GW ansatz becomes valid. In the rightmost plot the GPE solution already fills two more lattice sites compared to the GW solution.

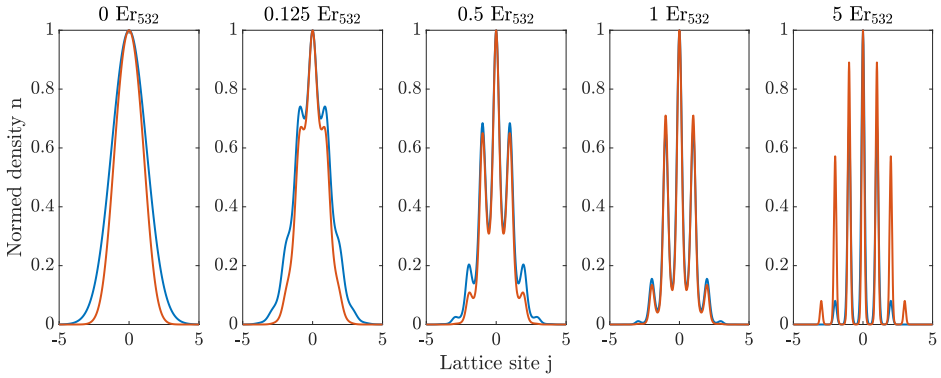

Figure 2.7: Integrated normalized densities in the z-direction for both GPE (orange) and GW (blue) 3D calculations. The lattice depth increases from left to right. At around $1\,\mathrm{E_{r,532}}$ both approaches yield very similar results.

Chapter 3

Bloch oscillations in quantum gases

Bloch oscillations were first mentioned by Felix Bloch in 1929 in the context of electrons in a solid [9]. Stating, that an electron will undergo an oscillatory motion and not accelerate for eternity, if a static external force is acting on the system, is a bit counter intuitive in a classical picture. In reality however, electrons will not undergo this oscillation due to scattering on defects in the crystal structure.

Later it was worked out, that cold atoms in an optical lattice will also undergo oscillations in position and momentum space [11, 12], when an external force is acting on them. Although s-wave scattering was limiting the observation of Bloch oscillation cycles in the beginning, it was later achieved to tune the interaction to almost zero by means of a Feshbach resonance, which allowed to observe more than 20000 cycles within a couple of seconds [13].

3.1 Bloch oscillation theory

As already discussed in Sec. 2, periodic lattices lead to a band structure in energy of the atom with eigenenergies $E_n(q)$ and eigenstates $|n, q\rangle$, labeled by the band index n and the quasimomentum $q = \hbar k$. When a particle in a periodic potential is subject to a static external force $F = ma$, the quasimomentum will change according to $\hbar\frac{\mathrm{d}k}{\mathrm{d}t} = F$, here $F = ma$ with the mass of the particle m and the acceleration a. When the particle is approaching the edge of the Brillouin zone, it can either tunnel via Laundau-Zener tunneling [10, 38] to the next higher band or stay in the current band and Bragg reflect to the other side of the BZ and repeat. The Bloch period is specified as the amount of time it takes a particle to go from one reflection to

another, i.e. it crossed $2\hbar k_\mathrm{L}$ in momentum, and is given by

$$t_\mathrm{B} = \frac{2\hbar k_\mathrm{L}}{F} \ . \tag{3.1}$$

Additionally to the momentum space oscillation there is a position space oscillation with an amplitude $L = \Delta_0(s)/F$ [61], which is quite small if gravity is used as acceleration. In a recent experiment they used a magnetic field gradient to apply a small force and reasonably high tunneling to also resolve the position oscillations [62].

To describe the system in a quantitative way, we start by writing down the Schrödinger equation

$$i\hbar\frac{\partial\psi(x,t)}{\partial t} = \left[-\frac{\hbar^2}{2m}\partial_x^2 + V_\mathrm{latt}(x) + Fx + U(x)\right]\psi(x,t) \tag{3.2}$$

in an external lattice potential $V_\mathrm{latt}(x)$ and with an external force F acting on it. We also add a general potential $U(x)$, which usually includes a harmonic confinement and interaction potentials, becoming important later on. In the tight binding model where the wavefunction usually takes the form $\psi(x,t) = \sum_j w(x-x_j)\sqrt{\chi_j}e^{-i\phi_j(t)}$ when localized Wannier functions $w(x)$ are assumed on each lattice site. Here χ_j are the amplitudes on site j and $\phi_j(t)$ are the corresponding phases. The potential $U(x)$ serves just as a placeholder, which will become clearer in the following chapters. Plugging this wave function into Eq. (3.2) we can arrive at an equation for the time evolution of the phases by integrating in time, which yields

$$\phi_j(t) = (-jdF + E_j)\frac{t}{\hbar} \ . \tag{3.3}$$

Following Ref. [63] we can write the time evolution of the wave function in momentum space as

$$\psi(k,t) = \psi_0(k)\sum_j \sqrt{\chi_j}e^{-i(jdk+\phi_j(t))} \tag{3.4}$$

In this picture we can understand now, that the different energy contributions of the lattice sites j are the effect leading to the different de- and rephasings. More on that in Sec. 3.4.4.

3.2 Theoretical framework - dipolar interactions and quantum fluctuations

The dipolar nature of Erbium atoms obliges us to also account for the dipolar interactions in our model. Previously, in Section 2.4, we have only considered the more basic contact interaction in the GPE. As discussed in Sec. 1.3.4, dipolar atoms feature a long range anisotropic interaction, which is fundamentally different from the contact interaction and also much more difficult to compute, because the potential has nonlocal, long-range character.

In the following, as the simulations are done over a range of different a_s, the condensate will enter the dipolar dominated regime, $\varepsilon > 1$ (see Sec. 1.3.4). As mentioned before, the contact and dipolar interaction will compete for specific geometries. At a certain point, these interaction terms will be close to cancelling each other out and another term beyond the mean field approximation, the so called quantum fluctuations or Lee-Huang-Yang (LHY) term, will become important. It is coming from the LHY correction [17] and will play a substantial role, stopping the condensate from collapsing. This correction gives an energy shift to the ground state of the form [64]

$$\Delta E(\mathbf{r}) = \frac{64}{15} g n^2(\mathbf{r}) Q_5(\varepsilon_{\mathrm{dd}}) \sqrt{\frac{n(\mathbf{r}) a_s}{\pi}}\,, \tag{3.5}$$

which also has a dependence on the density $n(\mathbf{r})$ and the dipolar strength $\varepsilon_{\mathrm{dd}}$ through $Q_l(x) = \int_0^1 \mathrm{d}u (1 - x + 3xu^2)^{l/2}$. In the following to obtain this correction term in the eGPE one has to differentiate the energy correction with respect to the density. One arrives at

$$U_{\mathrm{qf}}(\mathbf{r}) = \frac{32}{3} g \sqrt{\frac{a_s^3}{\pi}} \left(1 + \frac{3}{2}\varepsilon_{\mathrm{dd}}^2\right) |n(\mathbf{r})|^{3/2} = \gamma_{\mathrm{qf}} |n(\mathbf{r})|^{3/2} \tag{3.6}$$

by also using a common approximation of $Q_5(\varepsilon_{\mathrm{dd}}) \approx 1 + \frac{3}{2}\varepsilon_{\mathrm{dd}}^2$ [65, 66]. Now with all the additional interaction and correction terms needed for our system we can start to derive a model.

3.3 Derivation of the theoretical model

At some point we started to measure Bloch oscillations in the ERBIUM lab and wanted to compare our experimentally observed oscillations to simulated data, because sometimes it can get hard to understand experimental results without a respective theory. For that we decided to derive a discrete quasi-1D model, which should capture the physics of the experiment well enough and give comparable results.

We start from the full time-dependent 3D extended Gross-Pitaevskii equation in an external potential $V(\mathbf{r}) = V_{x,y}(x,y) + V_z(z) = \frac{1}{2}m\sum_{\xi=x,y,z}\omega_\xi^2\xi^2 + sE_\mathrm{r}\sin^2(k_z z)$, including a 3D harmonic and a 1D periodic confinement. The full form of the eGPE is given by

$$i\hbar\frac{\partial\Psi(\mathbf{r},t)}{\partial t} = \left[-\frac{\hbar^2\nabla^2}{2m} + V(\mathbf{r}) + U_c(\mathbf{r},t) + U_\mathrm{dd}(\mathbf{r},t) + U_\mathrm{qf}(\mathbf{r},t)\right]\Psi(\mathbf{r},t) \tag{3.7}$$

with the terms on the right side being the kinetic and potential energy, followed by the contact interaction energy $U_\mathrm{c} = g|\Psi(\mathbf{r},t)|^2$, the dipolar interaction energy $U_\mathrm{dd} = \int \mathrm{d}\mathbf{r}'\, U(\mathbf{r},\mathbf{r}')|\Psi(\mathbf{r}',t)|^2$ and the quantum fluctuations energy $U_\mathrm{qf} = \gamma_\mathrm{qf}|\Psi(\mathbf{r},t)|^3$.

In the following process of reducing the dimensions, we omit the dipolar interaction term, as there is no known analytic form regarding these kind of approximations, but it will be added again in the discrete one dimensional equation in the end.

Previously, a Gaussian ansatz following from the single-mode approximation (SMA) has proven sufficient for freezing out the transverse directions of the wavefunction, as in Ref. [67], which are not really from interest here. Due to the fact that we work with dipolar atoms, the atoms experience magnetostriction when confined in a trap. Therefore, we use a variational ansatz following Ref. [68], which allows for change in size $l = \sqrt{l_x l_y}$ and anisotropy $\eta = l_y/l_x$ in the transverse wavefunction, written as

$$\Psi(\mathbf{r},t) = \psi(z,t)\cdot\phi(x,y) = \psi(z,t)\cdot\frac{1}{\sqrt{\pi}l}\mathrm{e}^{-(x^2\eta+y^2/\eta)/(2l^2)}\ . \tag{3.8}$$

The wave function is normalized as $\int \mathrm{d}\mathbf{r}\,|\Psi(\mathbf{r},t)|^2 = N$, with N being the total number of atoms of the condensate. As a first step, we integrate out the transverse directions of the eGPE. This is done by inserting the ansatz above into Eq. (3.7),

multiply it with the radial wave function $\phi(x,y)$ and integrate out the x and y degrees of freedom

$$i\hbar \underbrace{\int \mathrm{d}x\mathrm{d}y\, \phi^2}_{=1} \frac{\partial \psi(z,t)}{\partial t} = -\frac{\hbar^2}{2m}\left[\int \phi\left(\partial_x^2+\partial_y^2\right)\phi\,\psi(z,t) + \int \phi^2 \frac{\partial^2\psi(z,t)}{\partial z^2}\right] + \int \phi^2 V_{x,y}(x,y)\psi(z,t) + \int \phi^2 V_z(z)\psi(z,t) + \int \phi^4 g|\psi(z,t)|^2\psi(z,t) + \int \phi^5 \gamma_{\mathrm{qf}}|\psi(z,t)|^3\psi(z,t)\ , \quad (3.9)$$

which reduces to a one dimensional equation which also depends on the variational parameters

$$i\hbar\frac{\partial\psi(z,t)}{\partial t} = \left[-\frac{\hbar^2}{2m}\partial_z^2 + V_z(z) + \frac{\hbar^2}{2ml^2}\left(\eta+\frac{1}{\eta}\right) + \frac{ml^2}{4}\left(\frac{\omega_x^2}{\eta}+\eta\omega_y^2\right) + \frac{g}{2\pi l^2}|\psi(z,t)|^2 + \frac{2\gamma_{\mathrm{qf}}}{5\pi^{\frac{3}{2}}l^3}|\psi(z,t)|^3\right]\psi(z,t)\ . \quad (3.10)$$

As described in Sec. 2.2, Wannier functions are a practical tool to work with localized states on each lattice site instead of delocalized Bloch functions. Within this section of the thesis though, it is even more convenient to approximate the ground state of the Wannier function as the harmonic oscillator ground state

$$w_n(z-z_j) \approx \frac{1}{\sqrt{\sqrt{\pi}l_{\mathrm{latt}}}}\mathrm{e}^{-\frac{(z-z_j)^2}{2l_{\mathrm{latt}}^2}}\ . \quad (3.11)$$

Here $l_{\mathrm{latt}} = \sqrt{\frac{\hbar}{m\omega_{\mathrm{latt}}}}$ denotes the oscillator length within the harmonic approximation of the lattice with a harmonic frequency $\omega_{\mathrm{latt}} = 2\sqrt{s}\frac{E_{\mathrm{r}}}{\hbar}$. The ground state approximation is valid for deep lattices with strong localization ($V_0 \gg E_{\mathrm{r}}$). In our case, a lattice depth of $V_0 = 8\,E_{\mathrm{r}}$ is on the verge of this approximation, but it allows us to condense the one dimensional Eq. (3.10) even further down to a one dimensional discrete model to simplify the numerical calculations afterwards.

Finally with the last simplification $\psi(z,t) = \sum_j \psi_j(t)w(z-z_j)$ and integrating

out the lattice direction z, we arrive to the discrete one dimensional eGPE

$$i\hbar\frac{\partial\psi_j}{\partial t} = -J(\psi_{j+1}+\psi_{j-1}) + \Bigg[\underbrace{\frac{g}{(2\pi)^{3/2}l^2 l_{\text{latt}}}}_{=:g^{1\text{D}}} n_j + U^{\text{dd}}_{j,j}n_j + \sum_{k\neq 0} U^{\text{dd}}_{j,j+k}n_j n_{j+k} + \underbrace{\left(\frac{2}{5\pi^{3/2}l^2 l_{\text{latt}}}\right)^{\frac{3}{2}}\gamma_{\text{qf}}}_{=:\gamma^{1\text{D}}_{\text{qf}}} n_j^{\frac{3}{2}}\Bigg]\psi_j\,. \quad (3.12)$$

Here the dipolar onsite and offsite term, $U^{\text{dd}}_{j,j}$ and $U^{\text{dd}}_{j,j+k}$ respectively, were added and two transverse and longitudinal correction terms were omitted because they do not play any role in the dynamics. The parameter J is the tunneling parameter and is obtained by calculating the energy width of the lowest Bloch band for a lattice depth of V_0, see Sec. 2.2. In the case of simulating the Bloch oscillations, one needs to add the external force term $jdF_{\text{ext}}\psi_j$ to the right side of Eq. (3.12). Here $F_{\text{ext}} = mg\cos\theta$ with $m = m(^{166}\text{Er})$ the mass of erbium, $g = 9.8055\,\text{m/s}^2$ the gravitational acceleration in Innsbruck [69] and $\theta = 11^\circ$ the angle of the lattice w.r.t. the gravity axis.

Advancing further on the list of things needed to calculate the variational ground states we need to define the energy which we have to minimize during the imaginary time evolution ($\tau = it$). It can be obtained by integrating the right side of Eq. (3.12) with respect to the density n and adding the two transverse correction terms again, which sums up to

$$E[l,\eta,\psi] = \frac{\hbar^2}{2ml^2}\left(\eta+\frac{1}{\eta}\right) + \frac{ml^2}{4}\left(\frac{\omega_x^2}{\eta}+\eta\omega_y^2\right) + \sum_j\Bigg\{-J(\psi_{j+1}+\psi_{j-1})n_j + \frac{1}{2}g^{1\text{D}}n_j^2 + \frac{1}{2}U^{\text{dd}}_{j,j}n_j^2 + \frac{1}{2}\sum_{k\neq 0}U^{\text{dd}}_{j,j+k}n_{j+k}n_j + \frac{2}{5}\gamma^{1\text{D}}_{\text{qf}}n_j^{\frac{5}{2}}\Bigg\}. \quad (3.13)$$

With this settled we have achieved the important formulas and the basic concept to start the simulations. The final equations were used to simulate the theoretical data in [20], and the code can be found in Appendix A.

3.4 Simulation of the experimental system

To start off the simulations, we first have to define a couple of relevant system parameters of the experiment. At the beginning, a BEC of ^{166}Er is produced in an ODT with trap frequencies $(\omega_x, \omega_y, \omega_z) = 2\pi \cdot (217, 34, 240)\,\mathrm{Hz}$ at a scattering length of $80\,\mathrm{a_0}$. Then the scattering length is ramped to the final value just before the lattice is switched on and the ODT off. At this point, gravity acts on the atomic cloud and Bloch oscillations occur.

3.4.1 Ground states and their size

For the simulations, we simplify the ground state search in such a way that we already calculate the ground state at the final scattering length in the lattice, such that we can use our previously derived model from Eq. (3.12). We calculate the ground state employing said equation in imaginary time ($\tau = it$) for finite time steps until a threshold is reached, depending on the relative change of the wave functions. The imaginary time evolution (ITE) is carried out with the help of the ode45 [1] algorithm implemented in MATLAB. At first, a trial wavefunction, a simple discrete Gaussian, is used for the lattice direction. For the transverse direction we use l and η calculated from the trap frequencies ω_x and ω_y. But before the ode45 function is employed, the energy functional $E[\psi, l, \eta]$ w.r.t. Eq. (3.13) is minimized and the variational parameters are adjusted. Then the ode45 function is employed, and the process is repeated until said threshold is reached.

In Fig. 3.1 the contour of the density profile of two simulations is shown. Panel (a) shows the transverse density profile for a ground state calculated with a scattering length of $a_\mathrm{s} = 55\,\mathrm{a_0}$, whereas (b) shows the density profile of a ground state at $90\,\mathrm{a_0}$. One can clearly see the difference in size due to the different parameters l & η. For the two ground states we get $(l, \eta) = (3.01\,\mu\mathrm{m}, 4.01)$ and $(l, \eta) = (3.31\,\mu\mathrm{m}, 5.95)$ for panels (a) and (b), respectively. From these values we can calculate the widths in x and y as $l_x = l/\sqrt{\eta} = 1.36\,\mu\mathrm{m}$ and $l_y = l\sqrt{\eta} = 8.07\,\mu\mathrm{m}$ for the latter case. In (c) and (d) we show the x-z density distribution for the respective scattering lengths 55 and $90\,\mathrm{a_0}$. For a higher scattering length clearly more lattice sites are significantly occupied and will therefore contribute to Bloch oscillations. Due to

[1] The ode45 function is relying on an explicit Runge-Kutta (4,5) numerical algorithm with the Dormand-Prince pair for solving differential equations, see Ref. [70].

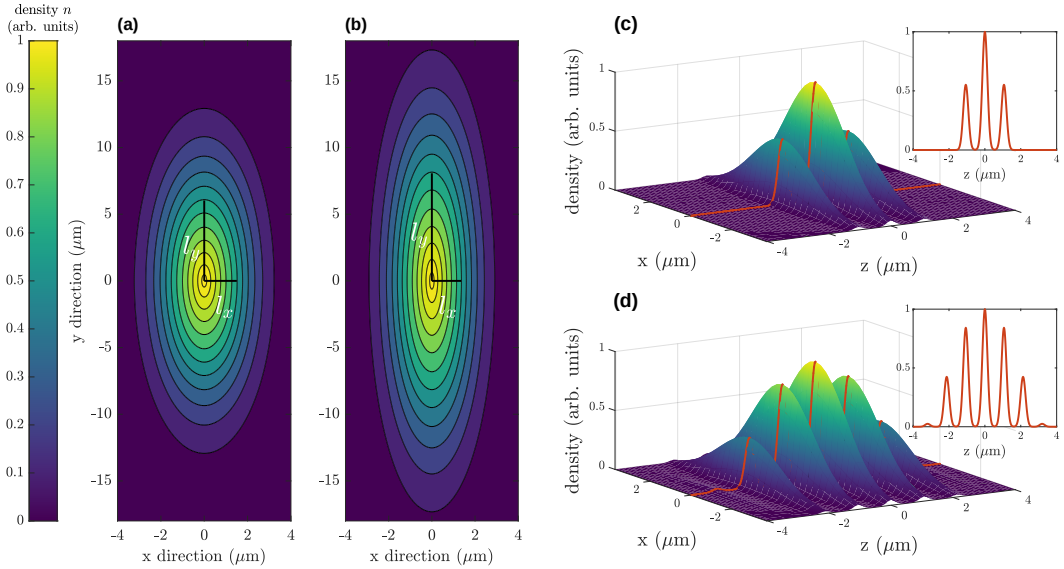

Figure 3.1: (a) Contour plot of the density n along the transverse directions x, y at a scattering length of $a_s = 55\,a_0$. (b) Same plot at a different $a_s = 90\,a_0$ to show the scattering length dependence of l and η (l_x, l_y). One can clearly see the difference in size along the y direction, as it stretches much further for higher a_s. (c) x-z density profile at $55\,a_0$ showing three occupied lattice sites. The inset shows a cut through the profile at $x = 0$. (d) Density profile for a higher scattering length at $90\,a_0$ which shows 7 significantly populated lattice sites.

the large relative change in the number of lattice sites occupied, we decided to go for a relatively large a_s range.

We ran the ground state simulation for a a_s range from $50\,a_0$ to $100\,a_0$ and an atom number N ranging from $5e3$ to $5.5e4$. For each of the individual discrete ground states, we extract some characteristic width to put the change of the size in perspective. We fit the g.s. with a Gaussian function of the form $G(z) = A\,e^{-z^2/(2\sigma^2)}$ and calculate the full width at half maximum FWHM $= 2\sqrt{2\ln 2}\sigma$. The results of our findings are shown Fig. 3.2, where we plot the FWHM vs. the scattering length for various atom numbers in panel (a). Panels (b-d) show a specific ground state corresponding to its color coded circle in the title. From right to left we go to lower scattering length, which means the dipolar strength ε_{dd} increases and the dipolar interaction is dominating on the left (below $65.5\,a_0$). This also means that the quantum fluctuations term gets more and more important as the density increases.

Another point to mention is, that the transition to a FWHM < 1.15 happens at lower scattering length the more atom number is used in the simulation. This

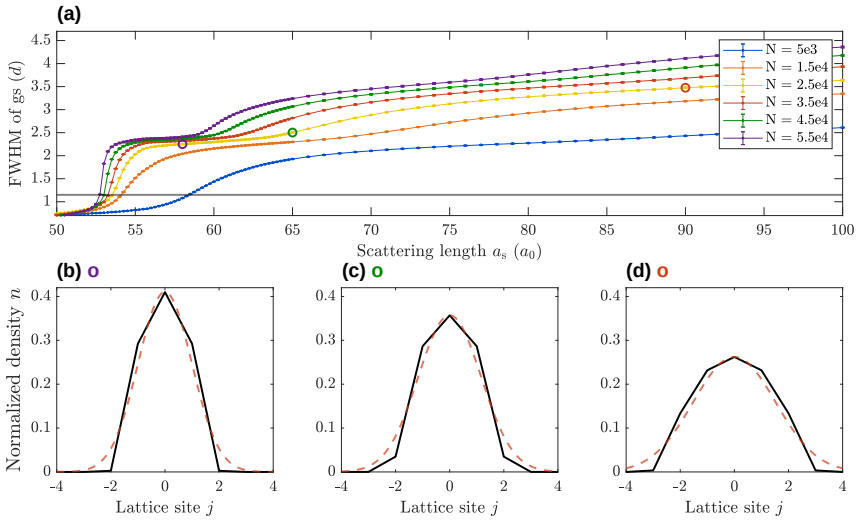

Figure 3.2: (a) FWHM of the discrete 1D ground states calculated by the imaginary time evolution in the external potential. The FWHM is extracted from a Gaussian fit to the ground state. The gray line indicates a threshold of FWHM = 1.15, where everything below has at least 80 % of the total atom number in the central lattice site ($j = 0$). (b-d) Central lattices sites of three different ground states at $N = 2.5e4$ and a scattering length of $a_s = [58, 65, 90]\, a_0$ from left to right.

is easily understood, as the density is even higher in absolute values and therefore the quantum fluctuations term can hold against the collapse to one lattice site even longer. Though one has to admit, that the model is not able to realistically assess the collapse of the real wave function, as the collapse to one lattice site affects the values of l and η vastly. The threshold of the FWHM at 1.15 was chosen as such, that the population in the central lattice site is at least 80 % and only maximally 10 % of the total number of atoms populate the neighboring lattice sites.

3.4.2 Bloch oscillation in momentum space

After the ITE follows the abrupt switch off of the harmonic trap described by the frequencies $\omega_{x,y,z}$. Only the ones of the lattice beam remain, which are estimated to be $(\omega_x^l, \omega_y^l, \omega_z^l) = 2\pi \cdot (4, 4, 0.5)$ Hz. Then the ground states are evolved in real time (RTE) to simulate the Bloch oscillations due to the external force. To observe the momentum evolution, we look at the Fourier transformed wave function in k-space after $t_{\text{exp}} = 30$ ms of expansion. In the simulation, this can be calculated by the convolution of the momentum density distribution $\tilde{n}(q,t) = |\tilde{\psi}(q,t)|^2 = |\mathcal{F}(\psi_j(t))|^2$

with a Gaussian of the width $\sigma_{\text{exp}} = \frac{\hbar k_z}{m} t_{\text{exp}}$. This yields

$$\tilde{n}_{\text{exp}}(q,t) = \tilde{\psi}_{\text{exp}}(q) * |\tilde{\psi}(q,t)|^2 \quad \text{with} \quad \tilde{\psi}_{\text{exp}}(q) = \frac{1}{\sqrt{\aleph}} e^{\frac{-q^2}{2(l_z/\sigma_{\text{exp}})^2}} \ , \tag{3.14}$$

where $\aleph$ is a normalization factor. Figure 3.3 shows the evolution of $\tilde{n}_{\text{exp}}(q,t)$ for a slow and fast dephasing case. The dephasing can be made out by looking at the width of the distribution, i.e. the width of the yellow line. In the upper tile at $60\,a_0$, there is merely a change in the width and the amplitude doesn't change drastically as well. In the other tile at $90\,a_0$ though, the strong oscillation is already gone after two Bloch cycles.

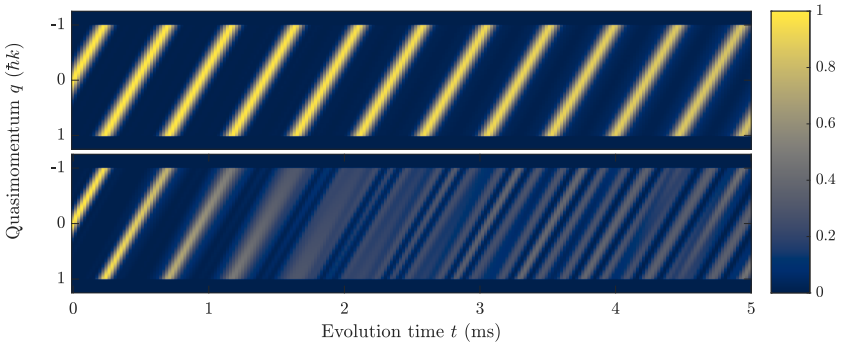

Figure 3.3: Quasi-momentum evolution of the Bloch oscillation for two different scattering lengths. In the upper panel a slowly dephasing case at $60\,a_0$, where the width of the momentum distribution stays roughly the same, whereas in the lower panel in the fast dephasing case at $80\,a_0$ the width is much larger after a couple of milliseconds. The color scale shows the relative intensity.

To quantify the Bloch oscillation in terms of dephasing of the initial state, we take a look at the full width of the momentum distribution $\Delta q = 2\sqrt{\text{var}(\tilde{n}_{\text{exp}}(q,t))}$. In the following we use this width to determine a quantity called the dephasing rate γ and also a dephasing time τ for completeness.

3.4.3 Dephasing rate of the Bloch oscillations

After calculating all the momentum widths of the momentum distributions we noticed, that the momentum width Δq at integer multiples of the Bloch period takes roughly a linear form. For the same two cases as in Fig. 3.3, 60 and $80\,a_0$, we show

the full procedure in Fig. 3.4. For a fast dephasing Bloch oscillation we can use all the points below a certain threshold, which was determined by looking at the momentum width of a dephased momentum distribution. For the slow dephasing cases we usually restricted ourselves to the first few ms because the curve typically bends upwards afterwards. We now fit the diamonds with a linear function and extract the dephasing rate γ from the slope.

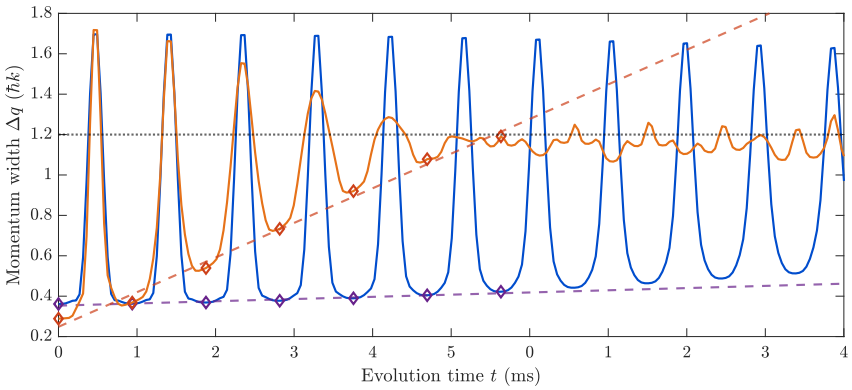

Figure 3.4: Evolution of the momentum width Δq for a fast dephasing BO (orange line) and a slow dephasing BO (blue line). The diamonds show the momentum width after the first few Bloch oscillation cycles. The dashed lines are linear fits to the diamonds of the respective color, where the slope corresponds to the dephasing rate γ. The dephasing time τ is evaluated as the time where the linear fit crosses the gray dotted line, a threshold for the momentum width.

The calculations are done for quite a big range in a_s and atom number. We only plot a couple of them in Figure 3.5 to keep it clear. What we see directly from the plot is the non-trivial dependence of γ on the atom number N. For high a_s the dephasing is anyway dominated by the contact energy on the different lattice sites and is therefore quite similar. For lower a_s though we observe dephasing minima γ_{min} at different scattering lengths for various atom numbers.

Going from low N to high N changes the shape of the minimum quite drastically. While being more or less symmetric for $N = 5e3$, the shape gets more and more asymmetric and even develops a kind of plateau on the lower side of the minimum for high atom numbers like $N = 5.5e4$. At high scattering lengths, the curves of different atom numbers seem to approach similar dephasing rates γ.

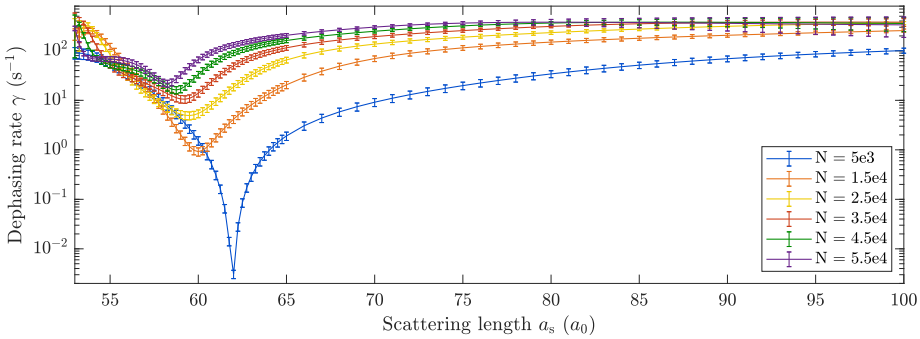

Figure 3.5: Dephasing rate γ of the Bloch oscillations for different atom numbers N across a broad range of scattering length a_s. The rate γ is obtained as the slope of the linear fit to the first points in Fig. 3.4. The shape of the curves look asymmetric due to the change of the ground state when going to lower scattering length. Also the minimum of the dephasing rate shifts to lower a_s for a higher atom number N.

3.4.4 Further analysis of features

In the following, we want to further analyze the minima of the dephasing rate and how it behaves for different atom numbers. For that, we first examine the energy per particle from Eq. 3.13 without the transverse correction terms. We plot every energy contribution from the contact to the quantum fluctuation energy for $2.5e4$ atoms in different colors in Fig. 3.6(a).

The biggest contributions are the contact interaction (blue) and the dipole-dipole onsite interaction (orange), which contribute against each other. The dipole-dipole offsite (yellow) and quantum fluctuation energy (red) add a repulsive part and the latter helps to stabilize the BEC at low scattering length, as you can see by the total energy per particle (gray). This fits our understanding of how these different terms act on the condensate.

Now we can try to look at the chemical potential $\mu_i = \dfrac{\partial E_i}{\partial n}$, which may help us to understand the position of the minima in Fig. 3.5 [16, 20]. We calculate it from

$$\mu_{i,\mathrm{tot}} = |\chi_i|^{-2} \left(2E_{i,\mathrm{mf}} + \frac{5}{2} E_{i,\mathrm{qf}} \right) \tag{3.15}$$

which is then plotted in Fig. 3.6(b-d) for each lattice site at different scattering lengths at the respective colored lines in (a). The gray part shows the total chemical potential $\mu_{i,\mathrm{tot}}$, whereas the red part shows only the quantum fluctuation addition. We see that for higher scattering lengths the QF part is relatively low, but lowering

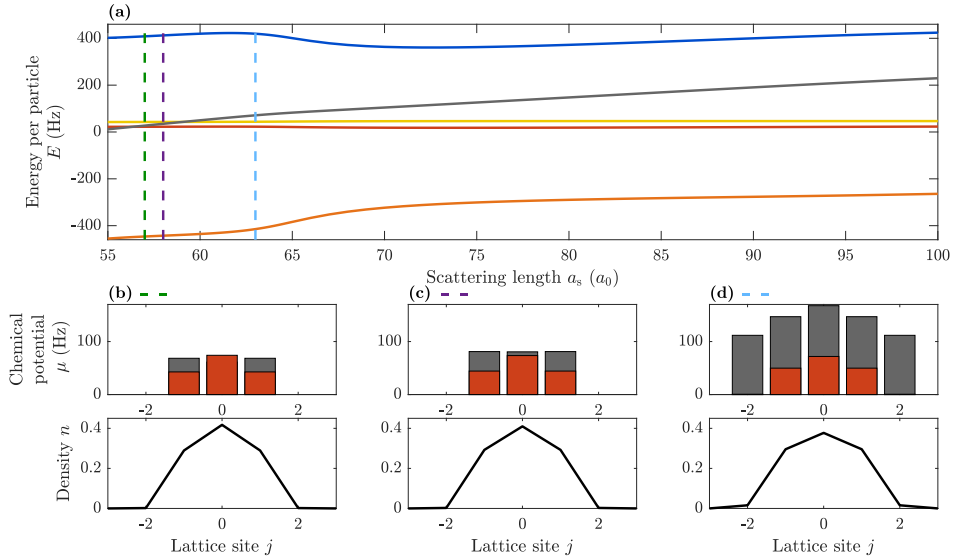

Figure 3.6: (a) Energy per particle in the system of 2.5e4 atoms split up in the contributions of contact (blue), DD onsite (orange), DD offsite (yellow) and QF (red) energy. The gray line shows the total energy per particle, which approaches zero for lower scattering length. (b-d) Show both the chemical potential μ and the density n of the ground state at the respective positions in (a). The chemical potentials show μ_{tot} in gray and the contribution of the beyond-mean-field term μ_{bmf} in red.

a_s gives it a significant value in the total chemical potential. What we also observe is a flattening of the distribution at some point on the scattering length spectrum.

To compare the minima in Fig. 3.5 and the oblateness of the chemical potential, we extract the minimum of the dephasing rate γ_{min} for each of the individual atom numbers. We also write down the scattering length at which the minimum is reached and plot this together in Fig. 3.7. The oblateness is expressed through the variance of the chemical potential, and we take the minimum and plot it in green. For low atom number we observe a quite good agreement of the two methods. However, for higher N, we observe a significant discrepancy between these two. One of the reasons for this could be that the method of determining the dephasing rate is not appropriate for higher dephasing rates γ. Another reason could be that the calculations are simply getting worse due to yet unidentified problems.

Another feature of Bloch oscillations is the (possible) revival of oscillations after the initial decay [71]. Since we have a system without decoherence, nothing but the interactions itself can change the momentum width Δp. Therefore, we can observe

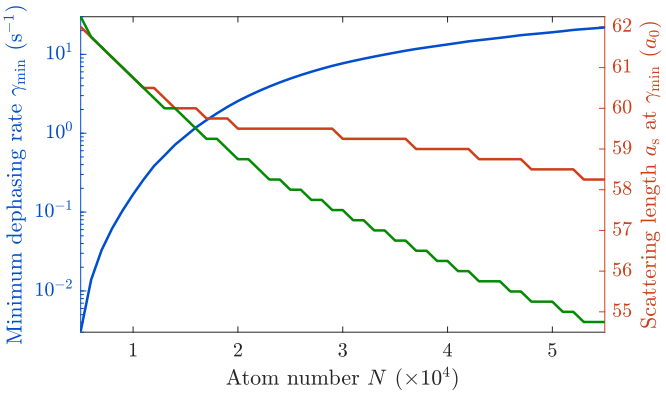

Figure 3.7: Minimum of the dephasing rate $\gamma_{\min}$ versus the atom number in blue determined by taking the lowest point of the curves in Fig. 3.5. On the right axis the scattering length at which this minimum of dephasing appears vs. N is plotted in orange. Additionally, the scattering length, at which the variance of the chemical potential is minimal is also shown in comparison (green).

these revivals of some BOs within a reasonable time frame. In the case of Fig. 3.8, the Bloch oscillations revive after around $t_{\text{re}} = n \cdot 13\,\text{s}$, $n \in \mathbb{N}^*$, which is shown by the momentum p going back to saturated yellow and the momentum width Δp reaching its extrema.

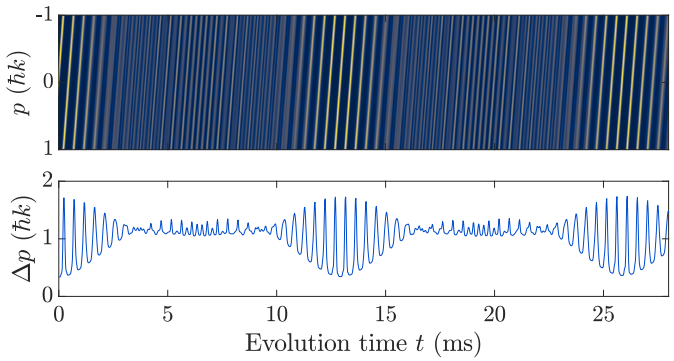

Figure 3.8: Evolution of the momentum p and momentum width Δp during a generic Bloch oscillation, which rephases after the initial dephasing caused by the interactions. After around $t_{\text{re}} = [13, 26]\,\text{ms}$ the momentum width is back to its original value at zero time.

3.5 Further possible extensions to the model

The assumption that the condensate width in the transverse directions at each lattice site is the same is simply a necessary step to obtain a not too complicated analytic expression of the different terms in the GPE. To further improve the model one would need to employ a different transverse wave function with variable width $l(z)\,\&\,\eta(z)$, similar to [72, 73]. This would finally make the wavefunction non-separable between the three dimensions, ergo $\Psi(\mathbf{r},t) \neq \psi(z,t)\cdot\phi(x,y)$.

Another point where things were simplified is the RTE. Here, $l\,\&\,\eta$ should actually be allowed to change during the time evolution, hence $l(t)$ and $\eta(t)$. So to implement that, one would need to minimize the energy in Equation (3.13) again during each step of the real-time evolution, which would drastically increase the time needed for each simulation run.

In addition to that above, another viable extension would be to do the RTE in the 3D GPE and extract l and eta from there, create some course grid where one can interpolate for $a_s/N/t$ to eventually do more points in the discrete 1D model, to obtain the results faster.

As already mentioned, the discrete quasi-1D model is not really able to catch the physics when going to one lattice site. Therefore, it would be very nice if one could either do some simulations in the full 3D GPE or go to a continuous quasi-1D GPE to allow for change of the wave function in the lattice direction. Of course, doing the whole simulations in the full 3D GPE would be ideal but would massively increase computation complexity and time.

Chapter 4

Laser system for manipulation of erbium atoms

In the following chapter we will focus on the build up/rebuild of a setup for an external cavity diode laser (ECDL), which may be used in the ERBIUM experiment in the future. First, we will go through the basics of the diode laser and the external cavity to realize a 631 nm light source. Then we will discuss the current optical setup and the lock to a stable reference cavity to achieve long-term stability. In the last part, we will talk about complications which came up along the path.

4.1 Laser (diode) working principle

To understand the laser setup to full extent we start by describing the underlying physics of lasers before we continue with the setup.

4.1.1 Stimulated emission of light

Stimulated emission of light is a fundamental process in the field of quantum physics and plays a central role in the operation of lasers. In this process, an excited atom or molecule, previously raised to a higher energy state, is triggered to emit a photon of light when it encounters another photon with the same energy and direction. This phenomenon results in coherent amplification of light, where the emitted photons are in phase and have the same wavelength and direction as the stimulating photon; see Fig. 4.1. Stimulated emission is the key principle of laser technology, enabling

the generation of intense, monochromatic, and highly directional beams of light with a wide range of applications in fields such as communications, medicine, and materials processing [74].

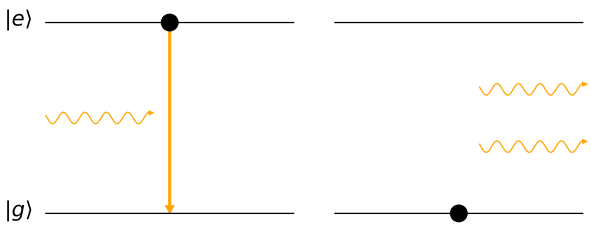

Figure 4.1: Sketch of the principle of stimulated emission of light. An incoming photon triggers the decay of an electron from an excited state to the ground state which emits a photon with the same wave vector as the incoming wave.

4.1.2 Laser diode chip

Today, the principle of stimulated emission of light is often implemented through a semiconductor chip, which is possible in a wide range of wavelengths, from UV to NIR. A laser diode usually consists of three main layers (see Fig. 4.2):

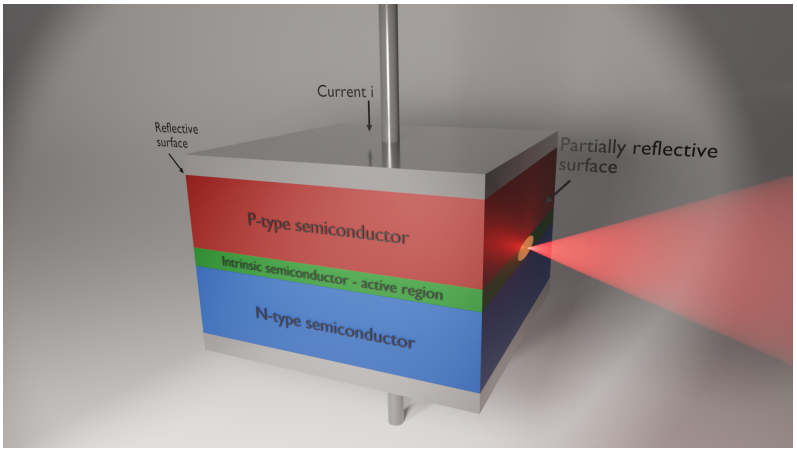

Figure 4.2: Drawing of a photo diode chip which consists of a P- and N-type semiconductor with an intrinsic semiconductor placed inbetween. When current is flowing, the middle part becomes active and generates photons, which get reflected on the back side and can leave through the front partial reflector.

An active layer, a p-type semiconductor, and an n-type semiconductor. When a forward voltage and current i is applied across the p-n junction, it allows the flow of electrons from the n-side to the p-side and the flow of holes vice versa. This injection of charge carriers into the active region creates a population inversion, i.e. more electrons in higher energy states than in lower states, which is essential for laser operation. When a photon travels through the active layer, it can stimulate an electron to drop to a lower energy state and emit a photon. This results in a chain reaction that creates an avalanche of photons.

To maintain enough photons inside the layer the end facets are reflective and partially reflective, respectively. The emitted photons bounce back and forth between these surfaces, stimulating further photon emissions until they finally leave through the partially reflective surface. The emitted photons are coherent photons with the same wavelength. Adjusting the current mostly increases the photon flux, but may also induce mode hopping. Lasers are extremely sensitive devices, reacting to small changes in the temperature or current by hopping between the longitudinal modes.

4.2 ECDL for the generation of 631 nm light

The generation of 631 nm light is realized with an external cavity diode laser (ECDL), which utilizes an external cavity to select the proper wavelength and give feedback to the laser diode, and therefore stabilize it during operation. ECDLs usually contain a laser diode chip built into a larger resonator with separate connections, which are often mounted together with an aspheric collimation lens. The whole laser package is then mounted with a grating which allows for a fine tuning of the desired wavelength.

The most simplistic setup only uses a grating in the Littrow configuration, which reflects the 0^{th} order away from the laser and the 1^{st} order back into the laser. This setup is a bit cumbersome as the output beam is changing direction when rotating the grating. Another configuration is the Littman-Metcalf configuration [75, 76], which uses an additional rotating mirror to select the wavelength. The drawback of this setup is that the strongest (0^{th}) order gets reflected onto the mirror and is therefore lost. Thus, we use another more advanced Littrow configuration.

4.2.1 ECDL - Littrow enhanced configuration

The laser is built upon a design featured in [77], based on the enhanced Littrow configuration [78]. This enhanced configuration features the grating and a mirror mounted on one piece that can be rotated; see Fig. 4.3. Here, the output beam remains fixed, and one can choose the wavelength by turning the whole flexure. Another feature of this configuration is the parallelism of the input and output beams, which simplifies the entire setup.

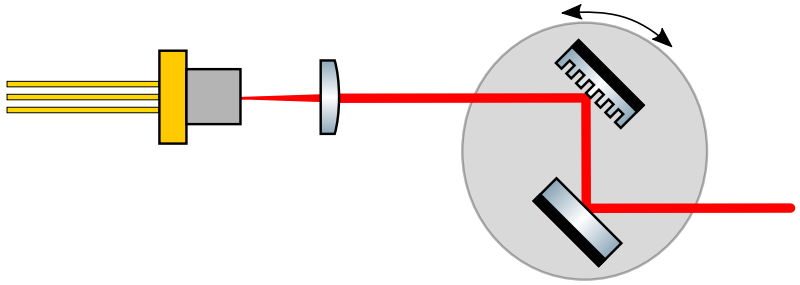

Figure 4.3: Enhanced Littrow configuration where the output laser beam stays fixed. The grating and the mirror are mounted on a flexure, which can be turned by two micrometer set screws.

4.2.2 Current power characteristics

The first thing on a long list is to determine the current power characteristics for different diode temperatures to get a feeling for the threshold currents I_{th} and power outputs P. Therefore, we put a power meter in front of the laser output and start to slowly increase the applied current. At this point, there is no beam shaping optics set up. [1] As we can see in Fig. 4.4 the laser diode HL63163DG [2] outputs around 60 mW of power at the maximum current that we can set. This seems to roughly correspond to the values written in the datasheet.

Further, we fit each of the I-P curves with a slope and extract the threshold current I_{th} at the intersection with the x axis. In addition, we can calculate the slope efficiency for all the temperature points that we have and plot them in Figure 4.5. Both plots look very similar to those in the datasheet, although they are a bit off. But since every laser diode can be different, it seems fine.

[1] In fact the setup was already built up but too unstable, which was the reason to rebuild it.
[2] The laser diode HL63163DG datasheet can be found under https://www.thorlabs.com/

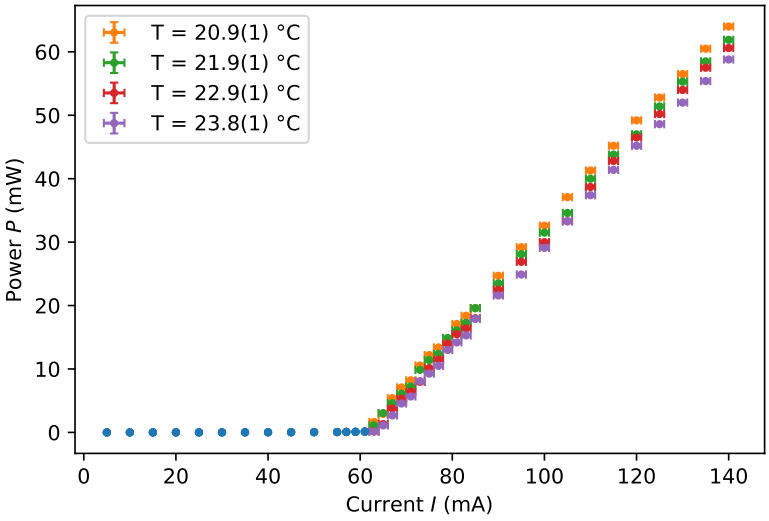

Figure 4.4: Current power characteristics of the laser diode HL63163DG for different typical temperatures used. Below a current of 60 mA no lasing is observed. Above this threshold we observe lasing with different efficiencies and threshold currents.

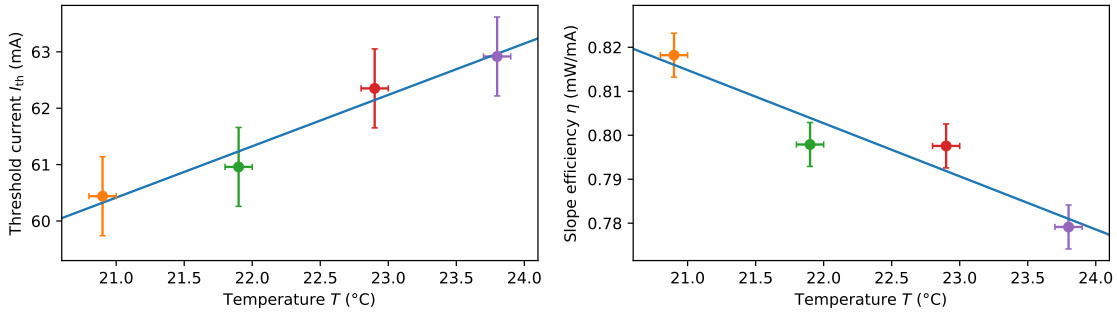

Figure 4.5: Threshold current I_{th} and slope efficiency η depending on the temperature. As expected the threshold current increases and the slope efficiency decreases with an increasing temperature. Adding the lines for a guide to the eye.

4.2.3 Laser profile and beam shaping

Straight out of the box, laser diodes usually have a fast and slow axis, corresponding to a fast and slow diverging laser beam to the respective axis. Hence, one needs to treat both axis separated from each other, which can be achieved with cylindrical lenses. In this context, we further talk about the horizontal (x) - and vertical (y) - beam axis.

In general, most laser beams are described by Gaussian beams, which are transverse electromagnetic (TEM) modes, often the TEM_{00} mode. The intensity distri-

bution of a Gaussian beam is given by

$$I(r,z) = I_0 \left(\frac{w_0}{w(z)} \right)^2 \exp\left(\frac{-2r^2}{w^2(z)} \right) . \tag{4.1}$$

Here, I_0 denotes the maximum intensity, z is the axial distance from the beam focus and r is the radial distance from the beam axis. The function $w(z)$ is called the spot size function an looks like

$$w(z) = w_0 \sqrt{1 + \frac{z^2}{z_\mathrm{R}^2}} . \tag{4.2}$$

The parameter w_0 is called the beam waist and is used to calculate the Rayleigh range $z_\mathrm{R} = \frac{\pi w_0^2 n}{\lambda}$, with n the refractive index of the medium. The Rayleigh range is the distance from the waist of the beam, where the radius of the beam has increased by a factor of $\sqrt{2}$.

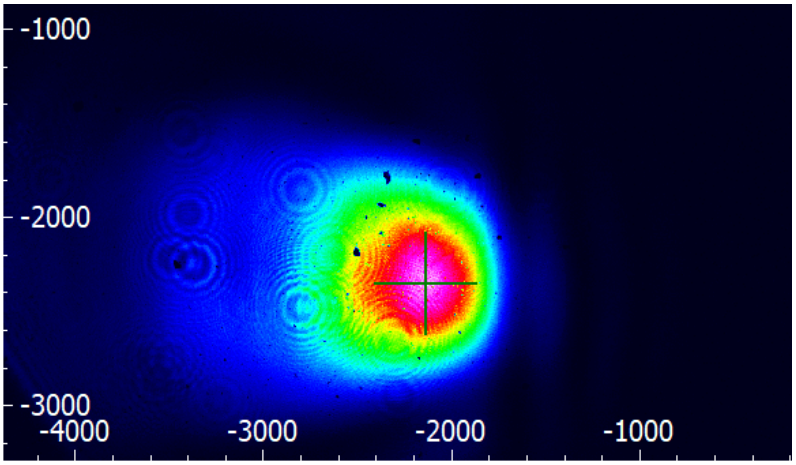

Figure 4.6: 2D laser profile recorded with a laser beam profiler. The intensity distribution goes from white (high) to blue (low). The center beam is quite round, although we can spot a faint tail on the left side of the beam.

With this in mind, we start to look at the beam radius after the laser housing. We placed the beam profiler into the laser beam at several points along the beam path and took a picture. For each 2D profile as shown in Fig. 4.6 we fit a Gaussian to the distribution and extract the radius by taking the FWHM of the Gaussian and dividing it by $\sqrt{2\ln(2)}$. After doing this for every measurement point, we get the respective plots in Figure 4.7.

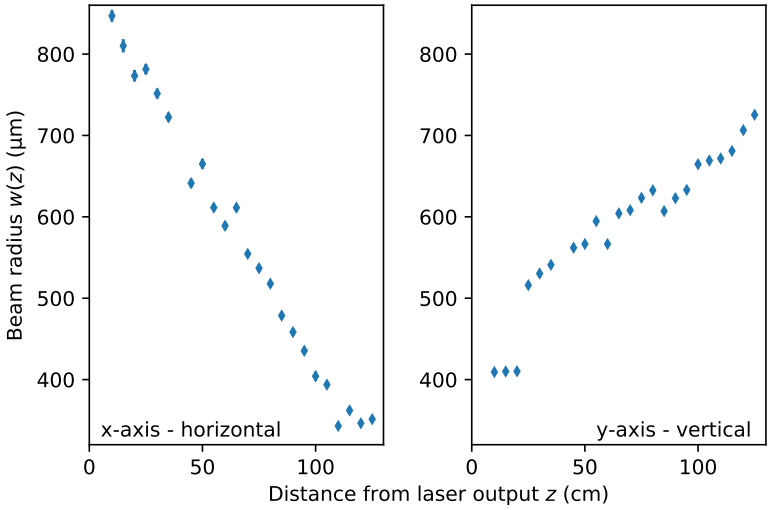

Figure 4.7: Beam radius of the horizontal and vertical beam axis after the laser housing. Since the data points are only stemming from single snapshots the errors are quite small.

We discover that the horizontal axis is converging, whereas the vertical axis is already diverging after the laser housing. Although the beam diameter should be small enough for the optical isolators IO-3-633-LP [3] we found strange patterns when trying to send them through the isolators. Hence, we decided to shape and collimate the beam already before the isolators. This is not recommended because every back reflection into the laser cavity causes instabilities. Thus, the optics should not be aligned perfectly to prevent this from happening. Later on in the project we found that one lens was still aligned too well, which caused the laser to behave worse than expected.

After the beam shaping optics we placed two optical Faraday isolators, which had a total transmission of around 76 % and a total isolation of 74 dB. Due to a damaged screw, we were unable to fully maximize transmission and isolation. Nevertheless, we would still miss out on a couple of percent and dB even if we tuned this one correctly.

[3] You can find the datasheet of the isolators at https://www.thorlabs.com/

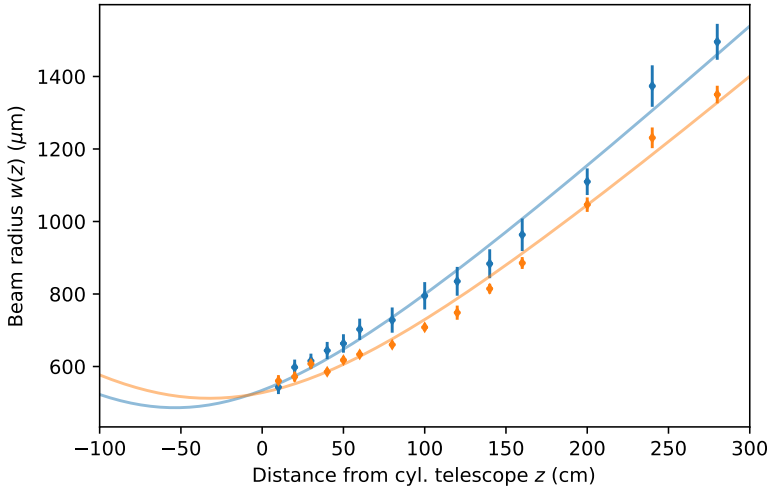

Figure 4.8: Beam radius measurement after the cylindrical telescope. Horizontal beam radius and fit in blue, vertical beam radius and fit in orange. Still a bit too much astigmatism left.

4.2.4 AOM characteristics

Since experiments often need lasers with different frequencies in the MHz regime, it is common to use an acousto-optic modulator (AOM). It can also serve as a fast switch to switch the light on and off. We will not go into detail here, but the base line is that AOMs can shift the frequency of laser beams usually by a couple to hundreds of MHz. This is enabled by the interaction of RF sound waves and light in a crystalline material. A piezoelectric transducer is driven by an RF signal and induces compression and rarefaction in the crystal and, therefore, changes in the refractive index. Incoming laser light is diffracted at this "grating" of the refractive index when set up correctly.

Usually a small percentage of light is lost as a result of absorption in the crystal and reflections, which is called insertion loss. This is usually on the order of a couple percent. A more important parameter is the diffraction efficiency $\varepsilon = P_1/P_{\text{tot}}$, which relates how much power is diffracted in the first order P_1 when the RF signal is turned on, to the total power after the crystal P_{tot} when the signal is turned off. The maximum diffraction efficiency is highly dependent on the beam size, wavelength, and the material used.

After measuring the diffraction efficiency for various RF powers, we get the data

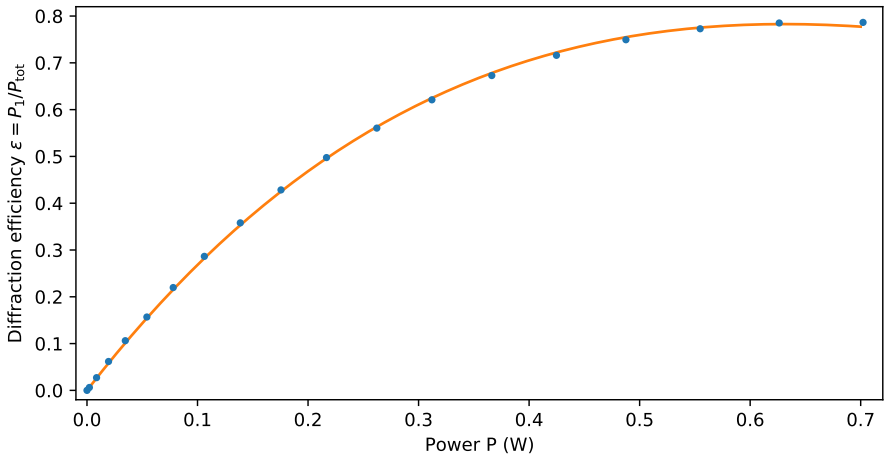

Figure 4.9: Diffraction efficiency of the AOM depending on the input RF power P. At around 0.6 W the saturation power is reached.

points in Figure 4.10. From the relative efficiency

$$\varepsilon = \sin^2\left(\frac{\pi}{2}\sqrt{P/P_{\text{sat}}}\right) \tag{4.3}$$

we can determine the saturation power $P_{\text{sat}} = 0.636(4)\,\text{W}$ and the maximum diffraction efficiency $\varepsilon_{\text{max}} = 0.784(2)$, which is close to the datasheet values of the AOMO 3110-120 [4].

At some point you may also need higher frequency shifts, which can be accomplished by a double-pass setup. Here, the laser beam gets diffracted into the first order, and (simply) reflected back through the AOM to get two times the RF shift added to it. Because of the fact that we need to guide the light to the experiment later on, we have to couple the laser beam into a single mode fiber. Both the double pass diffraction efficiency and the fiber coupling efficiency η are displayed together in Figure 4.10.

The center frequency of the AOM is $\nu_c = 110\,\text{MHz}$. Note that the frequency in the plot corresponds to the drive frequency and not the total frequency added to the laser. One usually only uses the frequency range within the FWHM of the total efficiency η_{tot}, which is in our case FWHM $= 2 \times 60\,\text{MHz}$ due to the double pass.

[4]Datasheet of the AOM can be found at https://gandh.com/

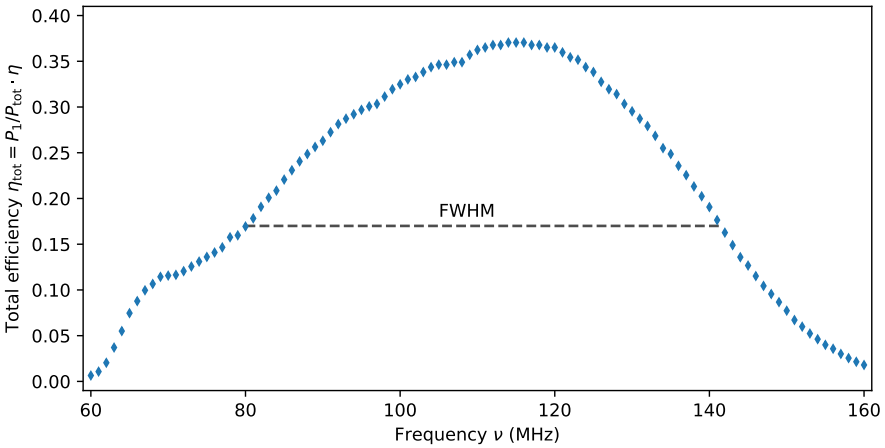

Figure 4.10: Total efficiency of the double pass and the fiber coupling combined. The FWHM is usually the range where you work in.

4.3 Setup of the system

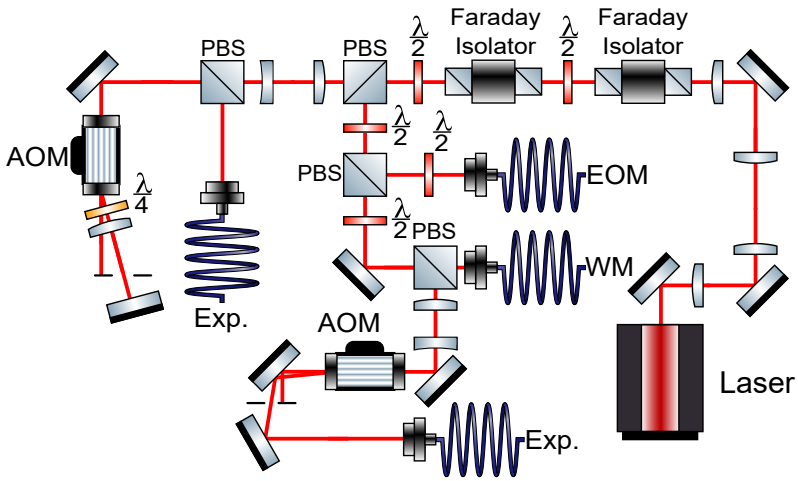

Figure 4.11: Sketch of the laser table setup. The laser beam exits the aluminium housing on the bottom right, passing a series of mirrors and lenses, before it is transmitted through optical isolators to reduce back reflections. It is then split up to be measured in a wavemeter, modulated in an EOM and shifted by two AOMs. The beams are then coupled into the blue and yellow fibers and connected to their final destination. More precise description in the text. Most of the components are taken from the ComponentLibrary of Alexander Franzen.

As discussed above, the setup in Figure 4.11 consists of the laser housing followed by a cylindrical telescope to shape the beam and another telescope to collimate the

beam. Two Faraday isolators reduce back reflections from the later part of the setup. Half-wave and quarter-wave plates help to split up the light at polarizing beam splitter cubes (PBS). In total, we have four fibers connected to the setup. Two of these are placed after a single- and double-pass AOM. One goes directly into a wavemeter (WM) and the other one is connected to an electro-optic modulator (EOM), covered in the next chapter. The AOMs both need a 2:1 ratio telescope to fit the laser beam through the aperture. Figure 4.12 shows the real-life setup of the breadboard on the laser table.

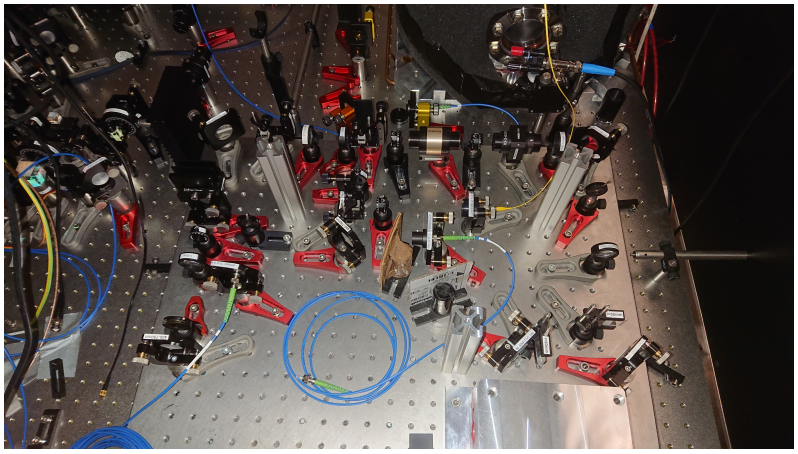

Figure 4.12: Real life setup of the laser and optics. There is still the path to the single-pass AOM missing. The iris at the right side of the beam path is used to mostly get rid of the wing in Fig. 4.6.

4.3.1 Pound-Drever-Hall stabilization

The last remaining fiber, connecting the laser setup with an electro-optic modulator serves a specific cause. While the laser is temperature controlled, isolated from vibrations on an optical table, and driven by a quite stable current, it still does not have the necessary stability and wavelength accuracy to be used in an experiment with ultracold atoms. One method to improve this is the Pound-Drever-Hall stabilization technique [79, 80]. The quintessence of this technique is to lock a laser frequency by modulating RF sidebands onto the laser, passing it through a high-finesse Fabry-Pérot cavity, and generating an error signal with a fast photo diode, which can be fed back to a PID controller regulating the piezo voltage and drive current.

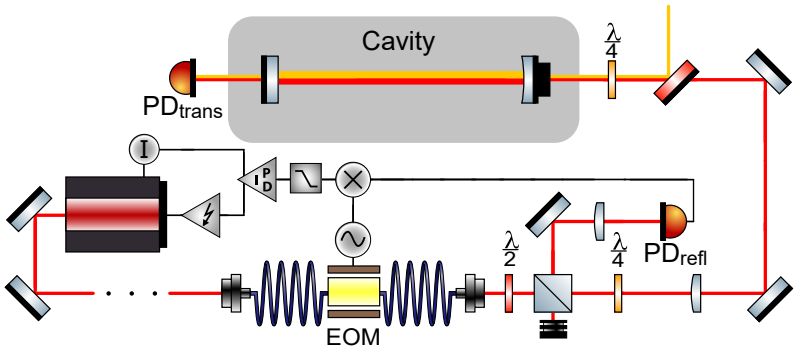

Figure 4.13: Sketch of the EOM laser setup, the cavity laser path and the control electronics behind the frequency lock of the laser. Light passes the EOM, get modulated, goes through the cavity and gets registered by a photo diode. The signals get analyzed and drive a PID controller which allows to lock the laser.

The small sketch in Figure 4.13 shows the rough locking design. The laser beam is coupled into a fiber going through an EOM. An rf wave generator is driving the EOM and modulating a sideband onto the laser light. The laser beam is matched to the stable reference cavity focus with a lens and overlapped with a 583 nm beam through a dichroic mirror. The reflection of the cavity is brought back to a fast photodiode whose signal is mixed with the rf wave generator to obtain the error signal. This is fed through a lowpass filter into the PID controller. When choosing the P, I, and D components of the controller appropriately, we can lock the laser to the stable reference cavity.

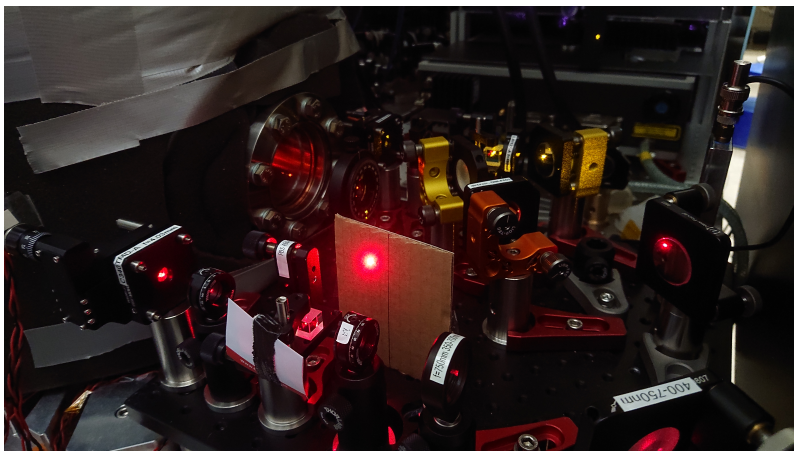

Figure 4.14: Real life cavity path setup without the photodiode. Light comes from the fiber outcoupler on the left and follows the U turn to the cavity, where it gets overlapped with the yellow laser beam.

The slow and course adjustment of the frequency is obtained by a piezoelectric element sitting in the flexure of the laser and is driven by a high voltage. The fast and fine correction of the frequency is given by the PID changing the drive current of the laser diode. Together, they allow for precise stabilization of the laser diode.

In Figure 4.15 we show the total frequency range accessible by the piezo sweep in blue. The orange data shows the cavity transmission signal arbitrarily scaled. The two highest peaks within the rising piezo voltage indicate the TEM_{00} modes of the cavity that are one free spectral range $\nu_{\mathrm{FSR}} = \frac{c}{2L} = 1\,\mathrm{GHz}$ apart. Here, c denotes the speed of light and $L = 15\,\mathrm{cm}$ is the length of the cavity [81]. All smaller peaks, except the ones symmetric around the big peak, are higher TEM_{nm} modes, which were minimized when coupling the laser to the cavity.

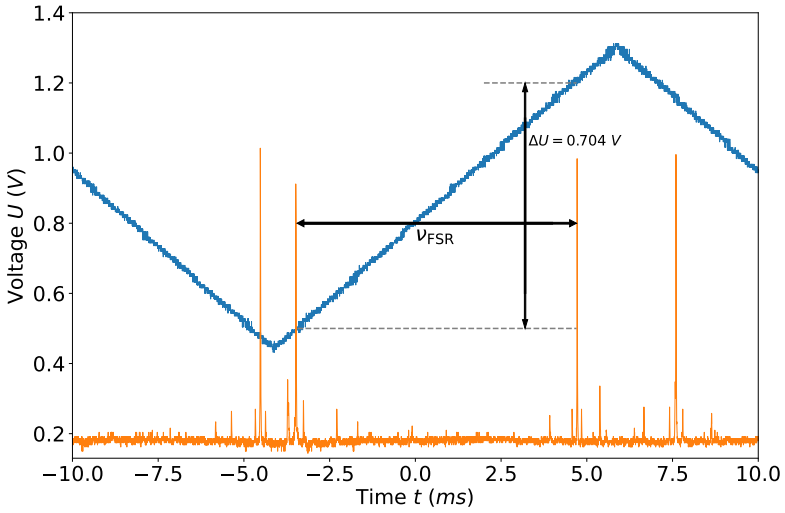

Figure 4.15: Total voltage sweep (blue) over the piezo range. blue Piezo sweep monitor voltage, orange cavity transmission arbitrarily scaled

To verify the correct coupling of the laser to the cavity we record a couple of error signals, similar to that in Figure 4.16. In total, we fit 15 signals with the error function

$$\varepsilon(\Delta) = c + A\Gamma\Omega\Delta \frac{\Gamma \sin\Phi[\Gamma^2 + \Omega^2 + \Delta^2] + \Omega\cos\Phi[\Gamma^2 + \Omega^2 - \Delta^2]}{[\Gamma^2 + \Delta^2][\Gamma^2 + (\Delta+\Omega)^2][\Gamma^2 + (\Delta-\Omega)^2]}\,, \tag{4.4}$$

which allows us to determine the linewidth Γ of the cavity. Here, c is an arbitrary offset, A is a general amplitude, Ω denotes the sideband modulation frequency, Φ is an arbitrary phase between the signals at the mixer, and Δ is the detuning from the

cavity resonance. By averaging the fits of the recorded samples, we get a linewidth of $\Gamma = 558(44)\,\mathrm{kHz}$ with the error being the standard deviation. It is close to the values measured in [81]. In the end we achieved a stable lock to a wavelength close to the transition in erbium.

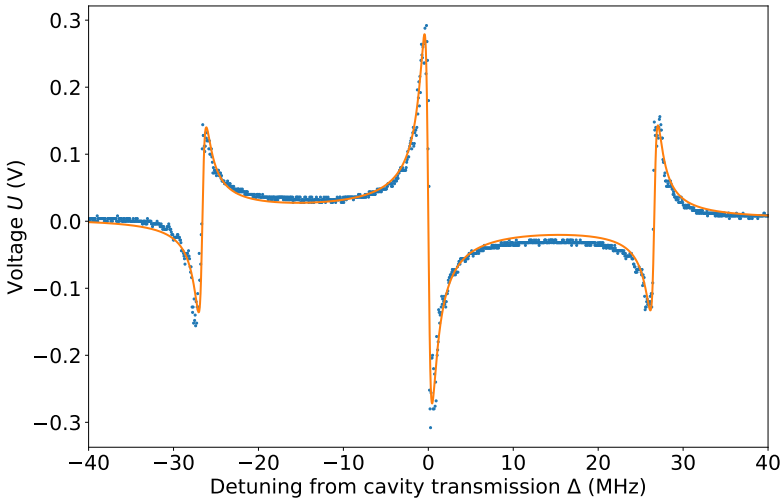

Figure 4.16: Error signal obtained from the PDH technique. The signal is fitted with the function $\varepsilon(\Delta)$ written in Eq. 4.4.

4.4 Temperature stabilization problems

At one point during the final tests of locking the laser, we observed temperature drifts as shown in Fig. 4.17. We proceeded to open up the laser housing and found that the laser diode mount was warm rather than chilly. After some superficial inspections of the electronics, we finally found a connection between the laser housing and the negative terminal of the housing temperature PID. We thought that the soldered connections of the peltier elements on the bottom may touch the ground plate.

While we pondered about nondestructive ways to rectify this situation, we discovered that the peltier element on the diode holder was tilted. We unscrewed the copper thermal bridge and found that the peltier element was completely broken into two pieces, see Fig. 4.18. A dead peltier element on the diode holder meant a complete disassembly of the laser. The broken peltier element needed to be milled out, and a new one was glued in place. Because we had to readjust the laser anyway

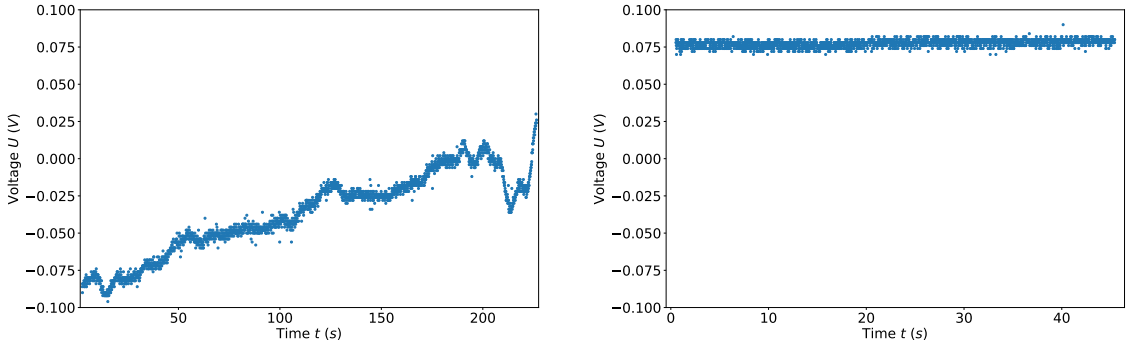

Figure 4.17: (left) Temperature error signal of the laser diode holder fluctuating around, not converging to zero, suggesting there is something wrong. (right) Temperature error signal of the laser housing showing a constant offset, which also suggests something may be broken.

we also fixed the soldering spots on the bottom peltier elements too. Finally, we adjusted the laser diode mount again by maximizing the output of the laser, when turning the position screws. In the end, we managed to get the laser back up and running without any more inconveniences.

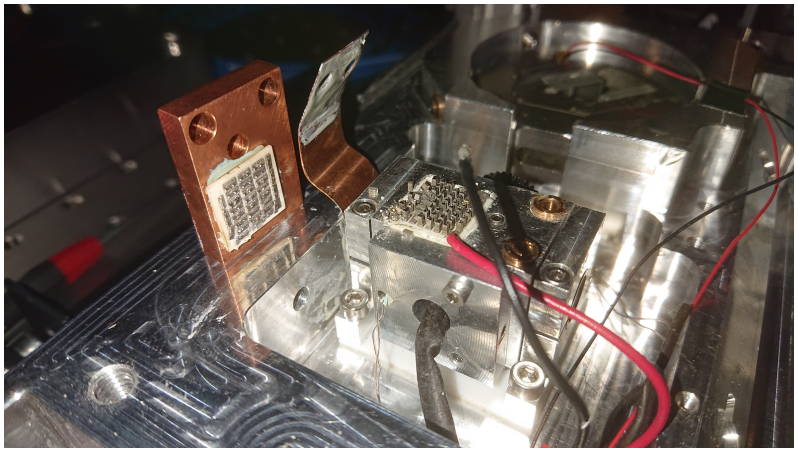

Figure 4.18: The culprit: Dead peltier element - possibly due to bad connections.

Chapter 5

Conclusion & Outlook

We have covered the most important properties and interactions of erbium and ultracold quantum gases in general. Basic knowledge was followed by a more in-depth study of things like the different methods for calculating the ground states of ultracold quantum gases in lattice geometries. These methods show a similar result for $s = 1\,\mathrm{E_{r,532}}$ in our geometrical arrangement. Further, we took a quick look at Bloch oscillation theory and derived a discrete quasi one-dimensional variational Gross-Pitaevskii equation from scratch inspired by Ref. [68]. This helped us compare our experimental measurements [20] and understand the physics behind Bloch oscillations in dipolar quantum gases. We analyzed the obtained data and tried to explain the rich features of it. When going to lower scattering lengths, the ground states move to one lattice site and the dephasing rates of Bloch oscillations possess a minimum on the way there. In the last chapter, we built a laser system from the ground up and explained everything along the way. We showed the characteristics of the diode, the threshold current and the slope efficiency. We characterized and shaped the laser beam to fit the demand and talked about various types of modulators that are needed in the process to prepare frequency shifted beams. The laser was locked to a stable reference cavity with a linewidth of $\Gamma = 558(44)\,\mathrm{kHz}$. This was achieved with the PDH technique by controlling the voltage applied to a piezo and the current at the laser diode. In the end, the laser suffered from dead peltier elements, which denied the temperature stabilization of the laser.

Improvements can be made in the study of both the GPE and GW ground state calculations, by finding a parameter which declare the regions in which these methods are viable. Further one could study the time dependent lattice loading of

bosons also in the context of both approaches.

The discrete variational model we derived allows for a fast calculation of the variational ground state and subsequently also for the time evolution of the state under influence of the external force. But it lacks some (maybe) import physical considerations, such as the change of the aspect ratio η during the time evolution. Additionally, it keeps the condensate width fixed at each lattice site, which is a major approximation. To remove all the inconveniences, one should conduct the simulations in all three dimensions without approximations.

We also showed that the dependence of the dephasing rate on the scattering length and atom number is non-trivial and, in fact, may be related to the variance of the chemical potential of the different lattice sites [20], although it does not match with the observed minima for most of the simulated atom number range.

Previous experiments have shown that optical transitions with a smaller linewidth are suitable for implementation in a post-MOT cooling stage [18, 19]. Therefore, we might be trying to implement this in the future. Other possible use cases could be for precision spectroscopy, as already done recently with the 1299 nm line in erbium [30]. One could also use the laser to manipulate the spin sublevels of erbium to generate different topologies.

Bibliography

[1] M. H. Anderson, J. R. Ensher, M. R. Matthews, C. E. Wieman, and E. A. Cornell. Observation of Bose-Einstein Condensation in a Dilute Atomic Vapor. *Science*, 269(5221):198–201, 1995.

[2] K. B. Davis, M. O. Mewes, M. R. Andrews, N. J. van Druten, D. S. Durfee, D. M. Kurn, and W. Ketterle. Bose-Einstein Condensation in a Gas of Sodium Atoms. *Phys. Rev. Lett.*, 75:3969–3973, Nov 1995.

[3] Jürgen Stuhler, Axel Griesmaier, Tobias Koch, Marco Fattori, and Tilman Pfau. Magnetostriction in a degenerate quantum gas. *Journal of Magnetism and Magnetic Materials*, 316(2):429–432, 2007. Proceedings of the Joint European Magnetic Symposia.

[4] D. Baillie, R. M. Wilson, R. N. Bisset, and P. B. Blakie. Self-bound dipolar droplet: A localized matter wave in free space. *Phys. Rev. A*, 94:021602, Aug 2016.

[5] L. Chomaz, R. M. W. van Bijnen, D. Petter, G. Faraoni, S. Baier, J. H. Becher, M. J. Mark, F. Wächtler, L. Santos, and F. Ferlaino. Observation of roton mode population in a dipolar quantum gas. *Nature Physics*, 14(5):442–446, May 2018.

[6] Fabian Böttcher, Jan-Niklas Schmidt, Matthias Wenzel, Jens Hertkorn, Mingyang Guo, Tim Langen, and Tilman Pfau. Transient supersolid properties in an array of dipolar quantum droplets. *Phys. Rev. X*, 9:011051, Mar 2019.

[7] L. Chomaz, D. Petter, P. Ilzhöfer, G. Natale, A. Trautmann, C. Politi, G. Durastante, R. M. W. van Bijnen, A. Patscheider, M. Sohmen, M. J. Mark,

and F. Ferlaino. Long-lived and transient supersolid behaviors in dipolar quantum gases. *Phys. Rev. X*, 9:021012, Apr 2019.

[8] L. Tanzi, E. Lucioni, F. Famà, J. Catani, A. Fioretti, C. Gabbanini, R. N. Bisset, L. Santos, and G. Modugno. Observation of a dipolar quantum gas with metastable supersolid properties. *Phys. Rev. Lett.*, 122:130405, Apr 2019.

[9] Felix Bloch. Über die Quantenmechanik der Elektronen in Kristallgittern. *Zeitschrift für Physik*, 52(7-8):555–600, 1929.

[10] Clarence Zener and Ralph Howard Fowler. Non-adiabatic crossing of energy levels. *Proceedings of the Royal Society of London. Series A, Containing Papers of a Mathematical and Physical Character*, 137(833):696–702, 1932.

[11] Maxime Ben Dahan, Ekkehard Peik, Jakob Reichel, Yvan Castin, and Christophe Salomon. Bloch Oscillations of Atoms in an Optical Potential. *Phys. Rev. Lett.*, 76:4508–4511, Jun 1996.

[12] Ekkehard Peik, Maxime Ben Dahan, Isabelle Bouchoule, Yvan Castin, and Christophe Salomon. Bloch oscillations of atoms, adiabatic rapid passage, and monokinetic atomic beams. *Phys. Rev. A*, 55:2989–3001, Apr 1997.

[13] M. Gustavsson, E. Haller, M. J. Mark, J. G. Danzl, G. Rojas-Kopeinig, and H.-C. Nägerl. Control of Interaction-Induced Dephasing of Bloch Oscillations. *Phys. Rev. Lett.*, 100:080404, Feb 2008.

[14] G. Ferrari, N. Poli, F. Sorrentino, and G. M. Tino. Long-Lived Bloch Oscillations with Bosonic Sr Atoms and Application to Gravity Measurement at the Micrometer Scale. *Phys. Rev. Lett.*, 97:060402, Aug 2006.

[15] M. Fattori, C. D'Errico, G. Roati, M. Zaccanti, M. Jona-Lasinio, M. Modugno, M. Inguscio, and G. Modugno. Atom Interferometry with a Weakly Interacting Bose-Einstein Condensate. *Phys. Rev. Lett.*, 100:080405, Feb 2008.

[16] M. Fattori, G. Roati, B. Deissler, C. D'Errico, M. Zaccanti, M. Jona-Lasinio, L. Santos, M. Inguscio, and G. Modugno. Magnetic Dipolar Interaction in a Bose-Einstein Condensate Atomic Interferometer. *Phys. Rev. Lett.*, 101:190405, Nov 2008.

[17] T. D. Lee, Kerson Huang, and C. N. Yang. Eigenvalues and Eigenfunctions of a Bose System of Hard Spheres and Its Low-Temperature Properties. *Phys. Rev.*, 106:1135–1145, Jun 1957.

[18] Mingwu Lu, Seo Ho Youn, and Benjamin L. Lev. Spectroscopy of a narrow-line laser-cooling transition in atomic dysprosium. *Phys. Rev. A*, 83:012510, Jan 2011.

[19] Gregory A. Phelps, Anne Hébert, Aaron Krahn, Susannah Dickerson, Furkan Öztürk, Sepehr Ebadi, Lin Su, and Markus Greiner. Sub-second production of a quantum degenerate gas, 2020.

[20] Gabriele Natale, Thomas Bland, Simon Gschwendtner, Louis Lafforgue, Daniel S. Grün, Alexander Patscheider, Manfred J. Mark, and Francesca Ferlaino. Bloch oscillations and matter-wave localization of a dipolar quantum gas in a one-dimensional lattice. *Communications Physics*, 5(1):227, Sep 2022.

[21] Claude Piguet. Extricating erbium. *Nature Chemistry*, 6(4):370–370, Apr 2014.

[22] Masataka Nakazawa, Yasuo Kimura, and Kazunori Suzuki. Efficient Er^{3+}-doped optical fiber amplifier pumped by a 1.48 µm InGaAsP laser diode. *Applied Physics Letters*, 54(4):295–297, 1989.

[23] I. F. Storchi, S. Parker, F. Bovis, S. Benedicenti, and A. Amaroli. Outpatient erbium:YAG (2940 nm) laser treatment for snoring: a prospective study on 40 patients. *Lasers Med Sci*, 33(2):399–406, Feb 2018.

[24] C. Neruntarat, K. Khuancharee, and P. Shoowit. Er:YAG laser for snoring: a systemic review and meta-analysis. *Lasers Med Sci*, 35(6):1231–1238, Aug 2020.

[25] John R. de Laeter, John Karl Böhlke, P. De Bièvre, H. Hidaka, H. S. Peiser, K. J. R. Rosman, and P. D. P. Taylor. Atomic weights of the elements. Review 2000 (IUPAC Technical Report). *Pure and Applied Chemistry*, 75(6):683–800, 2003.

[26] C.J. Foot. *Atomic physics*. Oxford master series in physics. Oxford University Press, 2005.

[27] W. C. Martin, R. Zalubas, and L. Hagan. *Atomic energy levels - the rare earth elements. (the spectra of lanthanum, cerium, praseodymium, neodymium, promethium, samarium, europium, gadolinium, terbium, dysprosium, holmium, erbium, thulium, ytterbium, and lutetium). [66 atoms and ions]*. NSRDS-NBS, Washington: National Bureau of Standards, U.S. Department of Commerce, |c1978, United States, 1978. Research Org.: Manchester Coll. of Science and Technology (UK). Dept. of Chemistry.

[28] A. Kramida, Yu. Ralchenko, J. Reader, and NIST ASD Team. NIST Atomic Spectra Database (ver. 5.9), [Online]. Available: https://physics.nist.gov/asd [2021, November 16]. National Institute of Standards and Technology, Gaithersburg, MD., 2021.

[29] H. Y. Ban, M. Jacka, J. L. Hanssen, J. Reader, and J. J. McClelland. Laser cooling transitions in atomic erbium. *Opt. Express*, 13(8):3185–3195, Apr 2005.

[30] A. Patscheider, B. Yang, G. Natale, D. Petter, L. Chomaz, M. J. Mark, G. Hovhannesyan, M. Lepers, and F. Ferlaino. Observation of a narrow inner-shell orbital transition in atomic erbium at 1299 nm. *Phys. Rev. Research*, 3:033256, Sep 2021.

[31] A. Frisch, K. Aikawa, M. Mark, A. Rietzler, J. Schindler, E. Zupanič, R. Grimm, and F. Ferlaino. Narrow-line magneto-optical trap for erbium. *Phys. Rev. A*, 85:051401, May 2012.

[32] J. H. Becher, S. Baier, K. Aikawa, M. Lepers, J.-F. Wyart, O. Dulieu, and F. Ferlaino. Anisotropic polarizability of erbium atoms. *Phys. Rev. A*, 97:012509, Jan 2018.

[33] J. G. Conway and B. G. Wybourne. Low-Lying Energy Levels of Lanthanide Atoms and Intermediate Coupling. *Phys. Rev.*, 130:2325–2332, Jun 1963.

[34] E. T. Davletov, V. V. Tsyganok, V. A. Khlebnikov, D. A. Pershin, D. V. Shaykin, and A. V. Akimov. Machine learning for achieving bose-einstein condensation of thulium atoms. *Phys. Rev. A*, 102:011302, Jul 2020.

[35] Albert Frisch. *Dipolar quantum gases of Erbium*. PhD thesis, University of Innsbruck, 2014.

[36] ed. David R. Lide. *CRC Handbook of Chemistry.* CRC Press, Boca Raton, FL, 2005, Internet Version 2005.

[37] P. Ilzhöfer, G. Durastante, A. Patscheider, A. Trautmann, M. J. Mark, and F. Ferlaino. Two-species five-beam magneto-optical trap for erbium and dysprosium. *Phys. Rev. A*, 97:023633, Feb 2018.

[38] L. D. Landau and E. M. Lifshitz. *Quantum Mechanics.* Pergamon, third edition, 1977.

[39] C. J. Pethick and H. Smith. *Bose–Einstein Condensation in Dilute Gases.* Cambridge University Press, 2 edition, 2008.

[40] Yijun Tang, Wil Kao, Kuan-Yu Li, and Benjamin L. Lev. Tuning the Dipole-Dipole Interaction in a Quantum Gas with a Rotating Magnetic Field. *Phys. Rev. Lett.*, 120:230401, Jun 2018.

[41] T Lahaye, C Menotti, L Santos, M Lewenstein, and T Pfau. The physics of dipolar bosonic quantum gases. *Reports on Progress in Physics*, 72(12):126401, Nov 2009.

[42] B. Marcelis, E. G. M. van Kempen, B. J. Verhaar, and S. J. J. M. F. Kokkelmans. Feshbach resonances with large background scattering length: Interplay with open-channel resonances. *Phys. Rev. A*, 70:012701, Jul 2004.

[43] A. J. Moerdijk, B. J. Verhaar, and A. Axelsson. Resonances in ultracold collisions of ^{6}Li, ^{7}Li, and ^{23}Na. *Phys. Rev. A*, 51:4852–4861, Jun 1995.

[44] Albert Frisch, Michael Mark, Kiyotaka Aikawa, Francesca Ferlaino, John L. Bohn, Constantinos Makrides, Alexander Petrov, and Svetlana Kotochigova. Quantum chaos in ultracold collisions of gas-phase erbium atoms. *Nature*, 507(7493):475–479, Mar 2014.

[45] T. Maier, H. Kadau, M. Schmitt, M. Wenzel, I. Ferrier-Barbut, T. Pfau, A. Frisch, S. Baier, K. Aikawa, L. Chomaz, M. J. Mark, F. Ferlaino, C. Makrides, E. Tiesinga, A. Petrov, and S. Kotochigova. Emergence of Chaotic Scattering in Ultracold Er and Dy. *Phys. Rev. X*, 5:041029, Nov 2015.

[46] Lauriane Chomaz, Igor Ferrier-Barbut, Francesca Ferlaino, Bruno Laburthe-Tolra, Benjamin L. Lev, and Tilman Pfau. Dipolar physics: A review of experiments with magnetic quantum gases, 2022.

[47] Y. Tang, A. G. Sykes, N. Q. Burdick, J. M. DiSciacca, D. S. Petrov, and B. L. Lev. Anisotropic expansion of a thermal dipolar bose gas. *Phys. Rev. Lett.*, 117:155301, Oct 2016.

[48] A. Patscheider, L. Chomaz, G. Natale, D. Petter, M. J. Mark, S. Baier, B. Yang, R. R. W. Wang, J. L. Bohn, and F. Ferlaino. Accurate determination of the scattering length of erbium atoms, 2021.

[49] F. Reif and R. Federick. *Fundamentals of Statistical and Thermal Physics*. Number Bd. 10 in Fundamentals of Physics Series. McGraw-Hill, 1965.

[50] W. Kohn. Analytic properties of bloch waves and wannier functions. *Phys. Rev.*, 115:809–821, Aug 1959.

[51] Dieter Jaksch. *Bose-Einstein Condensation and Applications*. PhD thesis, University of Innsbruck, 1999.

[52] Martin C. Gutzwiller. Effect of correlation on the ferromagnetism of transition metals. *Phys. Rev. Lett.*, 10:159–162, Mar 1963.

[53] Daniel S. Rokhsar and B. G. Kotliar. Gutzwiller projection for bosons. *Phys. Rev. B*, 44:10328–10332, Nov 1991.

[54] Werner Krauth, Michel Caffarel, and Jean-Philippe Bouchaud. Gutzwiller wave function for a model of strongly interacting bosons. *Phys. Rev. B*, 45:3137–3140, Feb 1992.

[55] D. Jaksch, C. Bruder, J. I. Cirac, C. W. Gardiner, and P. Zoller. Cold Bosonic Atoms in Optical Lattices. *Phys. Rev. Lett.*, 81:3108–3111, Oct 1998.

[56] Wilhelm Zwerger. Mott–Hubbard transition of cold atoms in optical lattices. *Journal of optics. B, Quantum and semiclassical optics*, 5(2):S9–S16, 2003.

[57] E. P. Gross. Structure of a quantized vortex in boson systems. *Il Nuovo Cimento (1955-1965)*, 20(3):454–477, May 1961.

[58] L. P. Pitaevskii. Vortex lines in an imperfect bose gas. *Sov. Phys. JETP*, 13(2):451–454, 1961.

[59] Carlo Barenghi and Nick G. Parker. A Primer on Quantum Fluids. *SpringerBriefs in Physics*, 2016.

[60] Juha Javanainen and Janne Ruostekoski. Symbolic calculation in development of algorithms: split-step methods for the gross–pitaevskii equation. *Journal of Physics A: Mathematical and General*, 39(12):L179, mar 2006.

[61] T Hartmann, F Keck, H J Korsch, and S Mossmann. Dynamics of Bloch oscillations. *New Journal of Physics*, 6:2–2, jan 2004.

[62] Zachary A. Geiger, Kurt M. Fujiwara, Kevin Singh, Ruwan Senaratne, Shankari V. Rajagopal, Mikhail Lipatov, Toshihiko Shimasaki, Rodislav Driben, Vladimir V. Konotop, Torsten Meier, and David M. Weld. Observation and Uses of Position-Space Bloch Oscillations in an Ultracold Gas. *Phys. Rev. Lett.*, 120:213201, May 2018.

[63] D. Witthaut, M. Werder, S. Mossmann, and H. J. Korsch. Bloch oscillations of Bose-Einstein condensates: Breakdown and revival. *Phys. Rev. E*, 71:036625, Mar 2005.

[64] Aristeu R. P. Lima and Axel Pelster. Quantum fluctuations in dipolar bose gases. *Phys. Rev. A*, 84:041604, Oct 2011.

[65] A. R. P. Lima and A. Pelster. Beyond mean-field low-lying excitations of dipolar Bose gases. *Phys. Rev. A*, 86:063609, Dec 2012.

[66] R. N. Bisset, R. M. Wilson, D. Baillie, and P. B. Blakie. Ground-state phase diagram of a dipolar condensate with quantum fluctuations. *Phys. Rev. A*, 94:033619, Sep 2016.

[67] S. Sinha and L. Santos. Cold Dipolar Gases in Quasi-One-Dimensional Geometries. *Phys. Rev. Lett.*, 99:140406, Oct 2007.

[68] P Blair Blakie, D Baillie, and Sukla Pal. Variational theory for the ground state and collective excitations of an elongated dipolar condensate. *Communications in Theoretical Physics*, 72(8):085501, Jul 2020.

[69] Bureau Gravimetrique International (BGI). Absolute gravity data. AGrav: Absolute Gravity Database - Meta-Data, online available: http://agrav.bkg.bund.de/... (last accessed 7.02.2022).

[70] J.R. Dormand and P.J. Prince. A family of embedded Runge-Kutta formulae. *Journal of Computational and Applied Mathematics*, 6(1):19–26, 1980.

[71] A. V. Ponomarev and A. R. Kolovsky. Dipole and bloch oscillations of cold atoms in a parabolic lattice. *Laser Physics*, 16(2):367–370, Feb 2006.

[72] L. Salasnich, A. Parola, and L. Reatto. Effective wave equations for the dynamics of cigar-shaped and disk-shaped bose condensates. *Phys. Rev. A*, 65:043614, Apr 2002.

[73] Mitchell J. Knight, Thomas Bland, Nick G. Parker, and Andy M. Martin. Improved low-dimensional wave equations for cigar-shaped and disk-shaped dipolar Bose-Einstein condensates, 2019.

[74] F. J. Duarte. *Tunable Laser Applications*. Optical Science and Engineering. CRC Press, 2 edition, 2008.

[75] Michael G. Littman and Harold J. Metcalf. Spectrally narrow pulsed dye laser without beam expander. *Appl. Opt.*, 17(14):2224–2227, Jul 1978.

[76] Karen Liu and Michael G. Littman. Novel geometry for single-mode scanning of tunable lasers. *Opt. Lett.*, 6(3):117–118, Mar 1981.

[77] E. Kirilov, M. J. Mark, M. Segl, and H.-C. Nägerl. Compact, robust, and spectrally pure diode-laser system with a filtered output and a tunable copy for absolute referencing. *Applied Physics B*, 119(2):233–240, May 2015.

[78] C. J. Hawthorn, K. P. Weber, and R. E. Scholten. Littrow configuration tunable external cavity diode laser with fixed direction output beam. *Review of Scientific Instruments*, 72(12):4477–4479, 12 2001.

[79] R. W. P. Drever, J. L. Hall, F. V. Kowalski, J. Hough, G. M. Ford, A. J. Munley, and H. Ward. Laser phase and frequency stabilization using an optical resonator. *Applied Physics B*, 31(2):97–105, Jun 1983.

[80] Eric D. Black. An introduction to Pound–Drever–Hall laser frequency stabilization. *American Journal of Physics*, 69(1):79–87, 01 2001.

[81] Alexander Patscheider. *Stable Reference Cavity for Er and Dy MOT Light.* PhD thesis, University of Innsbruck, 2017.

Appendix A

MATLAB code of Bloch oscillation simulations

This chapter features the MATLAB code of the variational Bloch oscillation simulation from the initialization of constants, through the calculation of the ground state and to the real time evolution of the variational wave function.

```
1
2  % Numerical propagation of the 1D DNPSE with ode45 including dipolar
3  % interaction and quantum fluctuations with a variational radial
4  % wavefunction and energy minimization during each imaginary time step
5  % Further evolving the system in real-time to observe Bloch oscillations
6
7  function [Psi_save_BO, Psi_save_q_BO, Psi_save_Exp_BO, l, eta] =
       Bloch_oscillation_simulation_variational_final(theta, phi, theta_gs, phi_gs, s, a, Natoms,
       ExpansionTime, omega_x, omega_y, omega_z, omega_x_BO, omega_y_BO, omega_z_BO, psi_x, l, eta,
       LHY, a_gs, DDI, evolution_params, Plot_energy, Print_energy_vals, shift_Vext)
8  clfall
9  beep off
10
11 %% --------- Constants ------------------------------------------------------
12
13 c    = 299792458;           % Speed of light [m/s]
14 kB   = 1.3806503e-23;       % Boltzmann constant [J/K]
15 h = 6.62607015e-34;         % Planck constant [Js]
16 hbar = 1.05457148e-34;      % Reduced Planck constant [Js]
17 muB  = 9.27400949e-24;      % Bohr magneton [J/T]
18 muB_G  = 9.27400949e-28;    % Bohr magneton [J/G]
19 mu0 = 4*pi*1e-7;            % Vacuum permeability [N/A^2]
20 grav = 9.80553;             % Acceleration of gravity [m/s^2]
21 u    = 1.6605e-27;          % Atomic mass unit [kg]
22 a0   = 0.5291772083e-10;    % Bohr's radius in [m]
23 m166 = 166*u;               % Mass of Er166 [kg]
24 m = m166;                   % Mass of used isotope [kg]
```

```
lambda = 1064e-9;           % Lattice wavelength [m];
kr = 2*pi/lambda;           % Lattice wavenumber [1/m]
omega_rec = hbar*kr^2/2/m;  % Recoil frequency [Hz]
G = 2*kr;                   % Brillouin zone width [1/m]
Er = hbar^2*kr^2/2/m;       % Recoil energy [J]
d = lambda/2;               % Lattice site spacing [m]

% theta = 0/180*pi;         % Angle between lattice and dipoles [rad] % 54.7456 magic angle
% phi = 0/180*pi; % Phi is 0 for B || x and 90 for B || y
% theta_gs = 90;
% phi_gs = 90;
mu = 6.98*muB;              % Magnetic dipole moment of atoms [J/T]
cut = 4;                    % At which lattice site (+-) the offsite interaction should be cut off
load(['EnergyOnOffsite4_Vz', int2str(s), '_Theta', int2str(theta_gs), '_Phi', int2str(phi_gs)], 'L'
     , 'Eta', 'UDDI', 'DDINNI', 'DDINNI2', 'DDINNI3', 'DDINNI4');
load('DDI2.mat', 'lsV', 'etaV', 'Esave');
% theta_gs = theta_gs/180*pi;
% phi_gs = phi_gs/180*pi;

%% --------- Physical system start parameters -----------------------------

Fext = m*grav*0.9816;                       % Gravitational force *0.99982
TBloch = 2*pi*hbar/(Fext*d);                % Bloch period
T_max = 0.015;                              % Maximum evolution time (s)  T_max = 0.012 in lab
NumberBlochPeriods = round(T_max/TBloch);   % Number of Bloch oszillations to simulate
Steps = 21;                                 % Saved steps per BO
dt = TBloch/Steps;                          % Single time step dt for BO
saves = 1 + NumberBlochPeriods*Steps;       % Number of saved wave functions

N = 401;                  % Number of Wells, must be odd to include 0
% s = 8;                  % Lattice Depth in Er
% a = 50;                 % Scattering length in a0
a_copy = a;
if a_gs == inf
    a = a*a0;
else
    a = a_gs*a0;
end
g = 4*pi*hbar^2*a/m;      % Contact interaction constant

% Natoms = 4e4;           % Number of atoms
% ExpansionTime = 30e-3;  % End expansion time

% omega_x = 34*2*pi;      % Trap frequency in x
% omega_y = 217*2*pi;     % Trap frequency in y
% omega_z = 240*2*pi;     % Trap frequency in z

l_x = sqrt(hbar/(m*omega_x));   % Harmonic oscillator length in x
l_y = sqrt(hbar/(m*omega_y));   % Harmonic oscillator length in y
l_z = sqrt(hbar/(m*omega_z));   % Harmonic oscillator length in z

% l = sqrt(l_x*l_y);              % Mean harmonic oscillator length in radial direction
```

```
76 omega = hbar/(m*l^2);                % Mean trap frequency in radial direction
77 % eta = sqrt(omega_x/omega_y);       % Eta variational parameter describing the ratio of widths in x
       and y
78
79 omega_latt = 2*omega_rec*sqrt(s);  % Harmonic frequency of lattice
80 l_latt = sqrt(hbar/m/omega_latt);  % Oscillator length of lattice
81
82 C_dd = mu0*mu^2;                    % Dipolar constant
83 eps_dd = C_dd/(3*g);                % Fraction of dipolar and contact interaction
84
85 gamma_QF = LHY*abs(32/3*g*sqrt(a^3/pi)*(1 + 3/2*eps_dd^2)); % Quantum fluctuations constant
86 QF_factor = (2/(5*pi^(3/2)*l^2*l_latt))^(3/2)*gamma_QF;     % Quantum fluctuation quasi 1D
87
88 U_c_DNLS = g/((2*pi)^(3/2)*l^2*l_latt);                    % DNLS contact term
89
90 if DDI == 0
91     DD_onsite = interpn(L, Eta, UDDI, l, eta, 'spline')*h;
92     inter_DDINNI1 = interpn(L, Eta, DDINNI, l, eta, 'spline')*h;
93     inter_DDINNI2 = interpn(L, Eta, DDINNI2, l, eta, 'spline')*h;
94     inter_DDINNI3 = interpn(L, Eta, DDINNI3, l, eta, 'spline')*h;
95     inter_DDINNI4 = interpn(L, Eta, DDINNI4, l, eta, 'spline')*h;
96 elseif DDI == 1
97     DD_onsite = interpn(etaV, lsV, Esave(:, :, 1, 2), eta, l*1e6, 'spline');
98     inter_DDINNI1 = interpn(etaV, lsV, Esave(:, :, 2, 2), eta, l*1e6, 'spline');
99     inter_DDINNI2 = interpn(etaV, lsV, Esave(:, :, 3, 2), eta, l*1e6, 'spline');
100    inter_DDINNI3 = interpn(etaV, lsV, Esave(:, :, 4, 2), eta, l*1e6, 'spline');
101    inter_DDINNI4 = interpn(etaV, lsV, Esave(:, :, 5, 2), eta, l*1e6, 'spline');
102 end
103 DD_offsite = [inter_DDINNI4, inter_DDINNI3, inter_DDINNI2, inter_DDINNI1, 0, inter_DDINNI1,
       inter_DDINNI2, inter_DDINNI3, inter_DDINNI4];
104
105
106 %% --------- Needed calculations to start ---------------------------------
107
108 dq = 2*pi/(d*(N-1));                    % Quasi momentum spacing
109 x = (-d*(N-1)/2:d:d*(N-1)/2);           % Real space vector
110 k = (-dq*(N-1)/2:dq:dq*(N-1)/2);        % Momentum vector
111 q = (-dq*(N-1)/2:dq:dq*(N-1)/2)/kr;     % Quasi momentum vector
112 qexp = (-dq*(N-1):dq:dq*(N-1))/kr;      % Doubled Quasi momentum vector
113
114 PSI_save = zeros(saves, N);             % Empty matrix for wave functions Psi(t, x)
115 PSI_save_q = zeros(saves, N);           % Empty matrix for wave functions Psi(t, q)
116 PSI_save_Exp = zeros(saves, N*2-1);     % Empty matrix for wave functions Psi(t, qexp)
117
118 Vext = (0.5*m*omega_z^2*(x + shift_Vext).^2)';  % Potential energy per well
119 MaxExpqr = hbar*kr/m*ExpansionTime;             % Expansion factor
120
121 % psi_x = exp(-(x.^2)/2/(l_z*3)^2);                                    % Psi_x Gauss function
122 psi_x = psi_x/sqrt(sum(abs(psi_x).^2));                               % Normalize it
123 PSI_Exp_Start = exp(-(q.^2)/2/(l_z/MaxExpqr)^2);                      % Psi_exp Gauss function
124 PSI_Exp_Start = abs(PSI_Exp_Start/sqrt(sum(abs(PSI_Exp_Start).^2))).^2; % Normalize
125
```

```
126 plot_potentials(psi_x);
127
128 % disp(strcat("U_c_DNLS: ", num2str(U_c_DNLS)));
129 % disp(strcat("U_dd_onsite: ", num2str(DD_onsite)));
130 % disp(strcat("U_dd_offsite: ", num2str(sum(DD_offsite))));
131 % disp(strcat("QF_factor: ", num2str(QF_factor)));
132 % disp(strcat("l: ", num2str(l)));
133 % disp(strcat("eta: ", num2str(eta)));
134
135 %% --------- Calculate Tunnel matrix element ------------------------------
136
137 nCoeff   = 40;                      % Number of coeffs >0
138 mCoeff   = -nCoeff:1:nCoeff;        % List of coeffs
139 E0       = zeros(1,N);              % First bloch band energies
140
141 for index_q = 1:N
142     H = make_HMatrix(q(index_q));
143     [cn, En] = eig(H);
144     E0(index_q) = En(1);
145 end
146 figure(3)
147 plot(E0)
148 K = abs(E0(1) - E0((N-1)/2 + 1))/4*Er;      % Tunneling element
149 K2 = 4/sqrt(pi)*s^(3/4)*exp(-2*sqrt(s))*Er; % Tunneling element from paper
150 disp(K/h); disp(K2/h);
151
152 %% ----- options and parameter values for ode45 solver and minimizer ------
153
154 options_integration = odeset('RelTol', 3e-8, 'AbsTol', 1e-8, 'Stats', 'off', 'MaxStep', 1e-6);
155 options_minimization = optimoptions(@fmincon, 'Algorithm', 'active-set', 'MaxFunctionEvaluations',
      1000, 'MaxIterations', 1000, 'OptimalityTolerance', 1e-30, 'ConstraintTolerance', 1e-10, '
      StepTolerance', 1e-30, 'Display', 'off');
156
157 A = [];             % nonlinear constraint
158 b = [];             % nonlinear constraint
159 Aeq = [];           % nonlinear constraint
160 beq = [];           % nonlinear constraint
161 lb = [1.5e-6, 0.1]; % lower bound
162 ub = [5e-6, 20];    % upper bound
163 nonlcon = [];       % nonlinear constraint
164
165 %% --------- Propagate imaginary in time for the ground state -------------
166
167 psi_x_2 = abs(psi_x).^2;    % Density psi_x
168 delta = 1;                  % Difference between wave functions of steps
169 counter = 0;                % Counter
170 dtgs = 1e-6;                % dt for finding ground state
171
172 while (delta > 1e-7)
173     n = Natoms*psi_x_2;
174     if mod(counter, Plot_energy.mod) == 0 && Plot_energy.bool
175         l_lin = logspace(log10(8e-7), log10(5e-6), 50);
```

```
176         eta_lin = logspace(log10(0.1), log10(22), 50);
177         % l_lin = logspace(log10(1.3e-6), log10(2.3e-6), 100);
178         % eta_lin = logspace(log10(5), log10(22), 100);
179         Energy_plot = Energy_func(l_lin, eta_lin);
180 
181         % contour plot of energy
182         % figure(4)
183         % contour(log10(eta_lin), log10(l_lin), log10(Energy_plot), 300)
184         % colorbar
185         % drawnow
186 
187         % surface plot of energy surface
188         figure(21)
189         surf(eta_lin, l_lin, Energy_plot, 'EdgeColor', 'flat')
190         set(gca, 'xscale', 'log')
191         set(gca, 'yscale', 'log')
192         % set(h, 'zscale', 'log')
193         minimum = min(Energy_plot, [], "all");
194         maximum = max(Energy_plot, [], "all");
195         lims = [minimum minimum + 1000];
196         zlim(lims)
197         caxis(lims)
198         % set(gca, 'ColorScale', 'log')
199         xlabel("\eta")
200         ylabel("l")
201         zlabel("energy")
202         colorbar
203         drawnow
204     end
205 
206     x0 = [l, eta]; % starting value for minimization
207 
208     if Print_energy_vals.bool && mod(counter, Print_energy_vals.mod) == 0
209         [E1, E2, E3, E4, E5, E6, E7, E8, E9] = Energy2(x0);
210         disp(strcat(num2str(E1), "   ", num2str(E2), "   ", num2str(E3), "   ", num2str(E4), "   ",
      num2str(E5), "   ", num2str(E6), "   ", num2str(E7), "   ", num2str(E8), "   ", num2str(E9)))
211     end
212 
213     if delta > 5e-4
214         [x1, fval] = fmincon(@Energy, x0, A, b, Aeq, beq, lb, ub, nonlcon, options_minimization); %
       minimize func
215         l = x1(1);
216         eta = x1(2);
217         omega = hbar/(m*l^2);
218     else
219         if mod(counter, 50) == 0
220             [x1, fval] = fmincon(@Energy, x0, A, b, Aeq, beq, lb, ub, nonlcon, options_minimization
      ); % minimize func
221             l = x1(1);
222             eta = x1(2);
223             omega = hbar/(m*l^2);
224         end
```

```
225     end
226
227     % while abs(l - lb(1)) < 1e-7
228         % l = 2*l;
229         % [x1, fval] = fmincon(@Energy, [l, eta], A, b, Aeq, beq, lb, ub, nonlcon,
        options_minimization); % minimize func
230         % l = x1(1);
231         % eta = x1(2);
232         % omega = hbar/(m*l^2);
233         % disp("loop")
234     % end
235
236     % l_x = l/sqrt(eta);
237     % l_y = l*sqrt(eta);
238     % omega_x = hbar/(m*l_x^2);
239     % omega_y = hbar/(m*l_y^2);
240     % disp(strcat("l_x: ", num2str(l/sqrt(eta))))
241     % disp(strcat("l_y: ", num2str(l*sqrt(eta))))
242     % disp(strcat("omega_x: ", num2str(hbar/(m*(l/sqrt(eta))^2))))
243     % disp(strcat("omega_y: ", num2str(hbar/(m*(l*sqrt(eta))^2))))
244
245     QF_factor = (2/(5*pi^(3/2)*l^2*l_latt))^(3/2)*gamma_QF;     % Quantum fluctuation quasi 1D
246     U_c_DNLS = g/((2*pi)^(3/2)*l^2*l_latt);                     % DNLS contact term
247     if DDI == 0
248         DD_onsite = interpn(L, Eta, UDDI, l, eta, 'spline')*h;
249         inter_DDINNI1 = interpn(L, Eta, DDINNI, l, eta, 'spline')*h;
250         inter_DDINNI2 = interpn(L, Eta, DDINNI2, l, eta, 'spline')*h;
251         inter_DDINNI3 = interpn(L, Eta, DDINNI3, l, eta, 'spline')*h;
252         inter_DDINNI4 = interpn(L, Eta, DDINNI4, l, eta, 'spline')*h;
253     elseif DDI == 1
254         DD_onsite = interpn(etaV, lsV, Esave(:, :, 1, 2), eta, l*1e6, 'spline');
255         inter_DDINNI1 = interpn(etaV, lsV, Esave(:, :, 2, 2), eta, l*1e6, 'spline');
256         inter_DDINNI2 = interpn(etaV, lsV, Esave(:, :, 3, 2), eta, l*1e6, 'spline');
257         inter_DDINNI3 = interpn(etaV, lsV, Esave(:, :, 4, 2), eta, l*1e6, 'spline');
258         inter_DDINNI4 = interpn(etaV, lsV, Esave(:, :, 5, 2), eta, l*1e6, 'spline');
259     end
260     DD_offsite = [inter_DDINNI4, inter_DDINNI3, inter_DDINNI2, inter_DDINNI1, 0, inter_DDINNI1,
        inter_DDINNI2, inter_DDINNI3, inter_DDINNI4];
261
262     DD_off = 0;
263     for i = 1:2*cut+1
264         j = i - (cut + 1);
265         if j == 0
266             continue
267         end
268         DD_off = DD_off + Natoms*abs(circshift(psi_x, j)).^2*DD_offsite(i);
269     end
270
271     % disp(strcat("new l: ", num2str(l))); disp(strcat("new eta: ", num2str(eta)));
272     % disp(strcat("function at new x0: ", num2str(Energy([l, eta]))));
273
```

```
274     DD_off = DD_off.'; % change DD_off to column vector for consistency in ode45 and to avoid
        calculating it two times per step
275
276     [TT,PSI_out] = ode45(@DGLFUNCGS, [0 dtgs/2 dtgs], psi_x, options_integration);
277     psi_x = PSI_out(3,:);
278     psi_x = psi_x/sqrt(sum(abs(psi_x).^2));
279     psi_x_3 = abs(psi_x).^2;
280     if (mod(counter, 25) == 0)
281         figure(1)
282         subplot(3, 2, 2)
283         plot(x/d,psi_x_3);
284         axis([-10 10 0 inf]);
285         title(['Run: \theta = ' num2str(theta) ', \phi = ' num2str(phi) ', a_s = ' num2str(a/a0) '
        a0']);
286         drawnow;
287         plot_potentials(psi_x);
288
289         % x_lin = linspace(-2*max([1/sqrt(eta), 1*sqrt(eta)]), 2*max([1/sqrt(eta), 1*sqrt(eta)]),
        1000);
290         % subplot(3, 2, 5)
291         % hold on
292         % plot(x_lin, 1/(sqrt(pi)*1/sqrt(eta))*exp(-x_lin.^2/((1/sqrt(eta))^2)))
293         % plot(x_lin, 1/(sqrt(pi)*1*sqrt(eta))*exp(-x_lin.^2/((1*sqrt(eta))^2)))
294         % hold off
295         % drawnow;
296
297         % disp(strcat("Delta: ", num2str(delta)));
298         % disp(strcat("new 1: ", num2str(1))); disp(strcat("new eta: ", num2str(eta)));
299         % x1 = [1, eta];
300         % disp(strcat("energy at (1,eta): ", num2str(fval)));
301
302     end
303     counter = counter + 1;
304     delta = sum(abs(psi_x_3 - psi_x_2));
305     psi_x_2 = psi_x_3;
306 end
307
308 %% -------------- Run for different Scattering lengths --------------------
309
310 mean_q = zeros(1, saves);      % Empty matrix for mean momentum of Psi(t,qexp)
311 width_q = zeros(1, saves);     % Empty matrix for momentum width of Psi(t, qexp)
312 Psi_save_BO = zeros(saves, N);
313 Psi_save_q_BO = zeros(saves, N);
314 Psi_save_Exp_BO = zeros(saves, 2*N-1);
315
316 psi_x = sqrt(psi_x_3);
317 psi_x_2 = psi_x_3;
318
319 psi_q = fftshift(fft(psi_x));
320 psi_q = psi_q/sqrt(sum(abs(psi_q).^2));
321 psi_q_2 = abs(psi_q).^2;
322
```

```
psi_exp_2 = conv(PSI_Exp_Start,psi_q_2);
psi_exp_2 = psi_exp_2/sum(psi_exp_2);

%% -------------- Save the simulation start -------------------------------

PSI_save(1,:) = psi_x_2;
PSI_save_q(1,:) = psi_q_2;
PSI_save_Exp(1,:) = psi_exp_2;

Ewx = sum(psi_exp_2.*qexp);
Erw2x = sum(psi_exp_2.*((qexp-Ewx).^2));
mean_q(1) = Ewx;
width_q(1) = 2*sqrt(Erw2x);

test = sort(psi_x_2,'descend');
latticesites = 1;
while (sum(test(1:latticesites)) < 0.999)
    latticesites = latticesites + 1;
end

%% -------------- Plot the simulation start -------------------------------

figure(1)
subplot(3,2,2);
plot(x/d,psi_x_2,x/d,PSI_save(1,:),'r');
title(['Prop. time = ' num2str(0,4) ' ms / ' ...
num2str(0,3) ' %']);
xlabel('lattice site n');
axis([-20 20 0 inf]);

subplot(3,2,4);
plot(q,psi_q_2);
title('momentum in q');
xlabel('q/kr');

subplot(3,2,1);
plot(0,width_q(1),'o');
xlabel('Propagation time [ms]'); ylabel('moment2_k');
drawnow;

%% --------- Change physical parameters for bloch oscillations ------------

load(['EnergyOnOffsite4_Vz', int2str(s), '_Theta', int2str(theta), '_Phi', int2str(phi)], 'L', 'Eta
     ', 'UDDI', 'DDINNI', 'DDINNI2', 'DDINNI3', 'DDINNI4');
load('DDI.mat', 'lsV', 'etaV', 'Esave');
theta = theta/180*pi;
phi = phi/180*pi;

% omega_x_BO = 4*2*pi;
% omega_y_BO = 4*2*pi;
% omega_z_BO = 0.5*2*pi;
l_x_BO = sqrt(hbar/(m*omega_x_BO));
```

```
l_y_BO = sqrt(hbar/(m*omega_y_BO));
l_z_BO = sqrt(hbar/(m*omega_z_BO));
l_BO = sqrt(l_x_BO*l_y_BO);
eta_BO = sqrt(omega_x_BO/omega_y_BO);
if evolution_params == 0
    l_BO = l;
    eta_BO = eta;
end
omega_BO = hbar/(m*l_BO^2);

a_BO = a_copy*a0;                           % scattering length
g_BO = 4*pi*hbar^2*a_BO/m;                  % Nonlinear interaction term

if DDI == 0
    DD_onsite = interpn(L, Eta, UDDI, l_BO, eta_BO, 'spline')*h;
    inter_DDINNI1 = interpn(L, Eta, DDINNI, l_BO, eta_BO, 'spline')*h;
    inter_DDINNI2 = interpn(L, Eta, DDINNI2, l_BO, eta_BO, 'spline')*h;
    inter_DDINNI3 = interpn(L, Eta, DDINNI3, l_BO, eta_BO, 'spline')*h;
    inter_DDINNI4 = interpn(L, Eta, DDINNI4, l_BO, eta_BO, 'spline')*h;
elseif DDI == 1
    DD_onsite = interpn(etaV, lsV, Esave(:, :, 1, 2), eta_BO, l_BO*1e6, 'spline');
    inter_DDINNI1 = interpn(etaV, lsV, Esave(:, :, 2, 2), eta_BO, l_BO*1e6, 'spline');
    inter_DDINNI2 = interpn(etaV, lsV, Esave(:, :, 3, 2), eta_BO, l_BO*1e6, 'spline');
    inter_DDINNI3 = interpn(etaV, lsV, Esave(:, :, 4, 2), eta_BO, l_BO*1e6, 'spline');
    inter_DDINNI4 = interpn(etaV, lsV, Esave(:, :, 5, 2), eta_BO, l_BO*1e6, 'spline');
end
DD_offsite = [inter_DDINNI4, inter_DDINNI3, inter_DDINNI2, inter_DDINNI1, 0, inter_DDINNI1,
     inter_DDINNI2, inter_DDINNI3, inter_DDINNI4];
U_c_DNLS = g_BO/((2*pi)^(3/2))/l_BO^2/l_latt;
eps_dd = C_dd/(3*g_BO);
gamma_QF = LHY*abs(32/3*g_BO*sqrt(a_BO^3/pi)*(1 + 3/2*eps_dd^2));
QF_factor = (2/(5*pi^(3/2)*l_BO^2*l_latt))^(3/2)*gamma_QF;

Vext = (x*Fext + 0.5*m*omega_z_BO^2*(x + shift_Vext).^2)';   % Potential due to Gravity and
     harmonic trap

%% ------ Propagation ----------------------------------------------------

for counter = 2:saves

    DD_off = 0;
    for i = 1:2*cut+1
        j = i - (cut + 1);
        if j == 0
            continue
        end
        DD_off = DD_off + Natoms*abs(circshift(psi_x, j)).^2*DD_offsite(i);
    end

    DD_off = DD_off.';

    [TT,PSI_out] = ode45(@DGLFUNCBO,[0 dt/2 dt],psi_x,options_integration);
```

```
424     psi_x = PSI_out(3,:);
425     psi_x = psi_x/sqrt(sum(abs(psi_x).^2));
426     psi_x_2 = abs(psi_x).^2;    % Density psi_x
427
428     psi_q = fftshift(fft(psi_x));
429     psi_q = psi_q/sqrt(sum(abs(psi_q).^2));
430     psi_q_2 = abs(psi_q).^2;
431
432     psi_exp_2 = conv(PSI_Exp_Start,psi_q_2);
433     psi_exp_2 = psi_exp_2/sum(psi_exp_2);
434
435
436     % ---------- save step ---------
437
438     PSI_save(counter,:) = psi_x_2;
439     PSI_save_q(counter,:) = psi_q_2;
440     PSI_save_Exp(counter,:) = psi_exp_2;
441
442     Ewx = sum(psi_exp_2.*qexp);
443     Erw2x = sum(psi_exp_2.*((qexp-Ewx).^2));
444     mean_q(counter) = Ewx;
445     width_q(counter) = 2*sqrt(Erw2x);
446
447     % ---------- plot step ---------
448
449     subplot(3,2,2);
450     plot(x/d, psi_x_2, x/d, PSI_save(1,:), 'r');
451     axis([-10 10 0 inf]);
452     title(['Prop. time = ' num2str((counter - 1)*dt*1e3, 4) ' ms / ' num2str(counter/saves*100, 3)
        ' %']);
453     xlabel('lattice site n');
454
455     subplot(3,2,4);
456     plot(q, psi_q_2);
457     title('momentum (q)');
458     xlabel('q/kr');
459
460     subplot(3,2,1); plot((0:dt:(counter-1)*dt)*1e3,width_q(1:counter),'o');
461     title(['Run: \theta = ' num2str(theta*180/pi) ', \phi = ' num2str(phi*180/pi) ', a_s = '
        num2str(a_copy) ' a0, N = ' num2str(Natoms)]);
462     xlabel('Propagation time [ms]'); ylabel('Momentum width');
463
464     subplot(3,2,3);
465     qdensity_image = 8e3*PSI_save_Exp(1:counter,:)';
466     qdensity_image(qdensity_image>64) = 64;
467     image((0:dt:(counter-1)*dt)*1e3,qexp,qdensity_image);
468     xlabel('Propagation time [ms]');
469
470     subplot(3,2,5);
471     plot((0:dt:(counter-1)*dt)*1e3, -1*squeeze(mean_q(1:counter)));
472     xlabel('Propagation time [ms]');
473     ylabel('Mean momentum (q)');
```

```
474
475     drawnow;
476 end
477
478 Psi_save_BO(:, :) = PSI_save;
479 Psi_save_q_BO(:, :) = PSI_save_q;
480 Psi_save_Exp_BO(:, :) = PSI_save_Exp;
481
482 %% ------------------------ Plots at the end -----------------------------
483
484 %% ---------------------- Additional functions --------------------------
485
486 %% Differential equation for BO evolution of groundstate
487
488 function DPSIBO = DGLFUNCBO(t,PSI)
489 psi_j = PSI;
490
491 n = Natoms*abs(psi_j).^2;
492 psi_jm1 = [0; PSI(1:N-1); ];
493 psi_jp1 = [PSI(2:N); 0;];
494
495 DNLS = n*U_c_DNLS;
496 DD_on = n*DD_onsite;
497 QF = QF_factor.*n.^(3/2);
498 % QF = 0;
499 % DD_on = 0;
500 % DD_off = 0;
501
502 DPSIBO = -1i/hbar*(Vext + DNLS + DD_on + DD_off + QF).*psi_j + 1i/hbar*K*(psi_jm1 + psi_jp1);
503
504 end
505
506 %% Differential equation for calculation of groundstate
507
508 function DPSIGS = DGLFUNCGS(t,PSI)
509 psi_j = PSI;
510
511 n = Natoms*abs(psi_j).^2;
512 psi_jm1 = [0; PSI(1:N-1); ];
513 psi_jp1 = [PSI(2:N); 0;];
514
515 DNLS = n*U_c_DNLS;
516 DD_on = n*DD_onsite;
517 QF = QF_factor.*n.^(3/2);
518 % QF = 0;
519 % DD_on = 0;
520 % DD_off = 0;
521
522 DPSIGS = - 1/hbar*(Vext + DNLS + DD_on + DD_off + QF).*psi_j + K/hbar*(psi_jm1 + psi_jp1);
523
524 end
525
```

```
%% Function to create Hamiltonian matrix

function H = make_HMatrix(q) % Make Hamiltonian matrix for tunneling coefficient calculation
    h1    = (2*mCoeff+q).^2+ s/2;
    hDiag = diag(h1,0);
    h2    = ones(2*nCoeff,1)*(+s)/4;
    hOffs = diag(h2,1)+diag(h2,-1);
    H = hDiag + hOffs;
end



%% Function to plot the potentials with a given density

function plot_potentials(psi) % Plot all the potential constants in the beginning

    start = fix(length(psi)/2) - 14;
    ende = fix(length(psi)/2) + 16;
    x_lin = -15:1:15;
    n_lin = Natoms*abs(psi).^2;

    DD_off = 0;
    for i = 1:2*cut+1
        j = i - (cut + 1);
        if j == 0
            continue
        end
        DD_off = DD_off + Natoms*abs(circshift(psi, j)).^2*DD_offsite(i);
    end

    figure(1)
    subplot(3, 2, 6)
    plot(x_lin, U_c_DNLS*n_lin(start:1:ende)/h, x_lin, DD_onsite*n_lin(start:1:ende)/h, x_lin,
     DD_off(start:1:ende)/h, x_lin, QF_factor*n_lin(start:1:ende).^(3/2)/h)
    legend({"DNLS", "DD onsite", "DD offsite", "QF"}, "Location", "northeast")
    xlabel("Lattice site j")
    ylabel("Energy (Hz)")
    axis([-10 10 -inf inf])
    drawnow;
end

%% Energy function to create minimization function

function En = Energy(y)
    if DDI == 0
        DD_onsite = interpn(L, Eta, UDDI, y(1), y(2), 'spline')*h;
        inter_DDINNI1 = interpn(L, Eta, DDINNI, y(1), y(2), 'spline')*h;
        inter_DDINNI2 = interpn(L, Eta, DDINNI2, y(1), y(2), 'spline')*h;
        inter_DDINNI3 = interpn(L, Eta, DDINNI3, y(1), y(2), 'spline')*h;
        inter_DDINNI4 = interpn(L, Eta, DDINNI4, y(1), y(2), 'spline')*h;
    elseif DDI == 1
```

```
        DD_onsite = interpn(etaV, lsV, Esave(:, :, 1, 2), y(2), y(1)*1e6, 'spline');
        inter_DDINNI1 = interpn(etaV, lsV, Esave(:, :, 2, 2), y(2), y(1)*1e6, 'spline');
        inter_DDINNI2 = interpn(etaV, lsV, Esave(:, :, 3, 2), y(2), y(1)*1e6, 'spline');
        inter_DDINNI3 = interpn(etaV, lsV, Esave(:, :, 4, 2), y(2), y(1)*1e6, 'spline');
        inter_DDINNI4 = interpn(etaV, lsV, Esave(:, :, 5, 2), y(2), y(1)*1e6, 'spline');
    end
    DD_offsite = [inter_DDINNI4, inter_DDINNI3, inter_DDINNI2, inter_DDINNI1, 0, inter_DDINNI1,
     inter_DDINNI2, inter_DDINNI3, inter_DDINNI4];

    DD_off = 0;
    for i = 1:2*cut+1
        j = i - (cut + 1);
        if j == 0
            continue
        end
        DD_off = DD_off + Natoms*abs(circshift(psi_x, j)).^2*DD_offsite(i);
    end

    % DD_onsite = 0;
    % DD_off = 0*DD_off;
    % gamma_QF = 0;

    En = (hbar^2./(4*m*y(1).^2)*(y(2) + 1./y(2)) + ...
    m*y(1).^2/4.*(omega_x^2./y(2) + y(2).*omega_y^2) + ...
    1/2*m*omega_z^2*l_latt^2 + ...
    hbar^2/(4*m*l_latt^2) + ...
    K*sum((circshift(psi_x, 1) + circshift(psi_x, -1)).*psi_x) + ...
    1/2*g./((2*pi)^(3/2)*y(1).^2*l_latt)*sum(n.*psi_x_2) + ...
    1/2*DD_onsite*sum(n.*psi_x_2) + ...
    1/2*sum(DD_off.*psi_x_2) + ...
    2/5*(2/(5*pi^(3/2)*y(1)^2*l_latt))^(3/2)*gamma_QF*sum(n.^(3/2).*psi_x_2))/h;
end

%% Energy function to create a surface plot

function en = Energy_func(l, eta)
    en = zeros(length(l), length(eta));

    for p = 1:length(l)

        for w = 1:length(eta)
            if DDI == 0
                DD_onsite2 = interpn(L, Eta, UDDI, l(p), eta(w), 'spline')*h;
                inter_DDINNI1 = interpn(L, Eta, DDINNI, l(p), eta(w), 'spline')*h;
                inter_DDINNI2 = interpn(L, Eta, DDINNI2, l(p), eta(w), 'spline')*h;
                inter_DDINNI3 = interpn(L, Eta, DDINNI3, l(p), eta(w), 'spline')*h;
                inter_DDINNI4 = interpn(L, Eta, DDINNI4, l(p), eta(w), 'spline')*h;
            elseif DDI == 1
                DD_onsite2 = interpn(etaV, lsV, Esave(:, :, 1, 2), eta(w), l(p)*1e6, 'spline');
                inter_DDINNI1 = interpn(etaV, lsV, Esave(:, :, 2, 2), eta(w), l(p)*1e6, 'spline');
                inter_DDINNI2 = interpn(etaV, lsV, Esave(:, :, 3, 2), eta(w), l(p)*1e6, 'spline');
                inter_DDINNI3 = interpn(etaV, lsV, Esave(:, :, 4, 2), eta(w), l(p)*1e6, 'spline');
```

```
628                 inter_DDINNI4 = interpn(etaV, lsV, Esave(:, :, 5, 2), eta(w), l(p)*1e6, 'spline');
629             end
630             DD_offsite2 = [inter_DDINNI4, inter_DDINNI3, inter_DDINNI2, inter_DDINNI1, 0,
      inter_DDINNI1, inter_DDINNI2, inter_DDINNI3, inter_DDINNI4];
631
632             % DD_onsite2 = 0;
633             % DD_offsite2 = 0*DD_offsite2;
634             % gamma_QF = 0;
635
636             DD_off2 = 0;
637             for i = 1:2*cut+1
638                 j = i - (cut + 1);
639                 if j == 0
640                     continue
641                 end
642                 DD_off2 = DD_off2 + Natoms*abs(circshift(psi_x, j)).^2*DD_offsite2(i);
643             end
644
645             en(p, w) = hbar^2./(4*m*l(p).^2).*(eta(w) + 1./eta(w)) + ...
646                  m*l(p).^2/4.*(omega_x^2./eta(w) + eta(w).*omega_y^2) + ...
647                  1/2*m*omega_z^2*l_latt^2 + ...
648                  hbar^2/(4*m*l_latt^2) + ...
649                  K*sum((circshift(psi_x, 1) + circshift(psi_x, -1)).*psi_x) + ...
650                  1/2*g./((2*pi)^(3/2)*x(1).^2*l_latt)*sum(n.*psi_x_2) + ...
651                  1/2*DD_onsite2*sum(n.*psi_x_2) + ...
652                  1/2*sum(DD_off2.*psi_x_2) + ...
653                  2/5.*(2./(5*pi^(3/2)*l(p).^2*l_latt)).^(3/2)*gamma_QF*sum(n.^(3/2).*psi_x_2);
654         end
655     end
656     en = en/h;
657 end
658
659 %% Print the energy contributions separately
660
661 function [E1, E2, E3, E4, E5, E6, E7, E8, E9] = Energy2(x)
662     if DDI == 0
663         DD_onsite = interpn(L, Eta, UDDI, x(1), x(2), 'spline')*h;
664         inter_DDINNI1 = interpn(L, Eta, DDINNI, x(1), x(2), 'spline')*h;
665         inter_DDINNI2 = interpn(L, Eta, DDINNI2, x(1), x(2), 'spline')*h;
666         inter_DDINNI3 = interpn(L, Eta, DDINNI3, x(1), x(2), 'spline')*h;
667         inter_DDINNI4 = interpn(L, Eta, DDINNI4, x(1), x(2), 'spline')*h;
668     elseif DDI == 1
669         DD_onsite = interpn(etaV, lsV, Esave(:, :, 1, 2), x(2), x(1)*1e6, 'spline');
670         inter_DDINNI1 = interpn(etaV, lsV, Esave(:, :, 2, 2), x(2), x(1)*1e6, 'spline');
671         inter_DDINNI2 = interpn(etaV, lsV, Esave(:, :, 3, 2), x(2), x(1)*1e6, 'spline');
672         inter_DDINNI3 = interpn(etaV, lsV, Esave(:, :, 4, 2), x(2), x(1)*1e6, 'spline');
673         inter_DDINNI4 = interpn(etaV, lsV, Esave(:, :, 5, 2), x(2), x(1)*1e6, 'spline');
674     end
675     DD_offsite = [inter_DDINNI4, inter_DDINNI3, inter_DDINNI2, inter_DDINNI1, 0, inter_DDINNI1,
      inter_DDINNI2, inter_DDINNI3, inter_DDINNI4];
676
677
```

```
678     DD_off = 0;
679     for i = 1:2*cut+1
680         j = i - (cut + 1);
681         if j == 0
682             continue
683         end
684         DD_off = DD_off + Natoms*abs(circshift(psi_x, j)).^2*DD_offsite(i);
685     end
686 
687     E1 = (hbar^2./(4*m*x(1).^2)*(x(2) + 1./x(2)))/h;                                % Radial
        kinetic energy/correction
688     E2 = (m*x(1).^2/4.*(omega_x^2./x(2) + x(2).*omega_y^2))/h;                      % Radial
        potential energy
689     E3 = (1/2*m*omega_z^2*l_latt^2)/h;                                              % Axial
        potential energy
690     E4 = hbar^2/(4*m*l_latt^2)/h;                                                   % Axial
        kinetic energy
691     E5 = (K*sum((circshift(psi_x, 1) + circshift(psi_x, -1)).*psi_x))/h;            % Tunneling
         energy
692     E6 = (1/2*g./((2*pi)^(3/2)*x(1).^2*l_latt)*sum(n.*psi_x_2))/h;                  % Contact
        interaction energy
693     E7 = (1/2*DD_onsite*sum(n.*psi_x_2))/h;                                         % Onsite
        dipole-dipole interaction energy
694     E8 = (1/2*sum(DD_off.*psi_x_2))/h;                                              % Offsite
        dipole-dipole interaction energy
695     E9 = (2/5*(2/(5*pi^(3/2)*x(1)^2*l_latt))^(3/2)*gamma_QF*sum(n.^(3/2).*psi_x_2))/h;  % Quantum
        fluctuations energy/Lee-Huang-Yang term
696 end
697 
698 %% Clear all figures
699 
700 function clfall
701 FigList = findall(groot, 'Type', 'figure');
702 for iFig = 1:numel(FigList)
703     try
704         clf(FigList(iFig));
705     catch
706         % Nothing to do
707     end
708 end
709 end
710 
711 end
```